Paul Frank

Thin film growth of rod-like and disc-shaped organic molecules on insulator and noble metal surfaces

PHD THESIS

For obtaining the academic degree

„Doktor der Technischen Wissenschaften“

Graz University of Technology

Supervisor:

Ao. Univ.-Prof. Dipl.-Ing. Dr. techn. Adolf Winkler

Institute of Solid State Physics

Graz, July 2009

EIDESSTATTLICHE ERKLÄRUNG

Ich erkläre an Eides statt, dass ich die vorliegende Arbeit selbständig verfasst, andere als die angegebenen Quellen/Hilfsmittel nicht benutzt, und die den benutzten Quellen wörtlich und inhaltlich entnommene Stellen als solche kenntlich gemacht habe.

Graz, am …… ……..
(Unterschrift)

Englische Fassung:

STATUTORY DECLARATION

I declare that I have authored this thesis independently, that I have not used other than the declared sources / resources, and that I have explicitly marked all material which has been quoted either literally or by content from the used sources.

…… ……..
date (signature)

Acknowledgement

First of all I would like to express my sincere gratitude to Prof. Dr. Adolf Winkler, who has been my supervisor since the beginning of my studies at the Institute of Solid State Physics. He provided me with many helpful suggestions, important advice and constant encouragement during the course of this work. Furthermore, from the Institute of Solid State Physics at the TU Graz I want to thank Franz Nussbacher and Robert Teubenbacher for their valuable contribution to my work. Additionally I acknowledge Martin Kornschober, who always solved my construction problems diligently and skillfully, and my lab mate Markus Kratzer, who helped me to solve numerous scientific and technical mysteries.

I owe special thanks to Gregor Hlawacek and Prof. Dr. Christian Teichert from the University of Leoben for taking intense academic interest in this thesis as well as for providing valuable suggestions that improved the quality of my studies.

Apart from the scientific part of my work, I would like to mention here that I enjoyed working is such an amicable atmosphere at this institute. In this context I would like to thank my lab mates Markus Kratzer, Johanna Stettner, Jörg Killmann and Erkan Demirci for many pleasant hours of working in a climate of friendship. The same applies to Prof. Dr. Robert Schennach, Eduard Gilli, Hans-Peter Koch, Anton Tamtögl and Axel Stupnik who were never averse to entering interesting conversations.

Last but not least I am deeply grateful to my family and to my girlfriend Lisa who helped me to concentrate on completing this thesis and supported me mentally during the course of my studies.

Abstract

Organic materials are considered as promising candidates for next generation electronics. In this context, a detailed understanding of the fundamental properties of thin organic films is desirable. For this purpose often model systems with well-defined substrates and pristine organic adsorbates are investigated. In many cases it turns out that the properties of the thin organic films depend on their structure and morphology, which in turn can often be tailored by altering the growth parameters.

In the present work the thin film growth (morphology, structure) and the adsorption / desorption kinetics of the rod-like molecule hexaphenyl (p6P) and of the disc-shaped molecule hexaaza-triphenylene-hexacarbonitrile (HATCN) were investigated on various substrates.

The thin films were prepared utilizing organic molecular beam epitaxy (OMBE) under well defined ultra-high vacuum (UHV) conditions. The substrate temperature could be varied from 100 K up to 1000 K.

The substrate surfaces were characterized by Auger electron spectroscopy (AES), X-ray photoelectron spectroscopy (XPS) and low energy electron diffraction (LEED). For the initial state of layer growth, thermal desorption spectroscopy (TDS) was used to search for a wetting layer and to reckon the kinetic parameters of desorption. In this work, the term wetting layer is used for a monomolecular continuous layer built up by molecules lying flat on the surface, which are particularly strongly bonded to the substrate. For thicker films, in-situ XPS in combination with TDS was applied to reveal the kinetics of the layer growth. The work function could be measured in-situ with a purchased Kelvin probe (KP). Ex-situ atomic force microscopy (AFM) conducted under ambient atmosphere conditions was used to analyze the film morphology.

The first part of this work (**chapter 5**) deals with the growth of hexaphenyl on clean and on modified mica surfaces. As it turned out, the formation of a wetting layer crucially influences the further film growth: On clean mica, a wetting layer exists which leads to the growth of elongated islands (so-called needles) consisting of molecules lying flat on the surface (long molecular axis parallel to the substrate surface). If the formation of the wetting layer is

prohibited by an artificial chemical or structural modification of the mica substrate, terraces develop which comprise molecules which are oriented with their long axis normal to the surface, i.e. standing molecules. Thus the wetting layer serves as a template for further film growth, as these rod-like molecules prefer π-stacking (parallel arrangement with respect to each other).

On KCl (**chapter 6**), no wetting layer forms, which brings about the growth of terraces (standing molecules) together with needles (lying molecules), which arrange with respect to the four fold symmetry of the substrate surface.

In contrast to the rod-like molecule p6P, the disc shaped HATCN molecules avoid π-stacking, which leads to a completely different film growth behavior (**chapter 6 & 7**). On Au (111), the first two layers are made up of molecules lying flat on the surface, on which then the bulk phase starts to grow. Interestingly, with increasing film thickness the flat lying molecules in the first layers become incorporated into the bulk structure as the temperature is raised above 350 K, which leads also to a change in film morphology from layer-by-layer growth to island growth. The islands formed upon this rearrangement feature the well-known bulk crystal structure of HATCN. The HATCN crystals are oriented with their (143) plane parallel to the Au (111) surface. On Ag (111), at the beginning a strongly bonded lying monolayer is formed which does not desorb upon heating. Interestingly, with increasing film thickness this monolayer transforms into a monolayer built up of standing molecules. On this monolayer metastable layers start growing which most probably consist of flat lying, but orderless molecules. Like on gold, the metastable flat lying layers get incorporated into the bulk phase as the film thickness is increased, thus forming crystalline islands, again with the well-known bulk crystal structure. Nevertheless, the thick film growth on silver is different from the one on gold, because the first monolayer on silver is a stable one, i.e. does not get integrated into the bulk phase. This leads to a significantly different film morphology. Additionally, the HATCN crystals on silver are orderless with respect to the surface. These findings were necessary to understand the work function change induced by HATCN adsorption on Au (111) and Ag (111).

Kurzfassung

Organische Materialien gelten als vielversprechende Kandidaten für neuartige elektronische Bauteile. In diesem Zusammenhang ist ein genaues Verständnis der grundlegenden Eigenschaften von dünnen organischen Schichten wünschenswert. Zu diesem Zweck werden oft Modellsysteme mit wohldefinierten Substraten und hochreinen organischen Adsorbaten untersucht. In vielen Fällen stellt es sich heraus, dass die Eigenschaften der dünnen organischen Filme von ihrer Struktur und Morphologie abhängen, welche wiederum oftmals durch Änderungen der Wachstumsparameter beeinflusst werden können.

In der vorliegenden Arbeit wurden das Wachstum von dünnen Schichten (Morphologie, Struktur) und die Adsorptions / Desorptionskinetik von dem stäbchenförmigen Molekül Hexaphenyl (p6P) und dem scheibchenförmigen Molekül Hexaaza-triphenylene-hexacarbonitril (HATCN) auf verschiedenen Substraten untersucht.

Die dünnen Schichten wurden unter Ultrahochvakuumbedingungen (UHV) mit Hilfe von Molekularstrahlepitaxie (OMBE) präpariert. Die Temperatur des Substrates konnte zwischen 100 K und 1000 K variiert werden.

Die Substratoberflächen wurden mittels Augerelektronenspektroskopie (AES), Röntgenphotoelektronenspektroskopie (XPS) und Beugung niederenergetischer Elektronen (LEED) untersucht. Um festzustellen, ob ein ‚Wettinglayer' (= benetzende erste Schicht) existiert und zur Bestimmung der kinetischen Parameter der Desorption wurde bei ultradünnen Schichten die thermische Desorptionsspektroskopie (TDS) verwendet. In dieser Arbeit wird der Begriff ‚Wettinglayer' für eine monomolekulare kontinuierliche Schicht verwendet, die aus Molekülen besteht, die flach auf der Oberfläche liegen und besonders stark an das Substrat gebunden sind. Für dickere Schichten wurde eine Kombination aus XPS und TDS Messungen angewendet, um die Kinetik des Schichtwachstums zu untersuchen. Die Austrittsarbeit konnte mit einer Kelvinsonde im UHV gemessen werden. Die Rasterkraftmikroskopmessungen (AFM) zur Analyse der Schichtmorphologie wurden unter Umgebungsluft durchgeführt.

Der erste Teil dieser Arbeit (**Kapitel 5**) befasst sich mit dem Wachstum von Hexaphenyl auf reinen und modifizierten Glimmeroberflächen. Es stellte sich heraus, dass die Ausbildung

eines Wettinglayers das weitere Schichtwachstum entscheidend beeinflusst: Auf reinem Glimmer existiert ein Wettinglayer, der zum Wachstum von länglichen Inseln (sogenannten Nadeln) führt. Diese Nadeln bestehen aus Molekülen, die flach auf der Oberfläche liegen (mit der langen Molekularachse parallel zur Substratoberfläche). Wenn die Ausbildung einer benetzenden Schicht durch künstliche chemische oder strukturelle Veränderungen des Glimmersubstrates verhindert wird, bilden sich terrassenförmige Strukturen aus. Diese Terrassen bestehen aus Molekülen, die mit ihrer langen Molekularachse normal auf die Oberfläche stehen, d.h. aus stehenden Molekülen. Also dient der Wettinglayer als Vorlage für das weitere Schichtwachstum, da die p6P Moleküle sogenanntes π-stacking bevorzugen (= parallele Anordnung zueinander).

Auf KCl (**Kapitel 6**) bildet sich keine benetzende Schicht, was zum Wachstum von Terrassen (stehende Moleküle) zusammen mit Nadeln (liegende Moleküle) führt, die sich bezüglich der vierfachen Symmetrie der Substratoberfläche ausrichten.

Im Gegensatz zum stäbchenförmigen Molekül p6P vermeiden die scheibchenförmigen HATCN Moleküle π-stacking, was zu einem völlig anderen Verhalten des Schichtwachstums führt (**Kapitel 6** & **7**). Die ersten beiden Lagen auf Au (111) bestehen aus Molekülen, die flach auf der Oberfläche liegen. Auf diesen beiden Lagen beginnt mit zunehmender Schichtdicke die Kristallphase zu wachsen. Bemerkenswerterweise werden die flach liegenden Moleküle der ersten beiden Lagen mit steigender Schichtdicke in die Kristallphase eingebaut, wenn die Temperatur über 350 K erhöht wird. Dies führt auch zu einer Änderung der Schichtmorphologie von Lagenwachstum zu Inselwachstum. Die Inseln, die bei dieser Umordnung gebildet werden, weisen die bekannte Kristallstruktur von HATCN auf. Die HATCN Kristallite sind mit ihrer (143) Ebene parallel zur Au (111) Oberfläche ausgerichtet. Auf Ag (111) bildet sich zu Beginn eine stark gebundene liegende Schicht, die während des Hochheizens nicht desorbiert. Interessanterweise wandelt sich diese Schicht mit steigender Schichtdicke in eine Schicht um, die aus stehenden Molekülen besteht. Auf dieser Schicht wiederum beginnt das Wachstum von metastabilen Schichten, die wahrscheinlich aus flach liegenden, aber ungeordneten Molekülen bestehen. Wie auf der Goldoberfläche werden auch hier die metastabilen Schichten aus flach liegenden Molekülen in die Kristallphase eingebaut wenn die Schichtdicke erhöht wird. Auf diese Weise werden kristalline Inseln gebildet, die wieder die bekannte Kristallstruktur aufweisen. Nichtsdestoweniger ist das Wachstum der dicken Schichten auf Silber anders als jenes auf Gold, da die erste Lage auf Silber stabil ist und nicht in die Kristallphase eingebaut wird. Ausserdem weisen die HATCN Kristalle auf

Silber keine bevorzugte Orientierung zur Oberfläche auf. Diese Erkenntnisse waren notwendig, um die durch HATCN verursachte Änderung der Austrittarbeit von Au (111) und Ag (111) zu verstehen.

Contents

List of Symbols and Abbreviations

p6P	para-hexaphenyl, sexiphenyl
α	multilayer desorption peak
AES	Auger electron spectroscopy
AFM	atomic force microscopy
amu	atomic mass unit
β	monolayer desorption peak
E_{des}	desorption energy
F4TCNQ	tetrafluoro-tetracyanoquinodimethane
HATCN	hexaaza-triphenylene-hexacarbonitrile
HIB	hole injection barrier
HWE	hot wall epitaxy
LEED	low energy electron diffraction
OMBE	organic molecular beam epitaxy
QMS	quadrupole mass spectrometer
RT	room temperature
SEM	scanning electron microscopy
STM	scanning tunneling microscopy
TCNE	tetracyanoethylene
TDS	thermal desorption spectroscopy
Θ	coverage
UHV	ultra-high vacuum
XPS	X-ray photoelectron spectroscopy
XRD	X-ray diffraction

1 Introduction

Novel organic materials are attractive candidates as active layer materials for organic electronic devices like thin film transistors, light emitting diodes or organic lasers. One of the frequently used materials is para-hexaphenyl (p6P), which is a very interesting model compound for studying the basic physical properties of conjugated organic semiconductors [1]. Devices using p6P such as organic light emitting diodes (OLED) [2–6], organic field effect transistors (OFET) and solar cells [7–11] have already been realized. In order to fabricate such devices, the growth parameters and stability properties of the organic films have to be well understood. Which growth mode is favored depends on the type of substrate, the substrate structure, the chemical composition of the substrate and the substrate temperature. Additionally, if a strongly bound first layer, a so-called wetting layer, exists, this layer will influence the further film growth. Several substrates have been used to study the thin film formation of hexaphenyl, for example Al [12–15], TiO_2 [15-17], CuO[18, 19] and Au [20–22]. Apart from these, a particular suitable substrate material is mica, because one can easily obtain well-defined single crystal surfaces by cleaving. Therefore the growth of p6P on mica has been the subject of many publications [15, 23-39]. It has been shown that p6P grows in a highly ordered fashion on the mica (001) surface, resulting in long (up to the  range) nano-fibres, which are oriented parallel to each other [24–26]. This type of nano-structures is important for nano-optics. Previous X-ray diffraction (XRD) studies revealed in this case a quasi-epitaxial relationship between the p6P crystallites and the mica substrate [27, 28]. On the other hand, in some cases the formation of ring-like structured islands has been observed [29]. Apparently, the substrate conditions have an important influence on the film growth. Another very frequently used substrate is potassium chloride (KCl). In this context, films prepared with physical vapor deposition (PVD) [40–46] and with hot-wall epitaxy (HWE) [47–49] have already been investigated. The initial growth stage exhibits crystalline needles which consist of molecules lying on the surface and form a rectangular network [49]. When a certain coverage is reached, terraces of standing molecules are formed. Using the right growth parameters and depending on the desired application, layers consisting of lying or standing molecules can be fashioned. For the electronic properties of devices apart from the molecular

arrangement of the active organic layer material also the metal/organic interface is of crucial importance. One of the most important properties that can be tailored by altering this interface intentionally is the charge injection. The charge injection can be enhanced by applying self assembled monolayers (SAMs) that carry an intrinsic dipole [50, 51] or by molecules that undergo a charge transfer type reaction with the electrode materials [52, 53, 54], or by applying thin layers of high work function metals [55]. In all cases a dipole at the interface is created that changes the electronic level alignment of subsequently deposited conjugated organic materials in such a way, that the hole injection barrier (HIB) can significantly be reduced. For example has it been shown that by the insertion of a thin layer of tetrafluoro-tetracyanoquinodimethane (F4-TCNQ) the HIB into p6P can be lowered by as much as 1.2 eV [56]. The major drawback of conventional cyano-based molecular acceptors like tetracyanoethylene (TCNE), tetracyanoquinodimethane (TCNQ) and F4-TCNQ is their rather low molecular weight, which implicates poor thermal stability of the grown structures. For F4-TCNQ this has already been shown to be a problem in devices [57]. Therefore molecular electron acceptors with higher thermal stability (which means to a first approximation a higher molecular weight) are desired. One of the novel cyano-based molecular acceptors with a significantly higher molecular weight and therefore with a higher thermal stability is hexaaza-triphenylene-hexacarbonitrile (HATCN). This discoid molecule features a very complex bulk structure with a unit cell consisting of 18 molecules [58, 59]. The thin film growth of HATCN was investigated in the course of this thesis in collaboration with other groups in detail.

The first part of the present work focuses on the influence of the intentional manipulation of the substrate and on the influence of the substrate temperature on the layer growth of the rod-like molecule p6P on mica (001) and KCl (001). In particular, the influence of the surface contamination by carbon and the structure modification by sputtering on the p6P layer growth was investigated.

The second part deals with the film growth of HATCN on Au (111) and Ag (111) and with the influence of the thin film structure on the work function of the surfaces. Important issues were the thermal stability and the desorption kinetics of the films and the correlation of the film growth to the HATCN-induced work function change of the substrate surfaces.

The presented results have been published in international scientific journals. The corresponding references are given in the reference list [60-68].

2 Basic concepts of epitaxial growth

In the following selected ideas established in inorganic film growth will be discussed which cannot always be transferred to organic film growth one to one, but nevertheless can often help to understand the fundamental mechanisms of organic layer or island formation.

Epitaxy is the commonly used denomination for the oriented growth of a crystalline material on a single crystal surface. The epitaxial orientation is determined by the condition for the minimum of the Gibbs free energy of the system, which is governed by the structure and the energy of the epitaxial interface. The key parameter which is used to describe the equilibrium between two phases is the chemical potential μ (eq. 2.1), which represents the derivatives of the Gibbs free energies with respect to the number of particles in the system at constant pressure P and temperature T.

$$\mu = \left(\frac{\partial G}{\partial n}\right)_{P,T} \tag{2.1}$$

In other words, the chemical potential μ is a measure of how much work has to be done to change the number of particles in a phase by one while keeping the temperature and the pressure constant.

The term ‘epitaxy’ is of course not limited to inorganic film growth. In the case of large organic molecules this term is also frequently used if the molecules form highly regular structures on single-crystalline substrates and a defined relationship between the regular structures of the adsorbate film and the substrate surface exists.

2.1 Thin film growth

Upon deposition of material the chemical potential of the surface will change due to adhesive and cohesive forces acting between the substrate and the adsorbate. Additionally, a lattice misfit of the two species will create misfit dislocations and strains whose energies also

influence the chemical potential. Therefore the chemical potential of the deposit will vary from monolayer to monolayer due to the interaction with the substrate, which leads to the appearance of the three well-known mechanisms of epitaxial growth [83, 84]:

- *Frank-van der Merwe* mechanism (layer-by-layer growth):

  if $\frac{d\mu}{dN} > 0$ for all layers N . The completion of the first layer $(N = 1)$ is more favorable than starting the second layer $(N = 2)$ → formation of 'wetting layers'

- *Stranski-Krastanov* mechanism (layer-by-layer followed by 3D island growth):

  If $\frac{d\mu}{dN} > 0$ for small N , but $\frac{d\mu}{dN} < 0$ for large N . After the formation of one or more wetting layers the adsorbate film will start to form 3D islands.

- *Volmer-Weber* mechanism (3D island growth):

  If $\frac{d\mu}{dN} < 0$ for all N . Island growth will occur immediately.

Generally, island growth is favored when the interfacial bonding is weaker than the bonding in the deposit itself. Additionally, high substrate temperatures and a large lattice misfit will both promote the cluster formation.

These general statements can be extended and specified for organic thin film growth in particular: The possible forces acting between the substrate and the adsorbate are defined by charge transfer, covalent chemical bonding, electrostatic multi-pole interactions and van der Waals interactions (physisorption) [71]. In many cases these interactions influence only the molecules within the first organic monolayer, whereas the second and subsequent layers are unaffected. Additionally, in the case of molecular crystals intermolecular interactions of van

der Waals type and/or electrostatic multi-pole type will be present throughout the organic bulk material. As a consequence, the relative strength of the involved interactions determines the molecular packing and the structure of the first adsorbed monolayer [94], which in turn often influences the structure of the subsequent layers. Therefore the question as to the existence of a continuous first monolayer, which is often denoted as 'wetting layer', is a key to understanding the thin film growth of organic systems. In some cases the wetting layer even acts as a template for further film growth, which is demonstrated for instance in **chapter 5**, which deals with the growth of p6P on differently treated mica (001) surfaces. There it is demonstrated that if a wetting layer comprising lying molecules is formed, the subsequent layers also comprise lying molecules. However, in some rare cases the structure of the subsequent layers influences the structure of the wetting layer: In **chapter 7** the very unusual layer growth behavior of HATCN on Au (111) is investigated and it turns out that the first two monolayers are both incorporated into the bulk structure after a critical layer thickness has been reached.

2.2 Nucleation

In the classical thermodynamic approach, the formation of a new phase B requires as a necessary prerequisite the appearance of small clusters of building units (atoms or molecules) in the volume of the supersaturated phase A (vapors, melt or in solution). These clusters or nuclei are small complexes of atoms or molecules which have the same properties as the corresponding bulk phases, but are much smaller [83]. In a homogeneous system near the phase equilibrium between the two phases, always small density fluctuations will be present. These fluctuations can lead to the formation of an aggregate of phase B in phase A and if the initial phase A is instable ($\mu_A > \mu_B$) the tendency to grow prevails after exceeding a certain critical radius r^*. This critical radius is defined by the interplay between the energy gain from creating the 3D droplet and the energy loss from creating new interfaces between the two phases. The critical size of the nuclei is also influenced by so-called surfactants because the process of nucleation is stimulated by the presence of impurities, ions or defects in the substrate.

In organic thin film growth, the concept of heterogeneous nucleation could be an approach to describe the formation of a phase B out of phase A of material 1 (adsorbate) in the presence of

material 2 (substrate). However, it turned out that the critical nucleus size in organic thin film growth is so small that it is impossible to designate such a nucleus as solid or liquid as no long range order can be observed. Therefore an atomistic view of nucleation is necessary in order to understand the processes involved.

2.3 Nucleation on islands: Step-edge barriers

Michely et al. [86-88] present an atomistic nucleation theory which describes the nucleation on islands in the presence of a step-edge barrier. Such a step-edge barrier for diffusing adatoms has been described for the first time by Ehrlich et al. [89] and Schwöbel et al. [90] and is therefore often referred to as Ehrlich-Schwöbel-Barrier. As a consequence, an adatom needs to surmount an activation barrier when crossing a step edge, which leads to the growth of pyramidal multilayer mounds (see **Fig. 2.1**, sometimes denoted as 'wedding cakes' [91, 92]). These mounds are formed by repeated two-dimensional nucleation on the subjacent island, respectively and their shape depends on the height of the step-edge barrier.

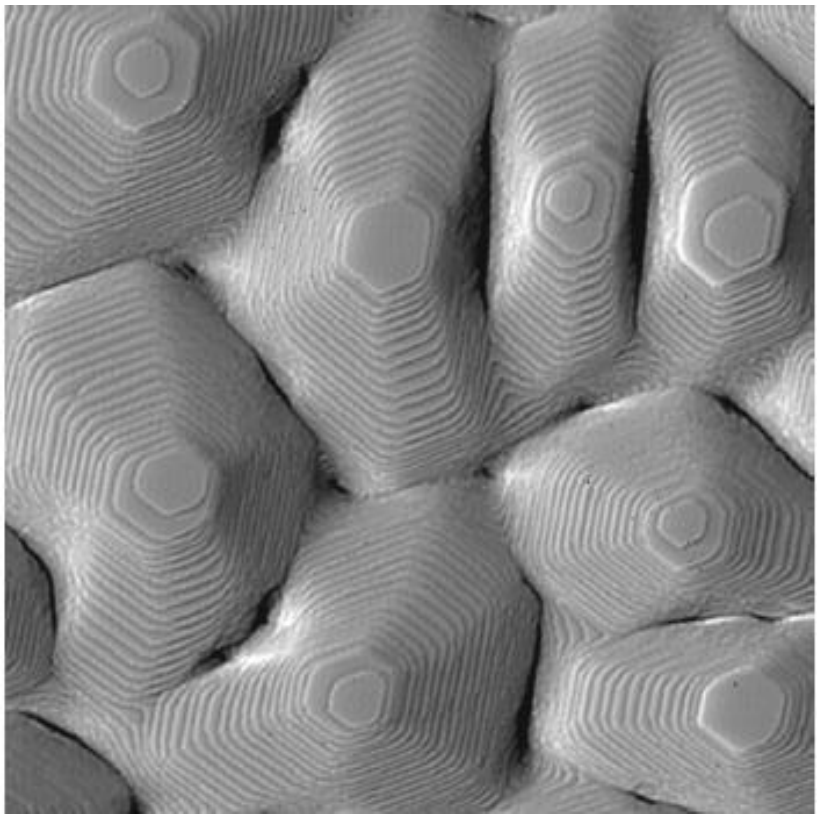

Fig. 2.1: STM image of pyramidal multilayer mounds which are formed due to the presence of a step-edge barrier upon Pt deposition on Pt (111) in a partial CO pressure. From [86].

In the case of an infinitely high step-edge barrier preventing any interlayer mass transport, the surface fractions in the individual layers follow a Poisson distribution [93]. By proper analysis of the shapes of the mounds it is possible to determine the height of the step-edge barrier (E_{SEB}) [65]: For this purpose, the previously mentioned theoretical model of Michely et al. is consulted: The height of the step-edge barrier together with the on-terrace jump rate ν governs the rate ν' at which molecules diffuse downwards across a terrace edge (= interlayer jump rate):

$$\nu' = \nu \cdot e^{-\frac{E_{SEB}}{k_B T}} \tag{2.2}$$

with $\nu \propto e^{-\frac{E_D}{k_B T}}$, E_D being the energy barrier for on-terrace diffusion, which is much smaller than E_{SEB}. The interlayer jump rate ν' can be estimated from the top terrace diameter l (gained from STM or AFM analysis) and the experimentally used deposition flux F :

$$l \propto \left(\frac{\nu'}{F}\right)^{\frac{1}{5}} \tag{2.3}$$

The on-terrace jump rate ν can be evaluated using kinetic nucleation theory [85]: If the step-edge barrier is large enough to effectively suppress interlayer mass transport, the on-terrace jump rate is in general related to the nucleation density N, which can be connected to the mound separation λ :

$$\frac{1}{\lambda^2} \propto N \propto \left(\frac{F}{\nu}\right)^{\frac{i^*}{D(i^*+2)}} \tag{2.4}$$

which can again be gained from STM or AFM image analysis. D is the dimension of the diffusion process (here $D = 2$) and i^* is the critical island size of the largest unstable cluster. For systems with strong barriers the choice $i^* = 1$ turned out to be reasonable [86], which

means that dimers are already stable and immobile. As soon as two adatoms are present on the island, nucleation will occur after a certain time provided that a large residence time of all atoms on the island is given (which is the case for systems with large step-edge barriers). In section **5.6.1 Step-edge barrier in organic film growth** it is shown that this well-known model for inorganic film growth can also be used for organic systems to verify the existence and to calculate the height of the step-edge barrier. However, supplementary ideas have to be taken into account when applying a model, which was designed for atoms, to large organic molecules with more degrees of freedom.

3 Film-substrate systems

This chapter shortly describes the used organic adsorbate molecules as well as the used single-crystalline substrates. The investigated systems can be divided into

- The rod-like molecule p6P on insulating substrates (mica, KCl)
- The disc-shaped molecule HATCN on noble metals (Au, Ag)

3.1 A rod-like molecule: The conjugated organic semiconductor para-hexaphenyl (p6P)

Hexaphenyl (p6P, frequently denoted as sexiphenyl) is the term used for a molecule that consists of six phenyl rings (chemical formula $C_{36}H_{26}$). In the case of para-hexaphenyl the phenyl rings are aligned in a row, forming thus a rod-like molecule. The electronic and optical properties of this molecule are related to the properties of other rod-like oligophenylenes (pnP) and are governed by their conjugation, which is an intrinsic property of all phenylenes. Regarding hydrocarbons, the term 'conjugation' describes the molecular property of having alternating carbon single- and double bonds, which causes $sp^2 + p_z$ hybridization [69, 70, 71]. The carbon sp^2 orbitals are exclusively involved in building up the backbone of the molecule, which determines the geometric structure and mechanical properties. The carbon p_z electrons, however, are delocalized across the conjugated area of the molecule to form extended π-orbitals [71]. Thus, the corresponding electrons are often denoted as π-electrons. A prototypical example of a conjugated organic molecule is benzene. Conjugated materials often exhibit a low electronic band gap between the HOMO and the LUMO, which gives rise to semiconducting behavior. In the case of hexaphenyl, the band gap is $\approx 3.1\ eV$ [72, 73], which is often described as wide-gap semiconducting behavior. The van der Waals dimensions of a single molecule are $2.85 \times 0.35 \times 0.67\ nm^3$. The atomic mass of a p6P molecule is 458.59 *amu* [74]. **Fig. 1a** shows a single p6P molecule in the planar configuration. The p6P bulk crystal structure at room temperature is monoclinic [75, 76] and well-known as

herringbone structure, which is characteristic not only of the pnPs, but also of various other conjugated aromatic molecules. In **Fig. 1b** the arrangement of 10 p6P molecules in the unit cell is depicted. A very detailed description of oligophenylenes at large and in particular of p6P can be found in ref [71].

Fig. 3.1: Single p6P molecule in the planar conformation. From [77].

3.2 A disc-shaped molecule: The organic molecular acceptor hexaaza-triphenylene-hexacarbontrile (HATCN)

HATCN is the term used for a disc shaped molecule with the chemical forumla $C_{18}N_{12}$ (see scheme in **Fig. 3.2**). The conjugated heterocycles determine the physical and chemical properties of the molecule. Therefore this molecule is a strongly electron-deficient heterocycle which as a consequence of that avoids π-stacking [58]. Thus the crystal structure is characterized by perpendicular CN-π interactions, leading to a very complicated 3D hexagonal arrangement [58, 59] (**Fig. 3.3**) with 18 molecules in the unit cell.

HATCN is assigned to the group of cyano-based acceptor molecules like tetracyanoethylene (TCNE) [78] or tetracyanoquinodimethane (TCNQ) [79] and its derivates. The major drawback of conventional cyano-based molecular acceptors is their rather low molecular weight, which implicates poor thermal stability of the grown structures. For F4-TCNQ ($m = 280.18\ amu$) this has already been shown to be a problem in devices [57]. Therefore molecular electron acceptors with higher thermal stability (which means to a first approximation a higher molecular weight) are desired. Thus the disc-shaped molecule HATCN ($m = 384.29\ amu$) is a promising novel molecular acceptor material which could be used to reduce the hole injection barrier of metals by increasing the work function to a great extent.

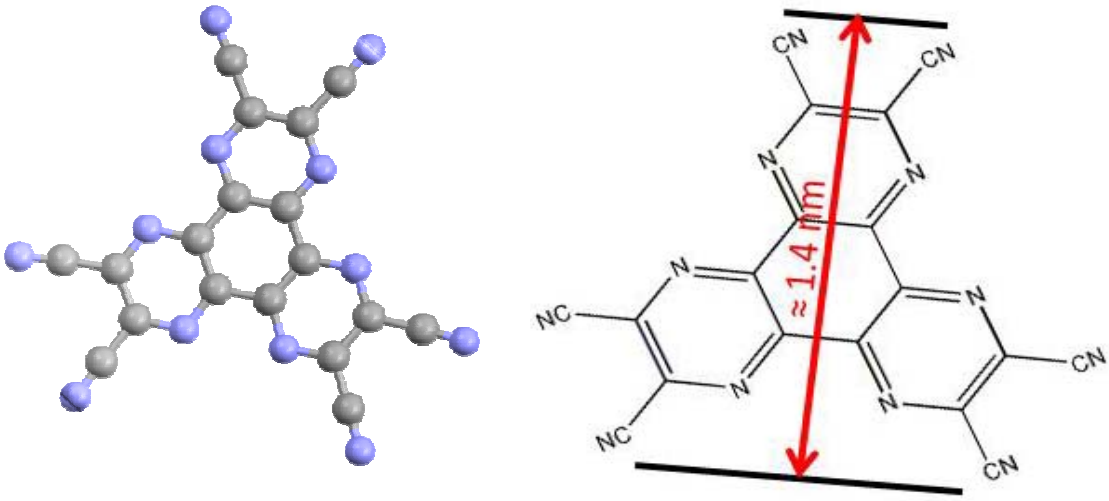

Fig. 3.2: Schematic views of the HATCN molecule. **Left:** Simple ball model of HATCN, carbon atoms in grey and nitrogen atoms in blue. **Right:** Chemical structure of HATCN showing the conjugation of the heterocycles which defines the chemical and physical properties of this molecule. In red: diameter including van der Waals radii.

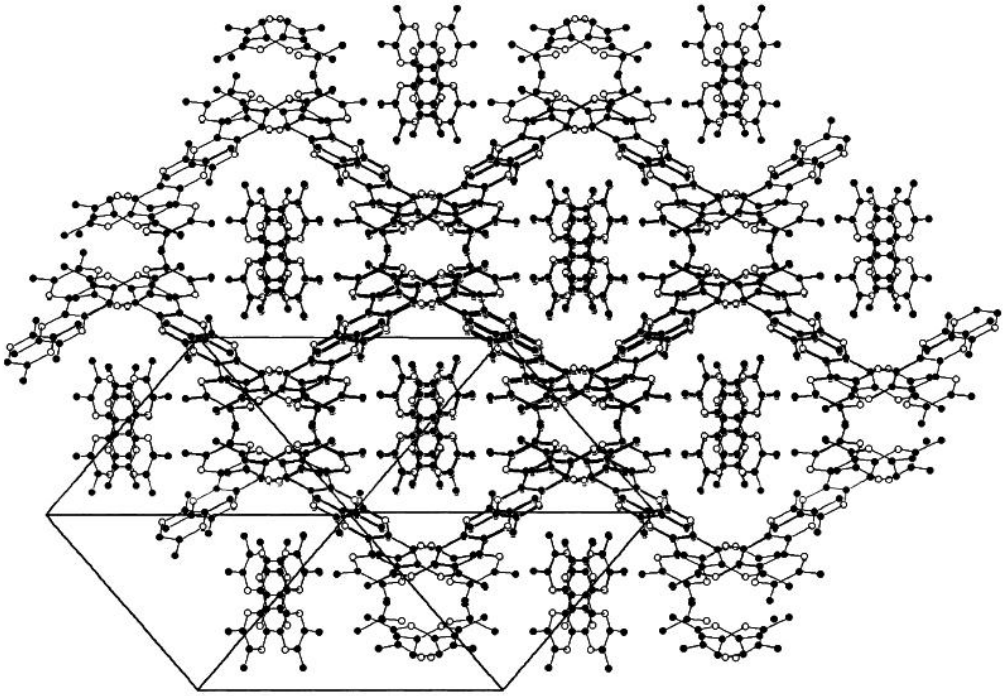

Fig. 3.3: View of the 3D bulk structure of HATCN. From [58].

3.3 Substrates

3.3.1 The mica (001) surface

For all the experiments presented in chapter **5 Hexaphenyl on mica (001)** muscovite mica with the chemical formula

$$KAl_2(AlSi_3O_{10})(OH,F)_2$$

has been used. A detailed description of the mica crystal structure can be found in refs [77, 80, 81].

The mica was available in sheets of several square centimeters. After cutting out a quadratic piece of $10 \times 10\ mm^2$ the mica was cleaved under ambient atmosphere conditions with a scotch tape and quickly transferred into the ultra-high vacuum chamber. In the section **4.3.2 Experimental implementation** the mounting of the mica substrates onto the sample holder is described in detail.

3.3.2 The KCl (001) surface

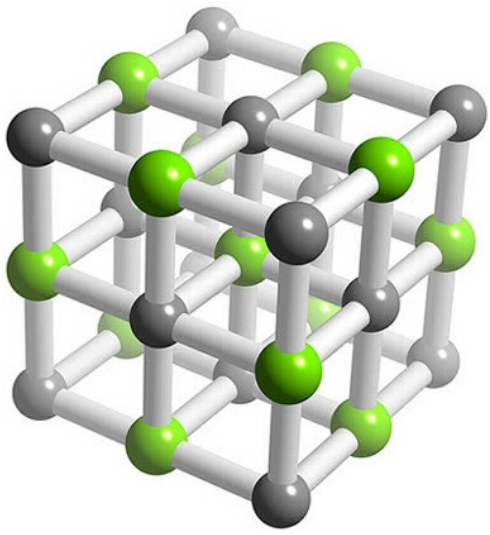

Fig. 3.4: Na-type KCl structure.

Potassium chloride has a crystalline structure like many other salts. Its structure is face-centered cubic (**Fig. 3.4**) with a lattice constant of about 6.3 Å [81]. The KCl specimens were prepared by cleaving a KCl block into pieces of $10 \times 10 \times 1\ mm^3$ with a razor blade. The small KCl plates were mounted onto the sample holder in a similar way as the mica samples. KCl is frequently used as a substrate in organic thin film investigations because it has an atomically well-defined surface. The surface has a four-fold symmetry which leads to a four-fold symmetry of the epitaxial relationships of the grown organic films.

3.3.3 The Au (111) surface

The gold bulk crystal structure is face-centered-cubic (fcc) with a lattice constant of about 4.08 Å. The idealized Au (111) surface has a 6-fold symmetry (hexagonal). However, considering the first and second topmost atomic layers, the symmetry of the surface structure reduces to a 3-fold rotational symmetry. The inter-atomic distance of the ideal Au (111) surface is $a_{111} = 2.88$ Å and the inter-row distance is $d_{111} = 2.49$ Å .

Gold is the only fcc metal whose (111) surface reconstructs [82]. The driving force behind this reconstruction is the relief of surface stress. Along the [1-10] direction an average 4.2% contraction of the topmost surface layer with respect to the underlying layer is found. In other words, the topmost atomic layer features along the [1-10] direction atomic rows where 23 atoms align on the same length as 22 atoms in the underlying layer. This surface reconstruction can be explained by a rectangular (22 x √3) surface unit cell. More detailed information on the reconstruction of the Au (111) surface can be found in refs [71, 82].

3.3.4 The Ag (111) surface

The silver bulk crystal structure is very similar to gold, namely fcc with a lattice constant of ≈ 4.09 Å. The inter-atomic distance of the ideal Ag (111) surface is $a_{111} = 2.89$ Å and the inter-row distance is $d_{111} = 2.50$ Å . The idealized Ag (111) surface has a hexagonal symmetry and does not exhibit a surface reconstruction.

4 Analytical methods & instrumentation

Most of the experimental results shown in this work were produced in our laboratory, except for scanning electron microscopy (SEM), X-ray diffraction (XRD) and part of the atomic force microscopy (AFM) measurements, which were carried out by our partner groups in Bratislava, Graz and Leoben, respectively. While AFM was performed ex-situ under ambient atmosphere conditions, thermal desorption spectroscopy (TDS), X-ray photoelectron spectroscopy (XPS), Auger electron spectroscopy (AES) and Kelvin probe (KP) experiments had to be accomplished under ultra-high vacuum (UHV) conditions. All these UHV experiments were conducted in our laboratory.

4.1 The UHV chamber

A schematic view as well as a more detailed description of the chamber and the sample holder can be found in ref [71]. The base pressure in the UHV chamber could reach $\approx 10^{-10}\ mbar$ after bake-out. The UHV was generated and maintained by rotary pumps and turbo pumps and monitored via a *Ionivac IM 520* ionisation gauge.

The sample was placed on a turnable sample holder which was located in the center of the chamber. The sample holder could be cooled down to about $100\ K$ via a liquid nitrogen cooling finger attached to the sample holder. The above mentioned surface probing devices and a sputter gun for specimen cleaning were arranged within a measuring plane and could be addressed by rotating the sample holder.

4.2 Thin film preparation by organic molecular beam epitaxy (OMBE)

The organic thin films were prepared by organic molecular beam epitaxy (OMBE) within the UHV chamber described in the previous section. For this purpose a home-built evaporation source containing a Knudsen-cell was applied, which has already been described in detail in refs [71, 80, 95]. This source has so far only been used for para-quaterphenyl (p4P) and para-hexaphenyl (p6P) evaporation, but could also be used for the preparation of HATCN films because the vaporization temperature of HATCN and p6P did not differ too much from each other. However, the HATCN powder as received contained residual solvents, which had to be eliminated before the HATCN source could be used for experiments. Details on the cleaning procedure can be found in section **7.1 Purification of HATCN and its cracking pattern**.

The film thickness was monitored via a quartz microbalance (*Inficon Inc.*) which was permanently positioned about 30° off the axis of the Knudsen source. The microbalance allowed an in-situ control of the evaporation rate. For the calibration of the impingement rate on the sample, the latter had temporarily been replaced by a second quartz microbalance, as described in ref. [80, 95]. The geometric factor

$$G = \frac{\Delta f_2}{\Delta f_1} \tag{4.1}$$

(Δf_2: frequency change of the microbalance replacing the sample, Δf_1: frequency change of the permanently positioned microbalance) turned out to be $G = 1.05$, showing that approximately the same amount of material impinges on the sample as on the permanently positioned microbalance. There is a simple relationship between the absolute mass thickness (Δm) and the frequency change (Δf) of the microbalance

$$\Delta m = -\frac{1}{S} \cdot \frac{\Delta f}{f^2} \tag{4.2}$$

Which yields for given S (integral mass sensitivity, given by the manufacturer [96]),

$$S = 2.273 \cdot 10^{-8} \frac{cm^2 s}{g} \tag{4.3}$$

$G = 1.05$ and a frequency of

$$f = 5.96 \cdot 10^6\ Hz \tag{4.4}$$

$$\xrightarrow{yields} \Delta m\left[\frac{\mu g}{cm^2}\right] \approx 0.0130 \cdot \Delta f\ [Hz] \tag{4.5}$$

The numerical value in this simple relation is slightly different from that in ref [80] because the frequency of the quartz microbalance has changed due to the huge number of organic layers evaporated on the crystal during the last years. Using the molecular mass of a single p6P or HATCN molecule ($m_1p6P = 458.6\ amu$, $m_1HATCN = 384.3\ amu$) certain mass thickness values in $\frac{molecules}{cm^2}$ have been obtained that are equivalent to a frequency change of $\Delta f = 1\ Hz$. Based on the density values of p6P and HATCN ($\rho_1p6P = 1.288\ g/cm^3$. $\rho_1HATCN = 1.6\ g/cm^3$) [58], one can additionally calculate the equivalent mean film thickness. The corresponding values are summarized in **Table 4.1**.

Molecule	$\Delta m\ \left(\frac{molecules}{cm^2}\right)$	$d\ (nm)$
p6P	$1.7 \cdot 10^{13}$	0.10
HATCN	$2.0 \cdot 10^{13}$	0.08

Table 4.1: Values of mass thickness Δm and mean film thickness d equivalent to a frequency change of the quartz microbalance of $\Delta f = 1\ Hz$ upon deposition of a p6P or HATCN film.

4.3 Thermal desorption spectroscopy (TDS)

TDS is a surface science technique which can be used to study adsorption and desorption properties of adsorbates on heated sample surfaces. After depositing a known amount of the material to be analyzed, the sample is heated with a constant heating rate and the partial pressures of atoms and molecules coming from the sample are measured.

4.3.1 Theoretical background

The most commonly used approach for describing the thermal desorption rate of an adsorbed species is the Polanyi-Wigner equation [97]

$$r_{des} = -\frac{d\theta}{dt} = \nu_n \cdot \exp\left(\frac{-E_{des}}{RT}\right) \cdot \theta^n \qquad (4.6)$$

This equation describes the correlation between the desorption rate (r_{des}) and the coverage (θ), temperature (T) and the so-called kinetic parameters v, n and E_{des} which will be explained in detail in the following. Before that, it is necessary to mention that this approach to thermal desorption spectroscopy only holds if the pumping speed is constant and sufficiently high in order to prohibit significant readsorption of desorbed particles on the sample.

To start with, the parameter v is the so-called pre-exponential factor or frequency factor (unit is s^{-1}) of the desorption process with the order n. According to transition state theory (TST) [98, 99], this frequency factor can be expressed in terms of the molecular partition functions in the transition state ($q^{\ddagger}$) and in the initial (adsorbed) phase (q_{ads}) for non-associative molecular desorption, calculated at temperature T

(4.7)

Note that the degree of freedom along the reaction coordinate (normal to surface) is omitted

from the calculation of . In the case of a desorption process with no activation barrier to adsorption, as it is usually the case for large organic molecules, the transition state is equivalent to the final state of the molecule. The final state is the gas phase without this one degree of freedom normal to the surface [100]. In common TDS experiments of small molecules (e.g. CO, N_2, H_2), the ratio of the partition functions is commonly assumed to be nearly unity (i.e. entropy is nearly the same in gas and adsorbed states), in which case the above expression gives a pre-exponential factor of about $10^{13}\ s^{-1}$ for room-temperature desorption. However, for large organic molecules (in that case n-alkanes) recent molecular dynamics und transition state theory calculations [102] predict a significant increase of the pre-exponential factor with chain length, which is attributed to increasing differences between the adsorbate and transition state entropies. This occurs because the adsorbed molecules are relatively hindered in translational and/or rotational degrees of freedom compared to the gas

phase. Upon desorption, the vibrational modes associated with the hindered translations and rotations in the adsorbed state will be converted to free translational and rotational modes in the gas phase. These free motions will contribute much more to the partition function than the vibrations in the adsorbed state and the ratio $\frac{q^{\ddagger}}{q_{ads}}$ can be very large. An attempt to quantify the translational and the rotational partition function for several n-alkanes (which can be seen as model systems for other large organic molecules) has been undertaken by Tait et al. [100]: They assume that in the transition state the molecules behave as a freely rotating 3D gas. They are considered to be rigid rotors in the gas phase i.e. they have three translational and three rotational degrees of freedom. Upon adsorption at low temperature, all six degrees of freedom become vibrational modes, the so-called hindered rotations. At the desorption temperatures, however, the corresponding energy barriers may be small compared to $k_B T$, so that these motions may be effectively 'free'. This depends on the corrugation of the interaction potential, a detailed knowledge of which would be required to determine the true nature of the adsorbate motion. Since detailed knowledge of the interaction potential is lacking, certain assumptions about the degrees of freedom of the molecules in the adsorbed state have to be made. Tait et al. calculate the pre-exponential factors for two extreme cases: ν_{max} by assuming immobile adsorbate molecules and ν_{min} by assuming a corrugation-free surface and find the experimentally obtained values for n-alkanes to lie between the calculated ν_{max} and ν_{min}, but outside the respective errors. The best fit to the experimental pre-exponential factors is in fact gained if it is assumed that the molecules behave translationally like a 2D gas, but all rotation is prohibited. However, the authors of that work state that this model is not intended to provide an accurate physical picture of the desorption system since it is hard to imagine a real adsorbate/substrate system where the interaction potential allows completely free translation of the adsorbate but no rotation at the same temperature. Rather their aim is to illustrate that the large increase in pre-exponential factor of n-alkanes with chain length can be accounted for entirely by considering the increase in rotational entropy available to the molecules in the gas-phase-like transition state.

In conclusion one can say that there is substantial experimental [21, 71, 100, 101] and theoretical [102, 103] evidence that the desorption rate of large organic molecules is in fact determined by very large pre-exponential factors compared to the commonly used value of $10^{13}\ s^{-1}$.

The desorption order, denoted as index *n* in eq. (4.6), determines the influence of the coverage on the shape of the TD-spectra. Typical values for *n* are

n = 0: The desorption rate does not depend on the coverage, which is fulfilled for desorption from a homogeneous multilayer film. The desorption rate increases exponentially with the temperature. After all the molecules from the multilayer have desorbed, there is a steep descent in the spectrum. Therefore the peak maximum shifts to higher temperatures for increasing coverage.

n = 1: The desorption rate is proportional to the coverage Θ. This holds for a limited reservoir of particles when single atoms or molecules desorb directly, separately and independently from their adsorption sites. The spectra feature a characteristic asymmetric peak shape. In contrast to zero order desorption, the peak maximum stays at the same temperature for any coverage.

n = 2: The desorption rate is proportional to Θ^2. This is a typical order for associative desorption processes where the adsorbed atoms or molecules need to find a reaction partner in order to desorb from the surface (e.g. hydrogen on various substrates). The peak shape is nearly symmetric and the peak maximum shows a characteristic shifting to lower temperatures with increasing coverage.

The last kinetic parameter which has to be discussed is the desorption energy, denoted as E_{des} in eq. (4.6). This is the energy that is needed to surmount the surface potential barrier and is therefore also often referred to as the activation energy for desorption. The desorption energy can also be coverage-dependent, which is for instance the case if lateral interactions between the adsorbed molecules exist. The interaction energy between the adsorbate species can either be repulsive or attractive, leading to a decrease or an increase of the activation energy, respectively. Examples for the influence of repulsive interactions can be found in the literature on TDS of large organic molecules [71], where repulsive Van-der-Waals interactions are likely to occur. The decrease of E_{des} with increasing coverage leads to shifts in the spectra to lower temperatures in the monolayer regime. Although this is characteristic for second order desorption kinetics, the desorption order in this case is still $n = 1$.

As the last part of the theoretical section on TDS some standard procedures that were used to directly obtain the kinetic parameters from a single or a series of measured spectra are presented.

- **Leading edge analysis**

This method allows the determination of coverage- and temperature-dependent activation parameters. To keep the temperature and the coverage constant, a small section of the spectrum on its leading edge is selected [104]. This part of the spectrum is then plotted as $(\ln r_{des})$ vs. $\frac{1}{T}$, according to the logarithmic Polanyi-Wigner equation

$$\ln r_{des} = -\frac{E_{des}}{RT} + \ln \upsilon_n + n \cdot \ln \theta \qquad (4.8)$$

From the slope of this Arrhenius plot E_{des} can be determined. From the intercept with the ordinate the frequency factor can be determined provided that reaction order and coverage are known. For this purpose it is necessary to calibrate the y-ordinate of the spectra correctly. This method is applied to zero order desorption spectra and can also be applied to first order desorption spectra in the region, where the desorption rate increases exponentially ($\theta \approx const.$), i.e. if one only uses the leading edge for analysis.

- **Analysis according to Redhead**

A rather simple relation between the kinetic parameters was proposed by Redhead [97]: If desorption follows first order kinetics and the parameters are independent of the coverage, the desorption energy can be approximated by

$$E_{des} = RT_{max} \cdot \left(\ln \frac{\upsilon_1 \cdot T_{max}}{\beta} - \ln \frac{E_{des}}{RT_{\max}} \right) \qquad (4.9)$$

The second part in the brackets is small relative to the first and is estimated as $ln\left(\frac{E_{des}}{RT_{\max}}\right) = 3.64$. $T_{\max}$ is the temperature at the peak maximum and υ_1 is the frequency factor for first order desorption, which has to be known. If the frequency factor for first order desorption is unknown, customary approaches for υ_1 are either to

take the commonly chosen value of $\upsilon_1 = 10^{13} s^{-1}$, which is, as mentioned before, not recommendable for large organic molecules, or to assume $\upsilon_0 \approx \upsilon_1$ and insert the value of the frequency factor for zero order desorption, which is easily gained by the above mentioned leading edge analysis. However, in systems where the multilayer growth is significantly different from the monolayer growth, this assumption does not have to be correct: In the case of HATCN on Au (111) it turned out that the frequency factors of the first monolayer and of the multilayer differ by six orders of magnitude (see sections **5.2** & **5.3**).

- **Heating rate variation method**

If a reliable approximation for υ_1 is not available or possible, a more detailed analysis than the above presented is inevitable. The heating rate variation method is based on the collection of a series of spectra for the same adsorbate coverage utilizing different heating rates [97]. Starting with eq. (4.6), one can get the following relation for first order desorption:

$$\frac{E_{des}}{RT_{max}^2} = \frac{\upsilon_1}{\beta} \cdot \exp\left(-\frac{E_{des}}{RT_{max}}\right) \quad (4.10)$$

Taking the logarithm and rearrangement yields

$$\ln(T_{max}^2/\beta) = E_{des}/(RT_{max}) + \ln(E_{des}/(R \cdot \upsilon_1)) \quad (4.11)$$

Plotting of $\ln(T_{max}^2/\beta)$ vs. $\frac{1}{T_{max}}$ for a series of β -values thus yields E_{des} from the slope and υ_1 from the intercept with the ordinate.

4.3.2 Experimental implementation

After the preparation of thin films in ultra-high vacuum (UHV) with a well-known thickness on the used samples, they were heated by resistive heating. The single crystals Au (111) and

Ag (111) used in this work exhibited a circular groove (like shown in **Fig. 4.1** on the **right**) running around their side walls, where the Ta wires could be wound around for mounting purposes. The mica and KCl sheets were heated by pinning them to a steel plate (**Fig. 4.1** on the **left**), which was also heated by resistive heating. The temperature was in all cases measured by a Ni/NiCr thermocouple spot-welded on the backside of the single crystals or on the back side of the steel plate and controlled by a LABVIEW program, which allowed maintaining a constant temperature or a linear heating of the samples. Details on the peculiarity of doing TDS with samples with poor thermal conductivity like mica can be found in chapter **5 Hexaphenyl on mica (001)**.

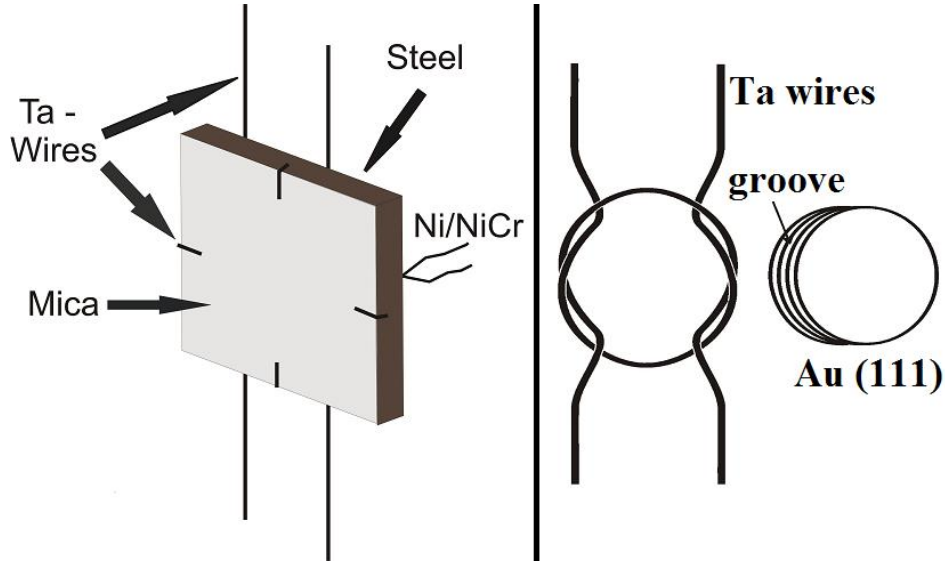

Fig. 4.1: Heating of the samples either by pinning to a heated steel plate (**left**) or by direct resistive heating (**right**). Temperature in both cases measured with a Ni/NiCr thermocouple.

TDS was performed by desorbing the adsorbed molecules into a multiplexed line-of-sight quadrupole mass spectrometer (QMS), which was tuned to the most relevant masses. The QMS 400 (by Pfeiffer Inc.) was equipped with a magnetic field enhanced cross-beam ion source and could detect a mass range of $1-512\ amu$. For both used molecules (p6P, HATCN) it was observed that the mass of the intact molecule did not show the highest QMS signal and therefore not the best signal to noise ratio. Usually, better signals were found for distinctive masses much smaller than the mass of the intact molecule. The reason for that is either cracking of the intact molecules in the QMS during the ionization process (the used ionization energy was rather high: $E_I = 70\ eV$, which led to a strong dissociation of the large molecules) or cracking of the molecules on the surface during the desorption process. The

latter will occur if strong interactions between the adsorbed molecules and the substrate surface exist. In chapter **7 HATCN on Ag (111)** an example of the observation of both cracking processes is given and it is shown how the two cracking processes can easily be distinguished.

4.4 X-ray photoelectron spectroscopy (XPS)

One of the most frequently used methods to probe the chemical composition of a sample surface is XPS, often also denoted as electron spectroscopy for chemical analysis (ESCA). This method involves irradiation of a solid in the vacuum with monoenergetic soft X-rays and sorting the emitted photoelectrons by their kinetic energy.

$$E_{kin} = h\upsilon - E_{Bind} - \phi_s \tag{4.12}$$

φ_s is the work function of the spectrometer. The kinetic energy E_{kin} of photoelectrons emitted upon irradiation of the sample with photons with a known energy of $h\upsilon$ depends on the binding energy of the involved photoelectron state E_{Bind} and is therefore characteristic for each element and thus allows to identify the components of the sample surface. The fundamental process of generating photoelectrons is illustrated in **Fig. 4.2**. The spectrum obtained is a plot of the number of emitted electrons as a function of their kinetic energy. Further details on this technique can be found in the literature [105-107].

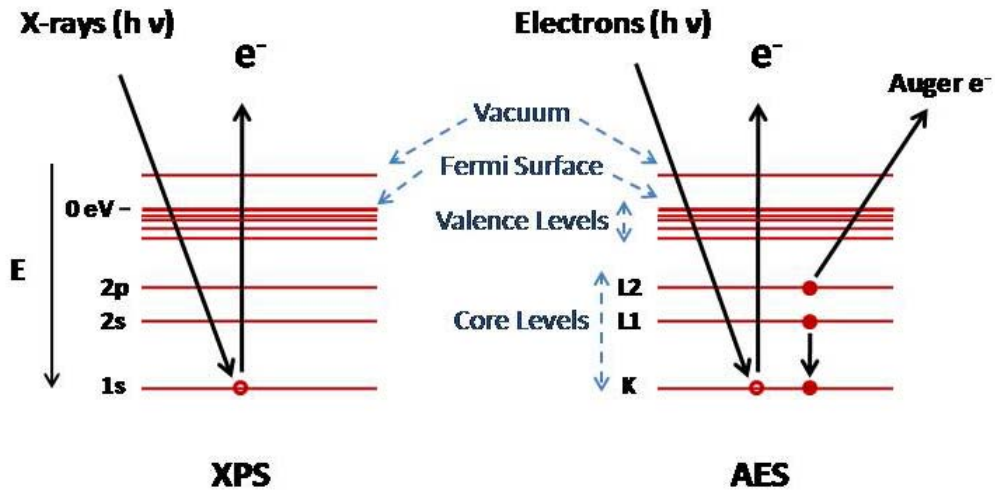

Fig. 4.2: Schematic view of the X-ray induced photoelectron (**left**) and the electron beam induced Auger electron (**right**) emission. From [108].

For the realization of the XPS experiments, a combined XPS/AES system by *Leybold Inc.* containing a concentric hemispherical analyzer (CHA) was used. The X-ray source could be switched between Mg K_α ($1253.6\ eV$) and Al K_α ($1486.6\ eV$) radiation. Standard operating parameters were a source voltage of $10.5\ kV$ and an emission current of $30\ mA$.

4.5 Auger electron spectroscopy (AES)

The Auger electron spectroscopy technique for chemical analysis of surfaces is based on the Auger radiationless process. When a core level of a surface atom is ionized by an impinging electron beam, the atom may decay to a lower energy state through an electronic rearrangement. The energy difference of these two states is given to the ejected Auger electron which has a kinetic energy characteristic of the parent atom. The kinetic energy can be approximated in the following way

$$E_{kin} \approx E_K - E_{L1} - E_{L2} - \phi_S \qquad (4.13)$$

φ_s is the work function of the spectrometer. E_K is the primarily ionized electron level, E_{L1} and E_{L2} are the higher energy levels that are involved in the process. An illustration of this process is shown in **Fig. 4.2**. More details on this well-known technique can be found in refs [105-110].

The electron gun for AES was operated with an emission current of $0.1\ mA$ and the beam voltage was usually in the range of $1500\ eV$ to $2500\ eV$. As mentioned in section (XPS), a CHA was used to analyze the kinetic energy of the secondary electrons coming from the sample. A lock-in amplifier was used to uncover the Auger electrons and to attenuate the usually high background in the secondary electron spectrum.

4.6 Atomic force microscopy (AFM)

The atomic force microscope is a very useful tool for imaging very small areas of all types of surfaces. Unlike scanning tunneling microscopy (STM), AFM is not restricted to electrically conducting surfaces [107, 111]. In this technique, the probe is a small sharp tip which is

scanned very closely across the sample surface. The distance between the tip and the sample is so small that atomic-range forces act between them. In order to measure these forces, the tip is attached to the end of a cantilever. The deflection of the cantilever, which depends on the forces acting on the tip, can be determined using a laser beam deflection system (see **Fig. 4.3**). AFMs can be used in so-called static and dynamic operating modes, which are also often denoted as contact and tapping mode, respectively. In order to image soft organic films, the non-contact tapping mode was utilized, because the forces acting on the presumably soft films during contact-mode AFM could influence their structure.

In the tapping mode, the cantilever is driven to oscillate up and down at a frequency near its resonance frequency using a piezo element. The interaction of forces acting on the cantilever when the tip comes close to the surface (van der Waals force, dipole-dipole interaction, electrostatic forces, etc) causes the amplitude of this oscillation to decrease as the tip gets closer to the sample. The vibration of the cantilever is detected using the laser beam deflection system. The measured laser beam deflection or cantilever vibration amplitude can now be used as an input for a feedback loop that keeps the tip-sample interaction (i.e. cantilever oscillation amplitude) constant by changing the tip height as the cantilever is scanned over the sample. The output of this feedback loop thus corresponds to the local sample height. Further details on the dynamic operating mode can be found in refs [112, 113].

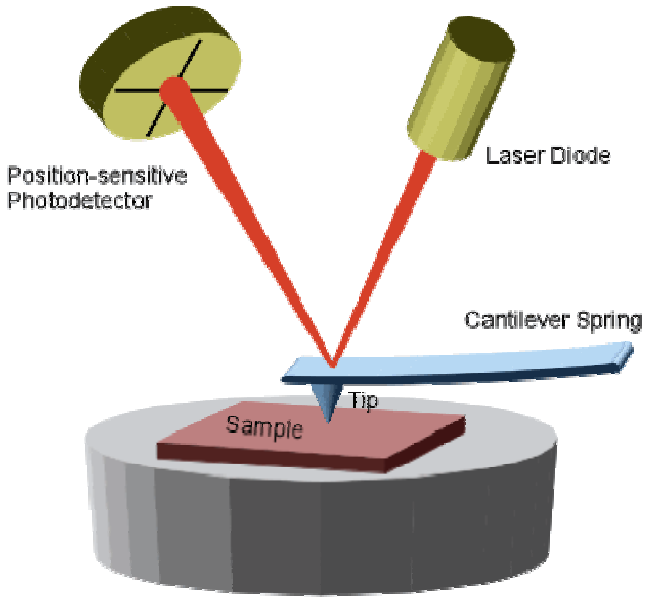

Fig. 4.3: The principle of atomic force microscopy (AFM). From [114].

The AFM measurements presented in this work were carried out in tapping mode under ambient atmosphere conditions, which inhibited even close to atomic resolution. However, the obtained resolution was good enough for imaging the rather large structures formed by the organic molecules. Most of the AFM investigations were done utilizing a *Nanosurf easyScan 2 AFM system*. Early AFM measurements (all p6P on mica images) were performed with a *Nanoscope Multimode IIIa scanning probe microscope (Digital Instruments Inc., Santa Barbara, CA)* equipped with an AS-130(J) scanner. This instrument was located at the Institute of Physics at the University of Leoben. In both cases, conventional Si-tips were used.

4.7 Kelvin Probe (KP)

The Kelvin Probe is a non-contact, non-destructive vibrating capacitor device used to measure the work function difference between a conducting specimen and a vibrating tip [115-119]. When two materials with different work functions are brought together, electrons in the material with the lower work function flow to the one with the higher work function. If these materials are made into a parallel plate capacitor, equal and opposite surface charges form. The voltage developed over this capacitor is called the contact potential, which is the difference between the work functions of the participating materials, and measuring it is done by applying an external backing potential to the capacitor until the surface charges disappear. At that point the backing potential will equal the contact potential. The tip and the sample do not need to touch each other and only very weak electric fields are required, which are not likely to influence the electrical or chemical structure of the material.

As explained above, the output of a Kelvin Probe measurement is not the work function of the sample itself, but the work function difference between the tip and the specimen. In order to obtain the absolute work function of the sample thus the work function of the tip has to be known. A standard procedure to determine the work function of the vibrating tip utilizing a gadolinium foil is presented in refs [120, 121].

All the KP measurements were carried out under UHV conditions with a built-in Kelvin Probe *(KP Technology Inc.)* equipped with a stainless steel tip. A photograph of the UHV Kelvin Probe is shown in **Fig. 4.4**.

Fig. 4.4: Photograph of the UHV Kelvin Probe.

5 Hexaphenyl on mica (001)

This chapter presents a detailed survey of the adsorption/desorption kinetics, structure, growth and morphology of ultra-thin p6P films on muscovite mica (001). Frequently for the description of the hexagonal mica surface instead of *Miller indices* the *Bravais-Miller indices* are used. In that case four axes are used and four *Miller indices* (hkil → mica (0001)), in which the parameters h,k,i are cyclically permutable and related by $h + k + i = 0$. As it turned out, the existence of a so-called 'wetting layer' affects the further film growth in a tremendous way. In this work, the term 'wetting layer' is used when there exists a monomolecular monolayer of molecules lying flat on the surface. A very common way to inspect the monolayer regime and thus to check whether a monolayer exists or not is TDS. Additional information on the initial thin film growth can be gained by combining XPS with TDS, i.e. monitoring the change of the XPS signal during heating up the sample. The morphology of thicker films was investigated by AFM and scanning electron microscopy (SEM).

The chemical and structural condition of the mica substrates also has an enormous effect on the thin film growth. In the following, thin films will be characterized which were grown on clean mica (**5.2**-**5.4**), on carbon contaminated mica (**5.5**) and on sputtered mica (**5.6**). XPS and low energy electron diffraction (LEED) were used to characterize the mica surface before the film deposition.

5.1 Calibration of the TD spectra

As shown in section **4.3.2**, the mica sheets were mounted on a heated steel plate, on the back side of which the temperature was measured. A drawback of this experimental setup was that because of the poor thermal conductivity of mica, the measured temperature did not represent the temperature on the mica surface properly and therefore the temperature scale had to be corrected. An uncorrected TD-spectrum for a p6P film with $30\ nm$ thickness is shown in **Fig. 5.1**. There exist two desorption peaks, one due to the desorption from the tantalum wires, which were used to fix the sample to the steel plate (see insert in **Fig. 5.1**), which are also

covered with p6P during the evaporation process, and one due to the desorption from mica. As a first approximation, it is assumed that the multilayer desorption peak should be independent of the substrate and hence desorption from tantalum should occur in the same temperature range as desorption from mica. Therefore the temperature scale was corrected utilizing a linear regression between two characteristic temperatures. At the adsorption temperature of $T_{ads} = 300\ K$ both materials will be at the same temperature. When heating up, the mica sample temperature will increase more slowly than that of the steel plate and this will result in a deviation which increases during heating. The second characteristic temperature is the starting point of the multilayer desorption of p6P from mica. Keeping in mind the assumption above, the measured $625\ K$ (where desorption from mica starts) can be assigned to $450\ K$ (where desorption from the tantalum wires starts). This fits quite well to p6P multilayer desorption from another metal surface, namely Au (111) [20, 21, 71]. All TD-spectra shown in the following sections are displayed with the corrected temperature scale.

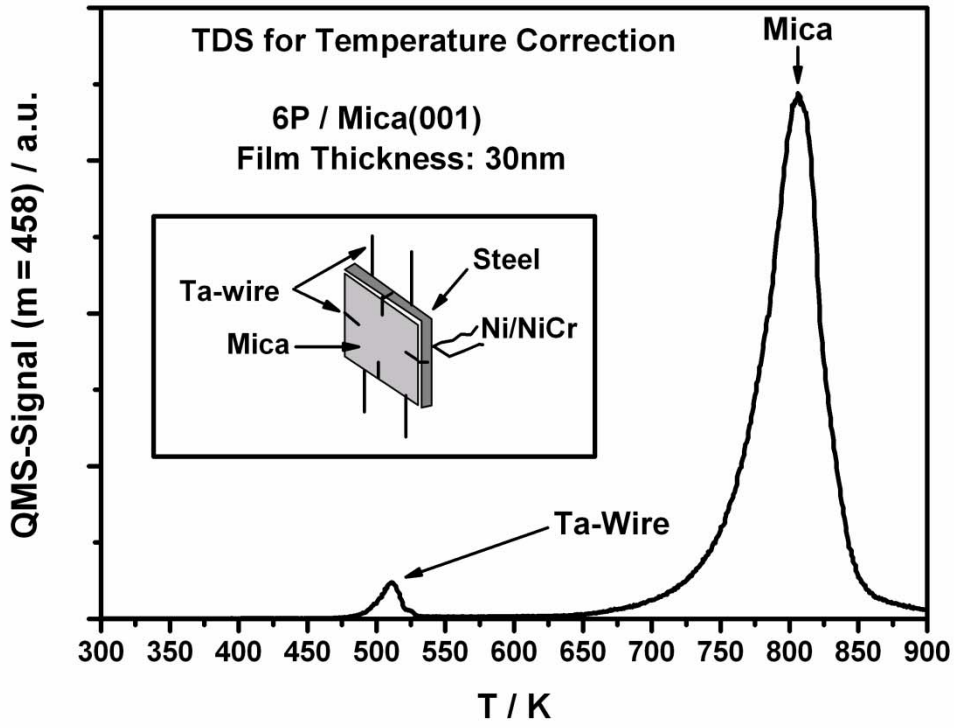

Fig. 5.1: TD-spectrum of $30\ nm$ p6P on mica (001), adsorption temperature $T_{ads} = 300\ K$. This spectrum was used to calibrate the temperature scale. The insert shows the sample mounting.

5.2 Freshly air-cleaved mica (001)

The surface composition and structure of a freshly cleaved mica (001) surface, after quickly transferring it into the UHV chamber and pumping down, was checked by XPS and LEED, respectively. LEED showed the well-known 6-fold symmetric pattern without spot-splitting (**Fig. 5.2**). Such a spot-splitting has been observed only for vacuum cleaved mica [122, 123].

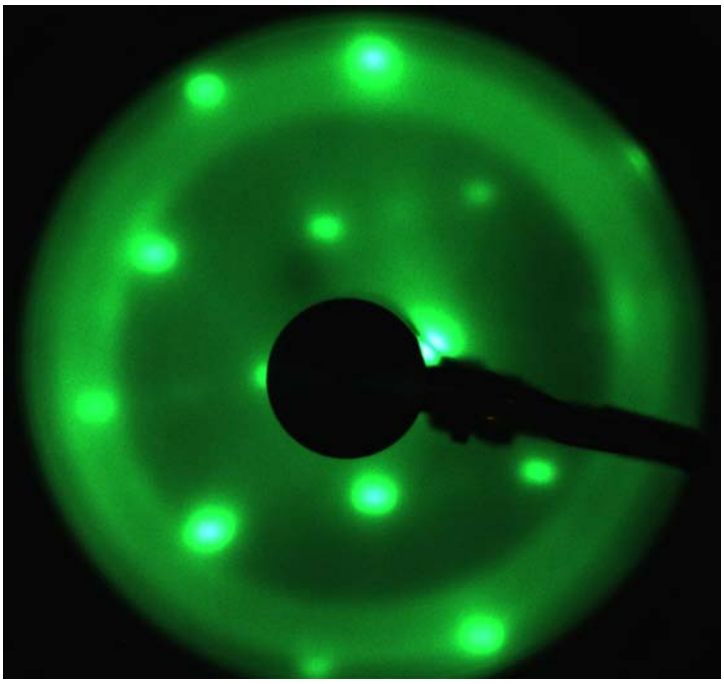

Fig. 5.2: LEED pattern of freshly cleaved mica; taken at 103 V .

XPS revealed that the surface was not completely clean. The spectra shown in **Fig. 5.3** and **Fig. 5.4** stem from a freshly air-cleaved mica surface, on which, in agreement with previous AES investigations [124] of air-cleaved mica, some amount of carbon can be observed. It was found that there is carbon on the surface whenever mica is cleaved in air. The supposed [124] reason for that is an adsorption process which requires carbon compounds and water. The amount of carbon contamination may depend on the time it takes to get the mica into (ultra) high vacuum conditions after the cleavage in air. An attempt to quantify this amount will be discussed in section **5.5 p6P on carbon contaminated mica (001)**.

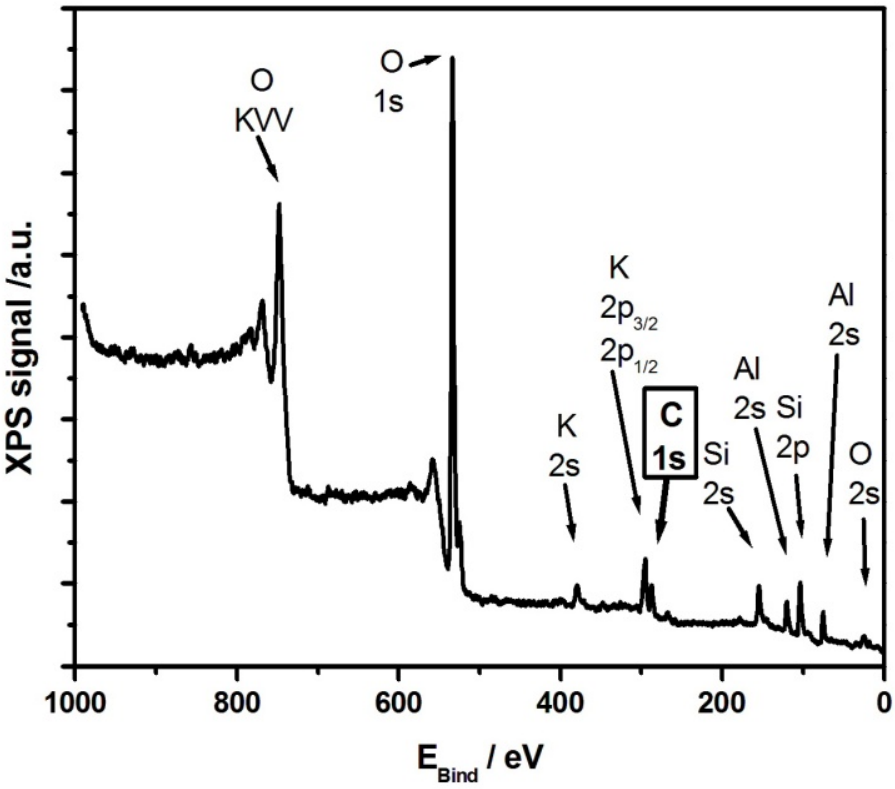

Fig. 5.3: XPS overview spectrum of mica after cleaving in air and subsequent pump-down of the chamber. The C1s peak can clearly be seen even in the overview.

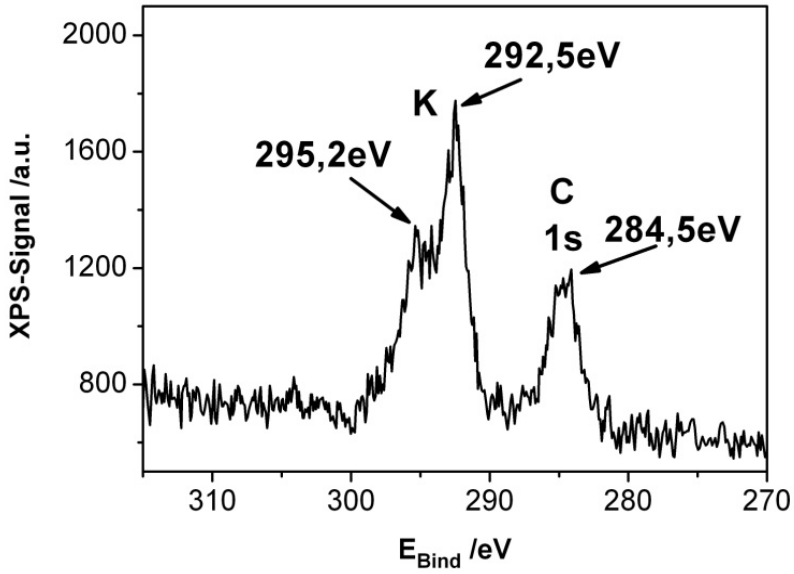

Fig. 5.4: Detail scan of **Fig. 5.3** to enlarge the C1s peak.

5.3 p6P on freshly cleaved mica (001) – monolayer regime

By using TDS it was possible to investigate the ultra thin p6P films in the sub monolayer regime. In **Fig. 5.5** one can see a TDS series of p6P films on mica (001) with different film thickness. Due to the high ionization energy of the QMS the QMS-signal intensity of the cracking products is usually higher than the QMS-signal of the original mass of p6P and among all the cracking products of p6P the mass 61 yielded the highest signal and therefore the best signal to noise ratio. Therefore in the monolayer regime, where the QMS signals are very small, the signal of the mass 61 is shown to represent the desorption of the p6P molecules. The amount of deposited molecules is denoted by means of the nominal mean film thickness, as measured by the quartz microbalance.

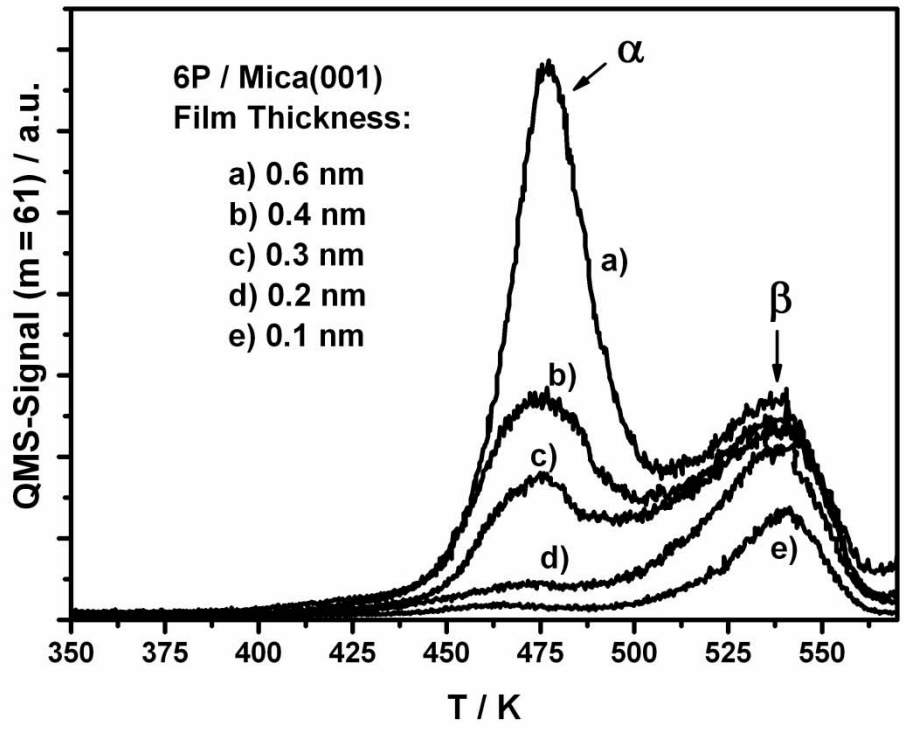

Fig. 5.5: TDS series of p6P grown on clean mica (001) at $T_{ads} = 300\ K$. The monolayer and multilayer desorption peaks are denoted by β and α, respectively. The total amount of deposited p6P for each single TD-spectrum is represented as the mean film thickness in nm .

Starting at a nominal mean film thickness of $0.1\ nm$, a peak which is labelled β arises at approximately $535\ K$. This peak keeps increasing with increasing p6P deposition until at a

film thickness of about $0.2\ nm$ a saturation of the β peak can be observed and another peak arises around $475\ K$, which is labelled α. This α peak increases steadily with increasing film thickness while the β peak remains unchanged. Since the β peak reaches saturation at a rather small film thickness ($0.2\ nm$) and from the asymmetric peak shape as well as from the coverage independent peak maximum, one can assign this peak to first order desorption from the monolayer. In previous AFM investigations [61] an indication for the existence of a monolayer was stated. A significantly higher root mean square (RMS) roughness of areas of a p6P-covered sample in between the crystallites or chains compared to the clean mica substrate was observed. Compared to these AFM measurements, the TDS measurements represent a direct proof for the existence of such a continuous monolayer (wetting layer) of p6P molecules on mica (001).

5.4 p6P on freshly cleaved mica (001) – multilayer regime

Thicker p6P films were investigated by TDS, XPS, SEM and AFM. A TDS series starting from $5\ nm$ up to $30\ nm$ is shown in **Fig. 5.6**.

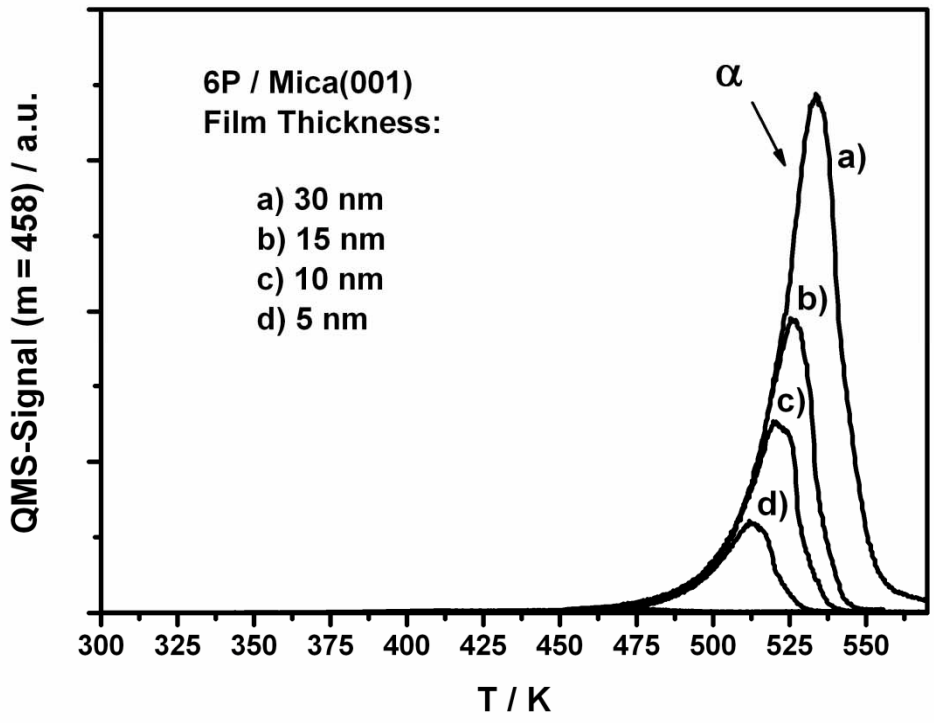

Fig. 5.6: TDS series of p6P grown on mica (001) at $T_{ads} = 300\ K$ in the multilayer regime. The total amount of deposited p6P for each single TD-spectrum is given as the mean film thickness in nm.

In the case of multilayer desorption the signal of the intact molecule (mass 458) is shown because there the QMS-signal is sufficiently high to yield a satisfying signal to noise ratio. In this spectrum the monolayer peak is not visible due to its much smaller intensity. From the asymmetric shape of the α peak, the fact that the peak shifts to higher temperatures with the coverage and the common leading edge of the peaks one can assign these peaks to zero order desorption from the multilayer. However, the peak shape in this case resembles much less a zero order desorption behavior than that for p6P desorption from metal surfaces, e.g. for Au (111) [20, 21, 71]. The reason for this is most probably the non uniform temperature distribution on the front surface of the mica sample due to its poor thermal conductivity. The multilayer desorption peaks in this case should rather be seen as the superposition of a number of desorption peaks with zero order desorption behavior, each of them slightly shifted in temperature with respect to each other.

For all the different films of **Fig. 5.6** AFM measurements were carried out (**Fig. 5.7**). The obtained AFM images were similar to the ones published in the literature previously [23-29].

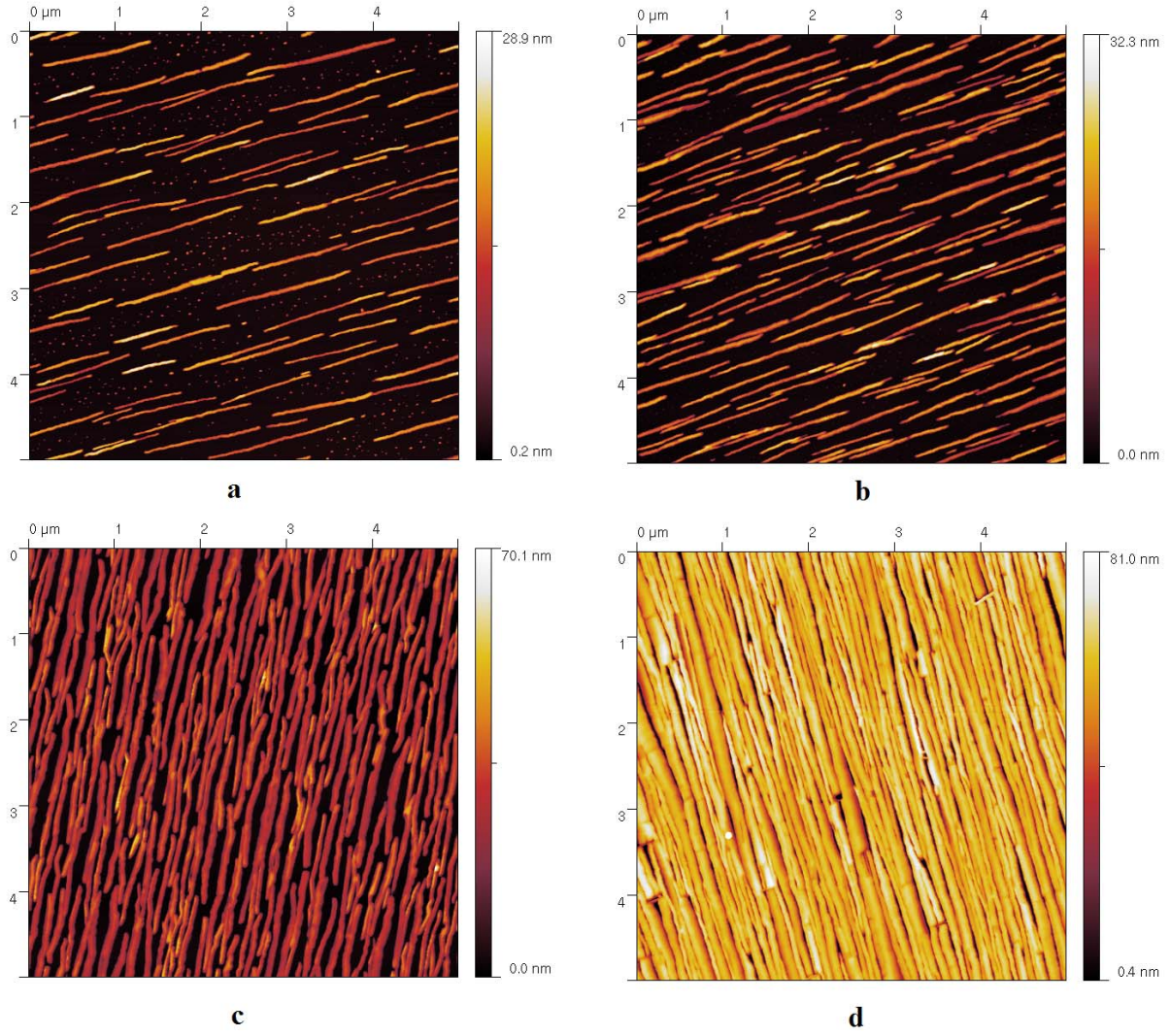

Fig. 5.7: AFM images of different p6P films on freshly cleaved mica. Lateral resolution of all images was $5\mu m \times 5\mu m$. Films were grown at room temperature. Thickness of the films: **a)** $1\ nm$, **b)** $2\ nm$, **c)** $7\ nm$, **d)** $30\ nm$.

At initial growth stages, characteristic needle-like islands (nano-fibers) and crystallites coexist on the mica surface. Within the needles the molecules are oriented with their long axis parallel to the surface and nearly normal with respect to the needle direction (see **Fig. 5.8**).

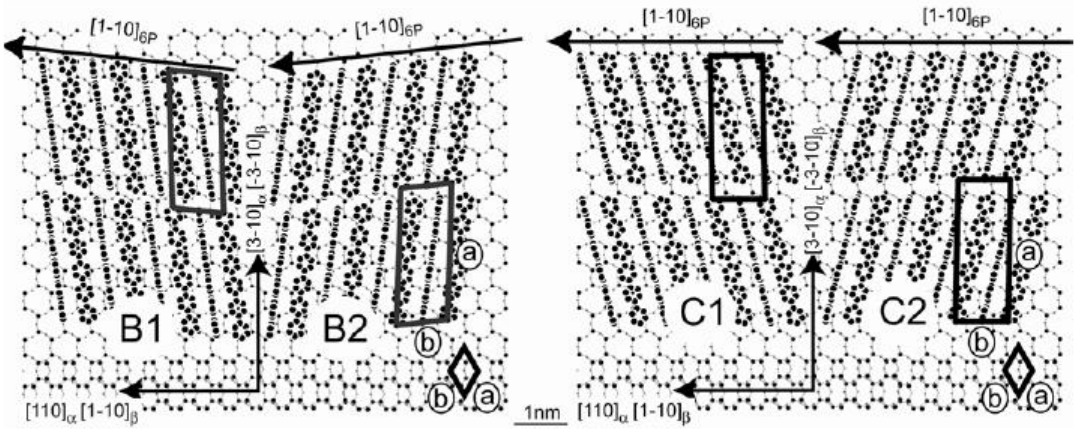

Fig. 5.8: Alignment of the hexaphenyl molecules relative to the mica (001) surface for different epitaxially aligned hexaphenyl crystallites. The two possible mica (001) cleavage planes α and β are accounted by respective lattice directions on the substrate surface. The thick arrows on top give the different directions of the needle shaped hexaphenyl crystallites. These arrows run approximately along high symmetry directions of the mica (001) surface, namely $[110]_{mica}$ in the case of $\alpha(001)_{mica}$ and $[1\text{-}10]_{mica}$ in the case of $\beta(001)_{mica}$. Relative to this high symmetry substrate direction, the arrows are rotated by 6° in case of B1 and B2 while the arrows are exactly parallel for C1 and C2. The unit cells of the two-dimensional surface lattices of the substrate as well as for the hexaphenyl crystals are drawn by full thick lines. From [128].

The nano-fibers are highly oriented over large surface domains and grow epitaxially on the substrate surface by two different crystal orientations with the crystallographic {11-1} (point on line coincidence I, orientation B) and the {11-2} (coincidence, orientation C) planes parallel to mica (001) [128]. Each crystal orientation shows two crystal alignments that are mirrored to each other denoted as B1, B2 and C1, C2, respectively.

As shown in **Fig. 5.8** and also in the AFM images **Fig. 5.7a** and **Fig. 5.7b**, the grown needles are sometimes not fully parallel, which is directly related to the differently aligned hexaphenyl crystals. The reason for this more or less parallel orientation of the needles is the existence of surface dipole fields on the mica surface, which are caused by the positive charge on the surface due to K^+ ions and the negative net charge in the subsurface layer due to the Al^{3+} ions substituting for Si^{4+} ions [24]. With increasing film thickness, the needles grow larger and higher by regrouping the crystallites. It is proposed that the driving force for the regrouping of the crystallites is the strain that is induced locally by the crystallites into the wetting layer [61]. The rearrangement process is performed by the crystallites as entities.

Once the crystallites are incorporated into the chain they are trapped there. Besides the film thickness, the substrate temperature also plays an important role in layer growth. **Fig. 5.9** shows the morphology of $7\,nm$ films of p6P on mica (001) grown at different substrate surface temperatures, namely $110\,K$, $330\,K$ and $400\,K$, measured with SEM (**Fig. 5.8a**) and AFM (**Fig. 5.8b**). Cross sections as obtained by AFM are shown in **Fig. 5.9c**.

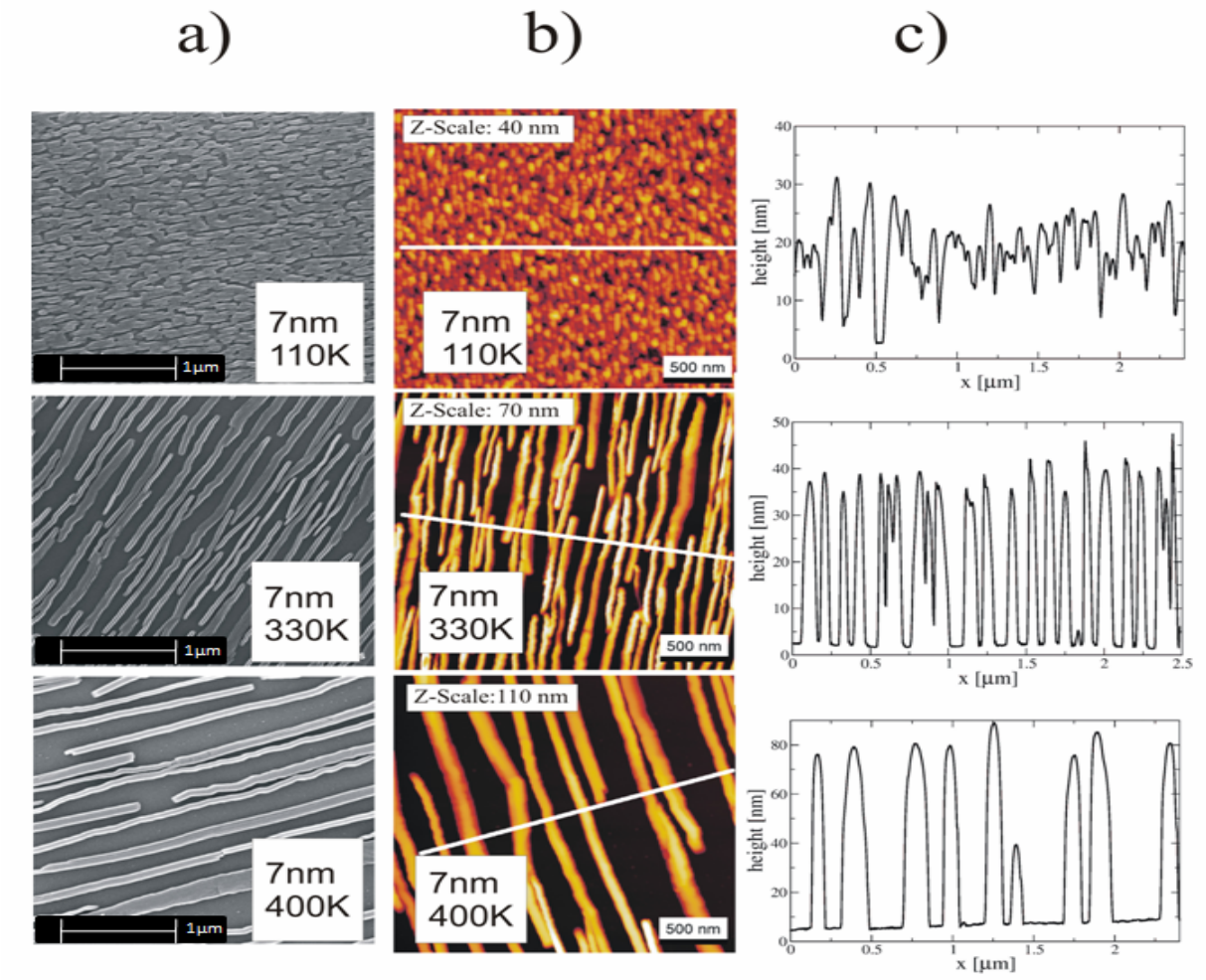

Fig. 5.9: SEM **(a)** and AFM **(b)** images of $7\,nm$ thick films of p6P on mica (001) grown at different adsorption temperatures, $110\,K, 330\,K, 400\,K$ and cross sections of the AFM images **(c)**. Please note the different Z-scales for the AFM images and the cross sections.

At low temperatures, the film consists only of small crystallites (about $100\,nm - 200\,nm$), which cover almost the whole surface. An increase of the substrate temperature during adsorption leads to the formation of needle-like structures (about $100\,nm$ - several μm in length). A further increase of the temperature leads to an increase of needle height and width, resulting in a decrease of needle density. In order to inspect the rearrangement of the crystallites during sample heating 'XPS vs. temperature' measurements have been performed.

The height of the C1s signal of the p6P film gives information on how much of the surface area is covered with the film. This way it is possible to find out if the p6P film is arranged in small crystallites which almost cover the whole surface or in large and high needle-like islands which cover less surface area at the same mean coverage. Various XPS vs temperature spectra are depicted in **Fig. 5.10** with the film formation temperature as a parameter.

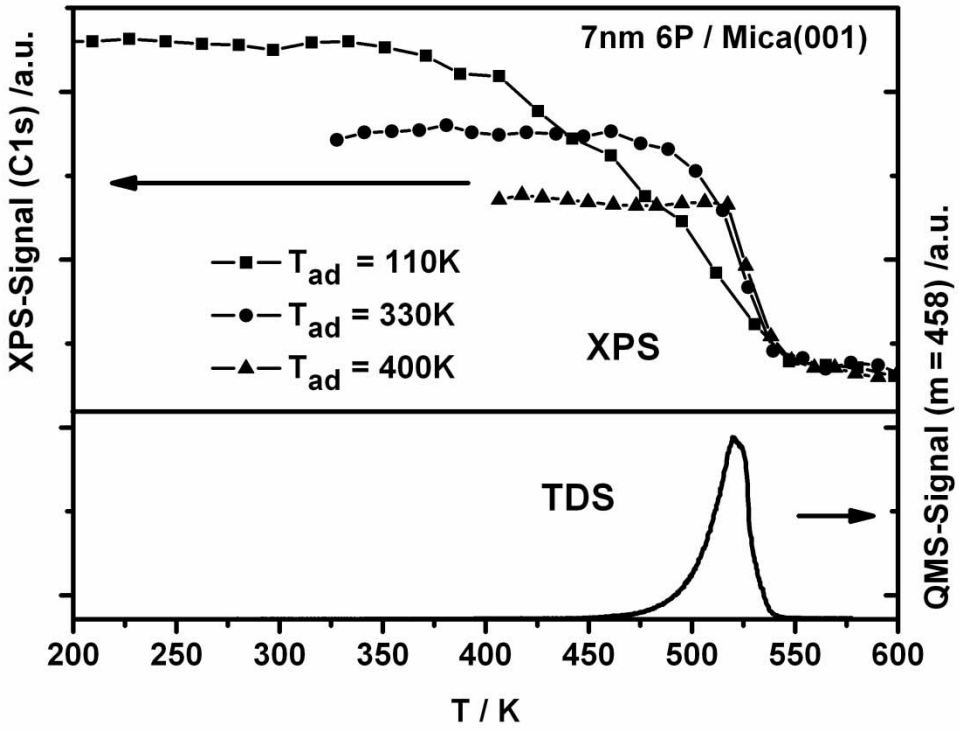

Fig. 5.10: Top: Change of the C1s signal for $7\ nm$ thick p6P films grown on mica (001) at different substrate temperatures ($110\ K, 330\ K, 400\ K$), as a function of the temperature during heating the sample with $1\frac{K}{s}$. **Bottom:** Representative thermal desorption spectrum for a $7\ nm$ thick p6P film on mica (001) at a heating rate of $1\frac{K}{s}$.

In the upper part of **Fig. 5.10** one can see the C1s XPS signal heights (symbols + line). At the bottom a TD-spectrum is depicted for comparison to show where desorption starts. Seven nanometer thick p6P films were prepared at different adsorption temperatures and then heated by $1\frac{K}{s}$. One can see that the height of the XPS peaks strongly depends on the film formation temperature. The higher the adsorption temperature, the lower is the signal. This is consistent with the AFM observation that at lower temperatures ($110\ K$) the film consists of small

crystallites while at higher temperatures ($330\ K, 400\ K$) it consists of larger and higher needle-like islands which do not cover as much substrate surface area as the small crystallites. Utilizing this technique, not only the surface morphology at a certain preparation temperature can be characterized, but also the crystallite rearrangement process during heating. The films prepared at $330\ K$ and $400\ K$ do not change in the morphology (as seen by the constant XPS signal) until desorption starts. The XPS signal decrease coincides directly with the TD-spectrum. Observing the $110\ K$ film C1s signal, however, one can see a decrease of the carbon signal already before desorption actually starts. This indicates a rearrangement of the crystallites, forming larger needles which keep getting higher with increasing temperature, uncovering larger areas of the mica substrate. The results of these low temperature experiments are interesting for two reasons: First of all it shows that the film morphology can considerably be changed by the low preparation temperature. Second, the constant XPS signal between $110\ K$ and $350\ K$ shows that the film morphology does not change during warming up to room temperature. This means that films prepared at these low temperatures can be investigated at room temperature by ex-situ techniques, for instance SEM and AFM, as it was done in this work.

5.5 p6P on carbon contaminated mica (001)

As shown in **Fig. 5.3**, air-cleaved mica contains carbon. The amount of the carbon contamination may depend on the time it takes to get the mica into (ultra) high vacuum conditions after the cleavage. In order to obtain information on the influence of carbon on the film growth, the amount of carbon was intentionally increased. Unlike on Au surfaces [21, 71] there was no dissociation of hexaphenyl on mica during heating, which made it necessary to induce p6P dissociation by other means. Eventually, the carbon coverage was prepared by X-ray induced dissociation of p6P. For this purpose a rather thick film ($> 10\ nm$) was grown at low temperatures (around $100\ K$) and then exposed to the Mg Kα radiation of the X-ray gun for about 2 h. The X-ray irradiation led to the dissociation of a certain amount of the p6P molecules and carbon accumulated on the surface. After a subsequent TD-flash, which was necessary to get rid of the residual p6P and its cracking products, only carbon remained on the surface.

That way four different carbon coverages were prepared and the amount of carbon was determined by XPS, as can be seen in **Fig. 5.11**. The amount of carbon could be increased up to a certain saturation coverage, which is used as a reference in this figure. All the C coverages are given in a fraction of the saturation coverage $\theta_{sat} - 1$.

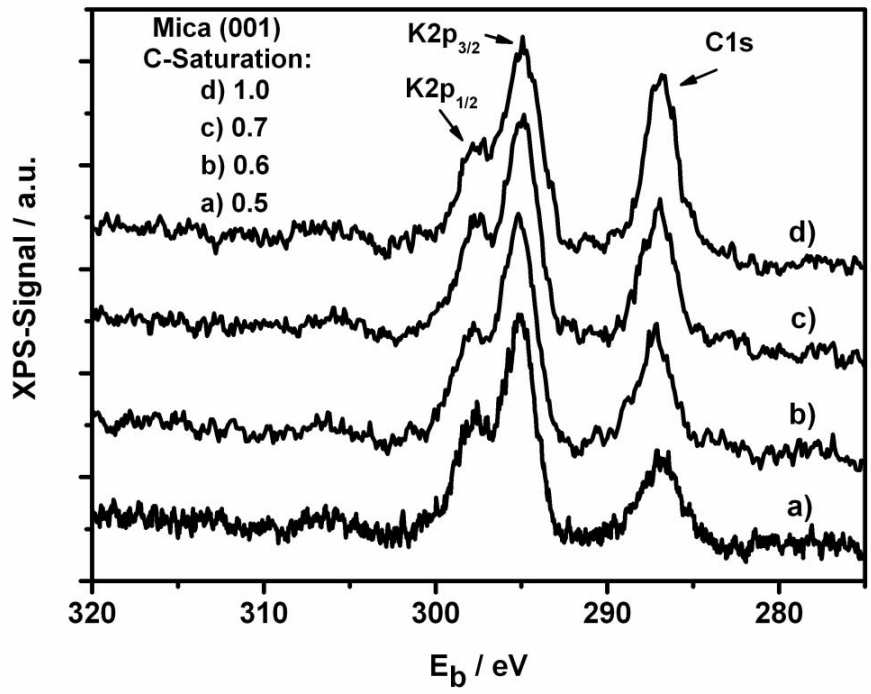

Fig. 5.11: XPS spectra of mica with different carbon coverages. C-coverage in units of the carbon saturation layer. **(a)** Air-cleaved mica, **(b)**–**(d)** After dissociation of p6P.

The increase of the carbon coverage as a result of the p6P dissociation can be followed by XPS, as seen in **Fig. 5.11**, **b–d**. This additional carbon influences the TDS behavior of p6P significantly. The associated TD-spectra are shown in **Fig. 5.12**. In order to compare the spectra of different carbon coverages with each other, the film thickness ($0.35\ nm$) and adsorption temperature ($300\ K$) were held constant.

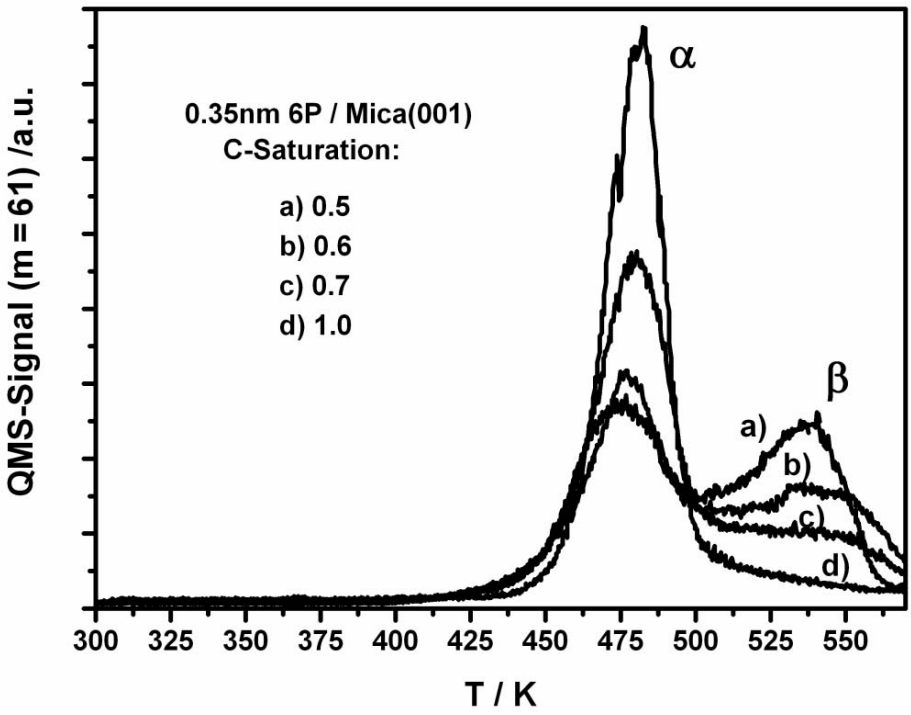

Fig. 5.12: TDS series of $0.35\ nm$ p6P grown on partially C-covered mica (001) surfaces at $300\ K$. The monolayer and multilayer desorption peaks are denoted by β and α, respectively. C-coverage is given in units of the carbon saturation layer, in accordance with the XPS spectra in **Fig. 5.11**.

The TD-spectrum obtained from the freshly cleaved mica surface (labeled **a)**), shows two peaks, β and α, for the monolayer and the beginning multilayer. As mentioned before, the existence of this β peak is a direct proof of a continuous monolayer of p6P on the mica (001) surface, thus of the existence of a wetting layer. With increasing C-coverage (curves **b**–**d**) one observes a decrease of the monolayer (β) peak until at the saturation coverage the β peak is completely missing. This indicates a significant change in initial film growth, i.e. in the monolayer regime. From these TD-spectra it follows that the p6P multilayer no longer grows on mica covered with a p6P wetting layer (*Stranski–Krastanov* growth), but on the mica surface itself (*Volmer-Weber* growth).

Another direct proof of a change in film growth of p6P on carbon contaminated surfaces could be obtained from AFM measurements. In **Fig. 5.13** a $1\ nm$ thick film of p6P on a C-saturated mica surface is shown.

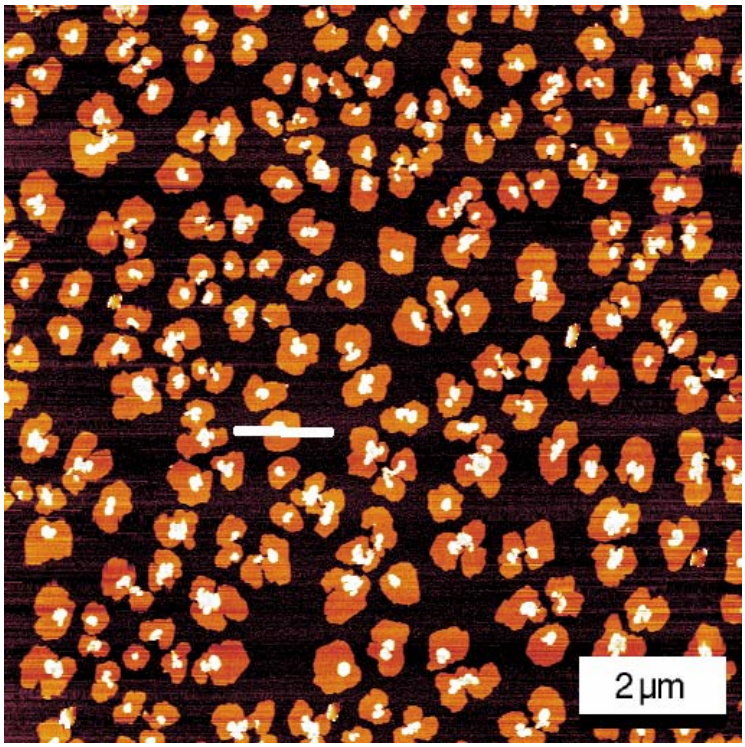

Fig. 5.13: AFM image of a $1\ nm$ thick p6P film grown on carbon covered mica (001) surface at $330\ K$. Z-scale: $5\ nm$.

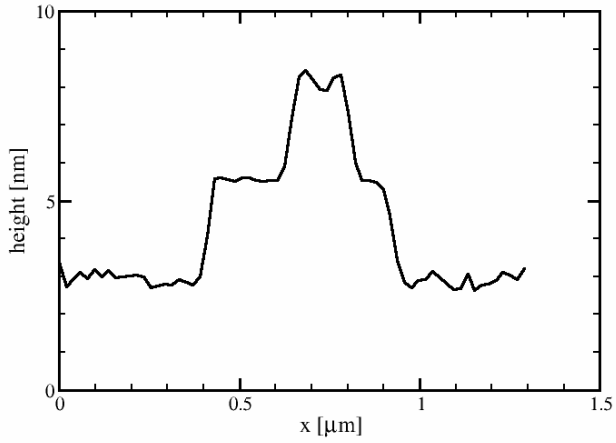

Fig. 5.14: Cross section analysis of the same film along the white line shown in **Fig. 5.13**.

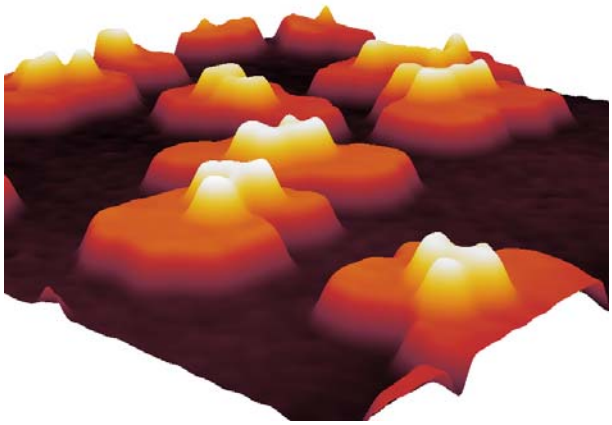

Fig. 5.15: 3D AFM image of the same film as shown in **Fig. 5.13** ($1\ nm$ p6P on C-mica at $330\ K$).

A cross-section of **Fig. 5.13**, as depicted in **Fig. 5.14**, shows that the height of such islands is roughly $2.7\ nm$, which corresponds to the length of a p6P molecule. This is an evidence that on the C-covered mica surface the monolayer does not consist of molecules lying flat on the surface but of molecules standing upright and that additional material forms a second layer of molecules standing upright on this first layer. **Fig. 5.15** shows a 3D-view of the same film. A similar film growth (p6P molecules standing upright) has already been reported for p6P films on mica surfaces, which were exposed to ambient conditions for two weeks after cleavage [39], p6P films on mica treated with water or methanol [29], on gold covered mica [125], as well as on carbon covered gold surfaces [21].

5.6 p6P on sputtered mica

In the previous sections the vast influence of carbon on the film growth was demonstrated. The next step was to try to get rid of the carbon on the freshly cleaved mica specimen, which was expected to lead to some change in the film morphology and wetting layer behavior. First attempts to eliminate the carbon by simple degassing under UHV conditions or by heating under oxygen atmosphere were not successful. Therefore a cleaning procedure was tried, which has proven to be successful for many other substrates, to wit sputtering. The effect of sputtering depends strongly on the used beam voltage and on the sputtering dose. If high beam voltages are used and long sputter times ($> 30\ \mathrm{min}$), it is possible to get a carbon-

free surface, i.e. no carbon peak in the XPS. The drawback of using these parameters is that the surface contains a lot of holes and humps after this kind of brute treatment (**Fig. 5.16**)

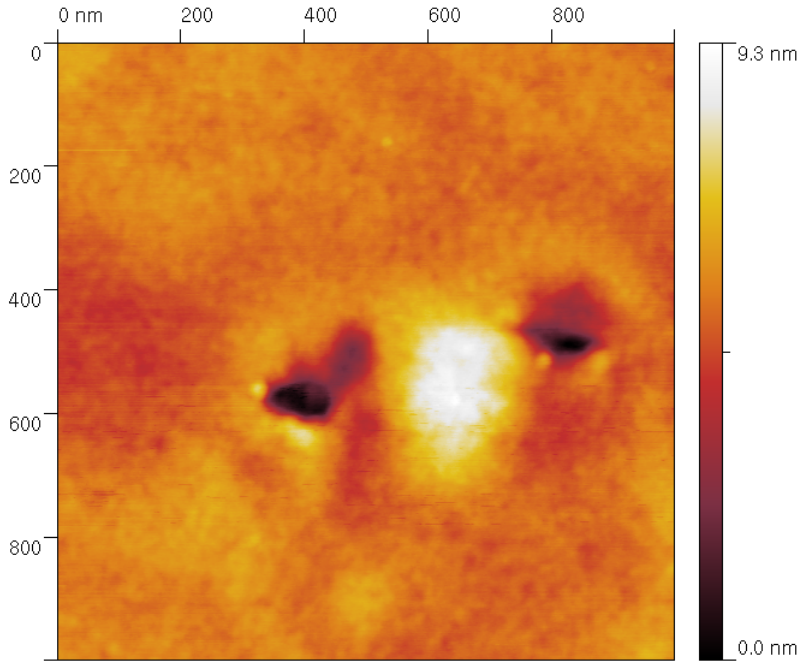

Fig. 5.16: The mica surface after sputtering with a beam voltage of $1.5\ kV$ for 30 minutes, Ar-pressure $5 \times 10^{-5}\ torr$.

So as to prohibit morphological damage of the mica samples during sputtering, a lower beam voltage ($500\ V$) was used. This 'gentle sputtering' though did not affect the chemical composition of the mica specimen, i.e. the XPS spectra remained unchanged. However, the LEED pattern continually deteriorated with the sputtering time until after some minutes of sputtering no LEED pattern could be observed anymore, which indicated a destruction of the ordered surface structure.

These structural changes of the mica surface influence the p6P film growth significantly, as can be seen in the TDS, which is depicted in **Fig. 5.17**. In this figure several TD-spectra are compiled, which were recorded after different sputtering times. In all the spectra, the adsorption temperature was $300\ K$ and the film thickness was $0.4\ nm$.

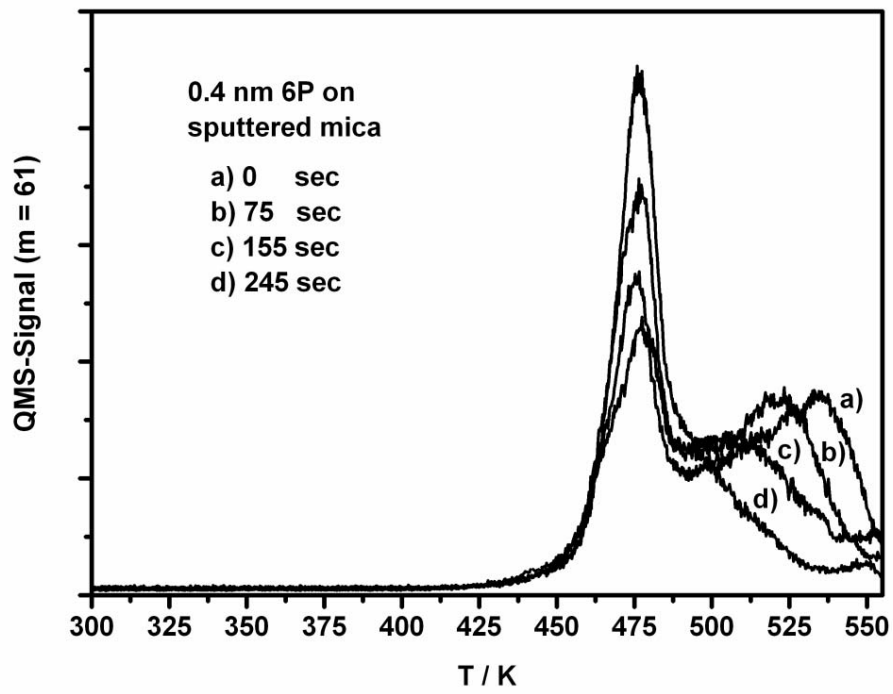

Fig. 5.17: TDS series of $0.4\ nm$ p6P grown on sputtered mica (001) surfaces at RT. The monolayer and multilayer desorption peaks are denoted by β and α, respectively. The sputtering time is denoted in seconds.

As already described in Section **5.2**, on the untreated mica surface two peaks can be seen, which are labeled α and β. The α peak corresponds to the initial multilayer, the β peak to the monolayer. In **Fig. 5.17** one can see a decrease of the β peak with increasing sputtering time, which on the other hand leads to an increase of the α peak. The total area of the individual desorption spectra remains constant within the experimental error. This means that, like on the carbon covered mica surface (**Fig. 5.12**), a significant change of the film growth in the monolayer regime takes place as a result of disordering the surface structure. However, there are some differences between the TDS series on the carbon covered mica surface and the TDS series on the sputtered mica surface. In **Fig. 5.12**, the β peak decreases in height with increasing carbon coverage and the peak maximum remains nearly constant. By contrast, in **Fig. 5.17** in addition to the decrease of the β peaks, also a shift to lower temperatures can be observed. A possible explanation for this different behavior is as follows: In the case of carbon contamination by p6P dissociation, most probably islands of higher carbon density will develop, where no monolayer can exist. Therefore the decreased β state results from the decreased area of the untreated surface. On the other hand, sputtering will yield a uniform

disordering of the whole surface. With increasing surface disorder, the binding strength of the molecules in the monolayer will decrease.

The p6P film growth on the sputtered mica surface was also investigated by AFM. In **Fig. 5.18** the morphology of a $1\ nm$ thick p6P film grown at room temperature on a surface after a sputtering time of 245 seconds (equivalent to curve **d)** in **Fig. 5.17**) is shown. A cross section of this film is displayed in **Fig. 5.19** and a 3D-view in **Fig. 5.20**.

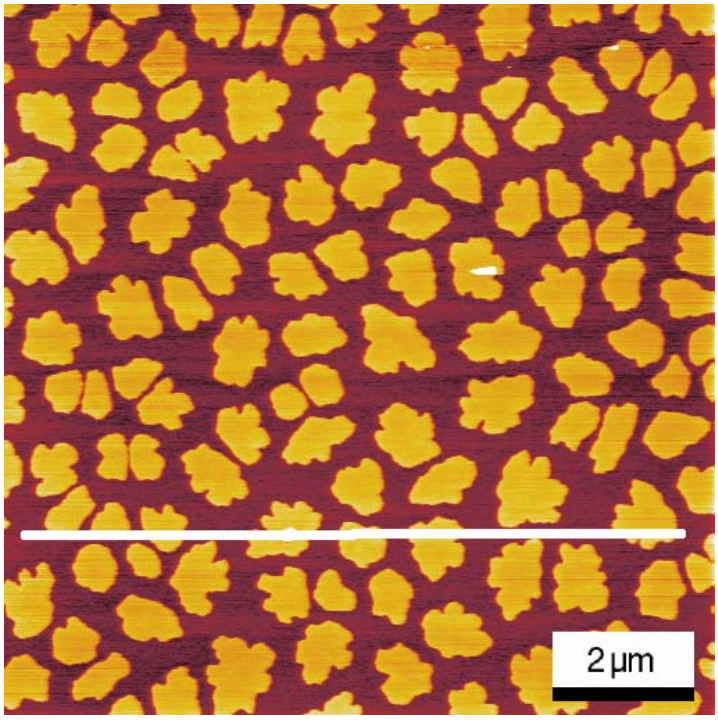

Fig. 5.18: AFM image of a $1\ nm$ thick p6P film grown on a sputtered mica (001) surface (sputtering time: $245\ s$) at room temperature.

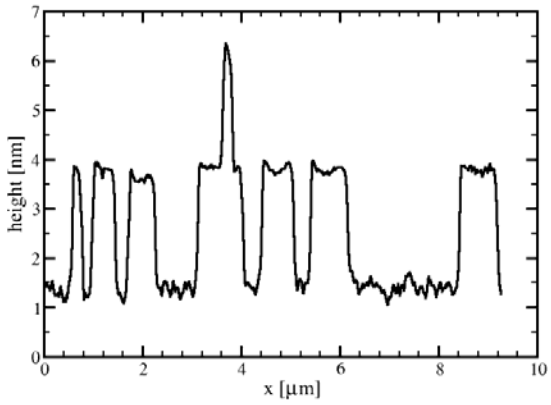

Fig. 5.19: Section analysis along the white line in **Fig. 5.18**.

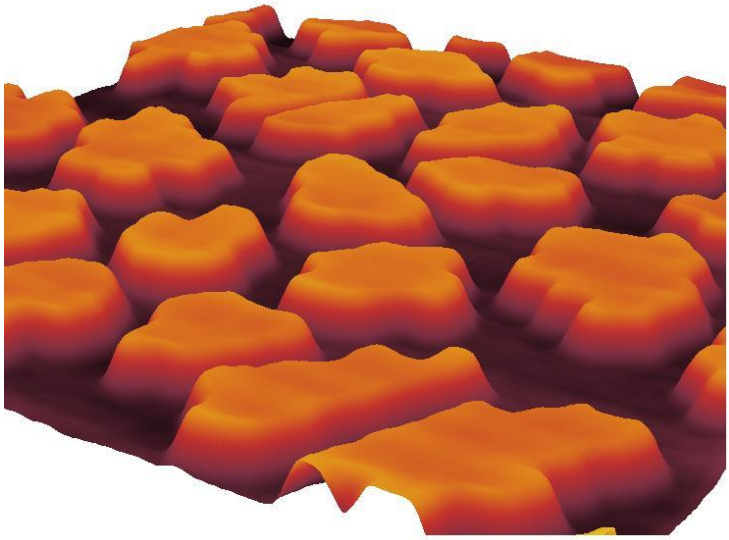

Fig. 5.20: 3D AFM image of the film shown in **Fig. 5.18** ($1\ nm$ p6P on sputtered mica at $300\ K$).

One can see that like on the carbon covered surface, the monolayer consists of islands of molecules standing upright (island height approximately $2.5\ nm$). However, the density of the islands is higher, maybe due to a different step-edge barrier, and therefore nearly no second layer can be observed in this figure.

5.6.1 Step-edge barrier in organic film growth

A characterization of the step-edge barrier (Ehrlich-Schwoebel-Barrier) could be carried out [65] by using an atomistic nucleation theory (see section **2.3 Nucleation on islands: Step-edge barriers)** that is established in inorganic film growth [86]. For that purpose several films of different film thickness from $1\ nm$ up to $100\ nm$ were prepared. With increasing film thickness (**Fig. 5.21**, **Fig. 5.22**) stepped mounds with a step height of $2.5-2.7\ nm$ are formed on top of which small elongated crystallites arise that do not exhibit the terrace structure and most probably consist of lying molecules, since they resemble the well-known p6P needles observed on freshly cleaved mica or KCl. The single mounds are separated by deep crevices that do not close with ongoing deposition (sometimes referred to as 'Zeno effect' in the literature [129]).

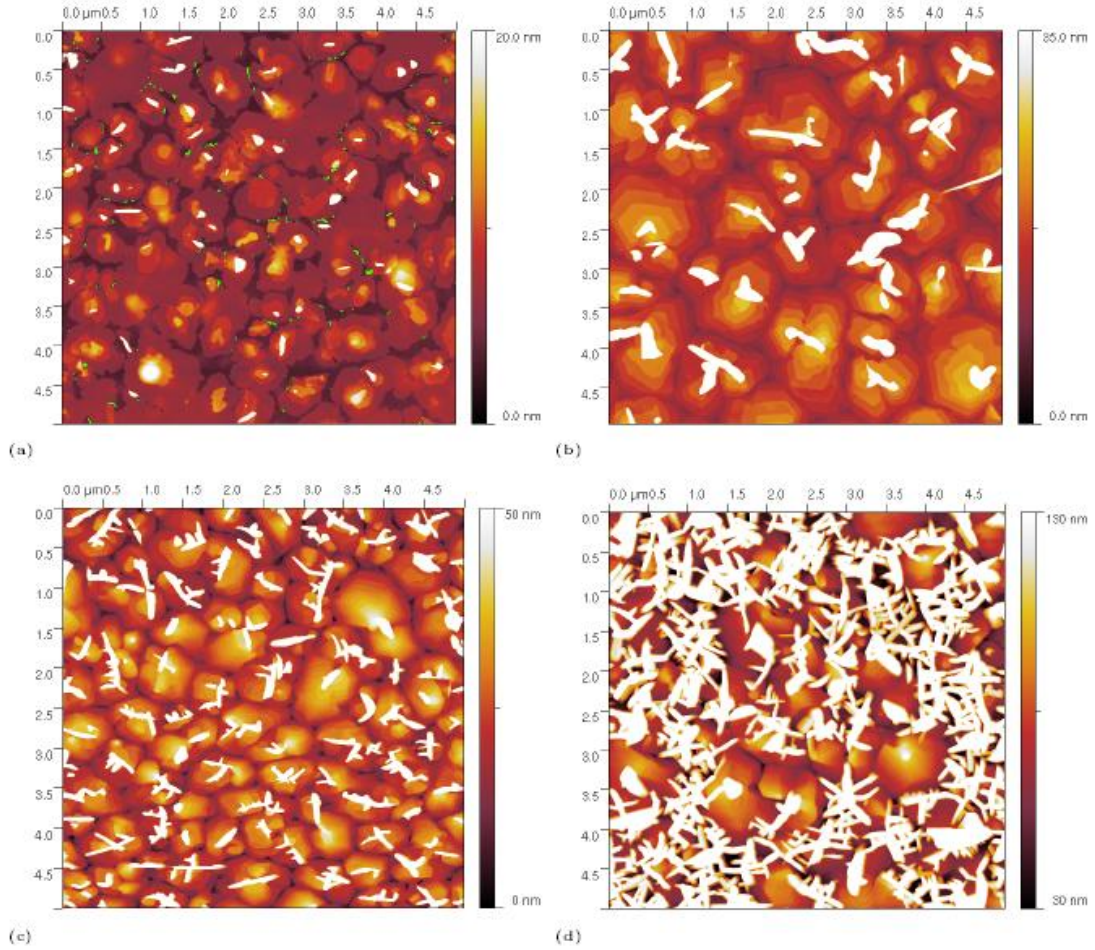

Fig. 5.21: Series of AFM images showing the evolution of the film morphology with increasing film thickness. All films were grown at RT on ion bombarded mica (001). **(a)** $4\ nm$, **(b)** $10\ nm$, **(c)** $30\ nm$, and **(d)** $100\ nm$ film thickness [65, 77].

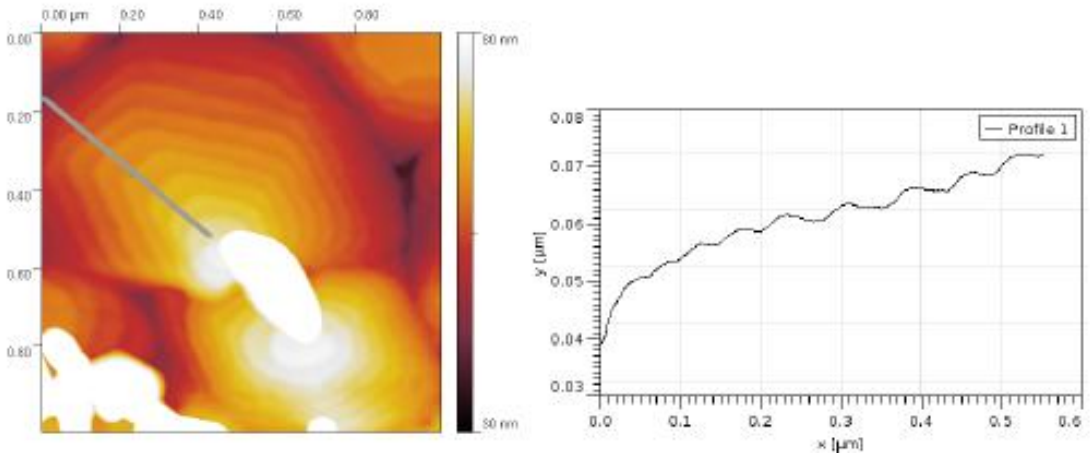

Fig. 5.22: Left: A typical mound in a $30\ nm$ thick p6P film. A small needle is seen on top of the mound. **Right:** Cross section along the line in the image on the left. One can see the characteristic lateral shape of the mound, characterized by a deep trench separating it from the neighboring mounds.

The mounds have a clear tendency to a polygonal shape, as can be seen in **Fig. 5.22**. The surface fraction covered by the needle-like structures increases with increasing film thickness. It is supposed [77] that these p6P needles form on ordered substrates and that the terraces on top of the mounds exhibit an order sufficiently high to allow the needle formation. For the evaluation of the mounds the needles on top of the mounds had to be removed by applying a height thresholding algorithm to the AFM images, which is in detail explained in ref. [77]. Using eq. 2.2 - eq. 2.4 with $D = 2$ (two-dimensional diffusion process) and $i^* = 1$ (critical nucleus size) together with the experimentally obtained values of $\lambda = 1\ \mu m$ (mound separation) and $l \approx 20 - 60\ nm$ (top terrace diameter) one ends up with a value of $0.67 \pm 0.04\ eV$ for the step-edge barrier. The error of this value stems mainly from the uncertainty of the parameter l, which is hard to measure due to the needle-like structures on top of the mounds. The value for the step-edge barrier was corroborated by molecular dynamics simulations [65], too. However, it turned out that several interesting features arise for the large organic molecules (compared to the classical inorganic picture where just single atoms are the diffusing species) which have to be taken into account for the simulations. First, the calculations revealed that the diffusion of the rod-like p6P molecule is favored along its long molecular axis. As a consequence, the molecules will arrive at the step-edge with their long axis perpendicular to it and if they overcome the barrier, they will be in the correct orientation to be incorporated into the underlying layer. Another important feature of large molecules comes into play during the diffusion process over the edge, where the molecule is either sticking out over the terrace (if it is rigid) or strongly bent. In case of rigid molecules, nearly all the intermolecular bonds have to break at the same time if the molecule overcomes the barrier, which leads to a relatively high step-edge barrier. According to this, a bending of the molecule is more favorable if the bending itself is not too energy-consuming. Indeed, there is experimental proof that the p6P molecule exhibits a rotational flexibility along the inter-ring C-C bonds [130]. This was shown for p6P adsorption on a Ni (110)(2x1)-O surface, where a bending of the phenyl rings of a single molecule with respect to each other was observed in STM images. The calculations yielded a step-edge barrier of $0.90\ eV$ for the rigid molecule and $0.61\ eV$ for the bending molecule, whereas more than 70% of the latter value is due to the energy cost related to the bending of the molecule.

Eventually, an evaluation of the first undermost terraces in the AFM images yielded another significant deviation from the inorganic growth model. It turned out that the tilt angle of the molecules is not constant in each layer. The first few layers of terraces are influenced by the substrate and exhibit a higher tilt angle from the surface normal, which decreases with increasing distance to the mica surface (illustrated in **Fig. 5.23**). In the bulk the tilt angle is 17° from the surface normal, which is exactly the value also obtained for the bulk terraces on KCl (see **Fig. 6.8**). The energy that is needed for the bending of a molecule decreases with the decreasing tilt angle of the underlying terrace. Thus the contribution of the energy cost for the bending to the step-edge barrier varies from layer to layer, resulting in different step-edge barriers. The step-edge barrier for the first layer was calculated utilizing another independent method which was applied to the $1\,mm$ thick film [65]: The number fraction of first layer islands with a certain size that have nucleated a second layer island on top yields the critical island size, which in turn gives the interlayer jump rate that is used to calculate the step-edge barrier (eq. 2.2). That way a value of $0.26\,eV$ for the step-edge barrier in the first monolayer was obtained.

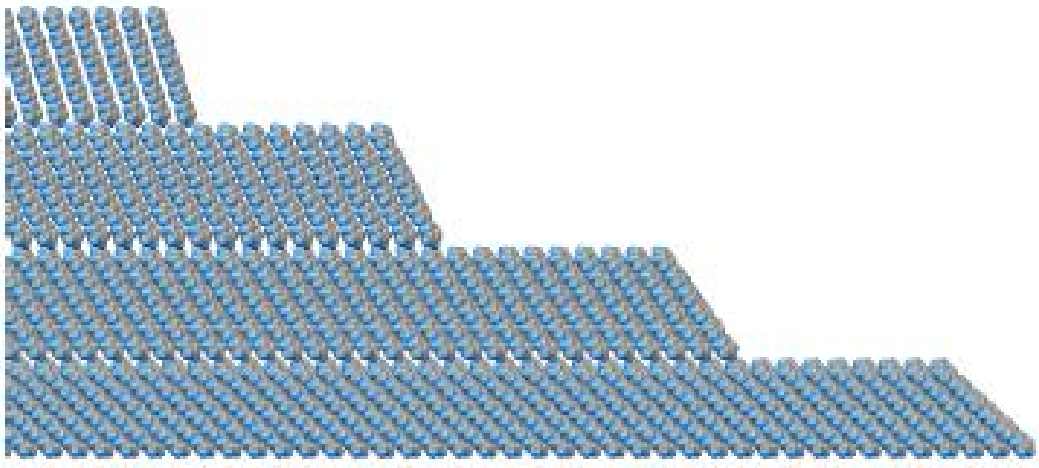

Fig. 5.23: Schematic view of the varying tilt angles in the first few layers. The step-edge barrier decreases with increasing tilt angle.

6 Hexaphenyl on KCl (001)

This chapter overviews the growth of p6P on KCl (001). Particular attention was drawn to the thermal stability of the films and to the temperature dependence of the p6P morphology. In contrast to mica, KCl exhibits a moderate thermal conductivity, which allowed a rational calculation of thermal desorption parameters. Again, TDS was used to get information on the existence of a wetting layer and combined TDS vs XPS measurements enabled monitoring the thermal stability of the grown films in-situ. AFM was used to characterize the morphology ex-situ.

After the installation of the KCl (001) substrate into the UHV chamber, small amounts of carbon and oxygen were detected on the surface by XPS. However, after annealing of the sample for 30 minutes at $420\ K$, no oxygen could be detected on the surface anymore. In **Fig. 6.1** the XPS spectrum of KCl right after installation is shown, in **Fig. 6.2** after annealing.

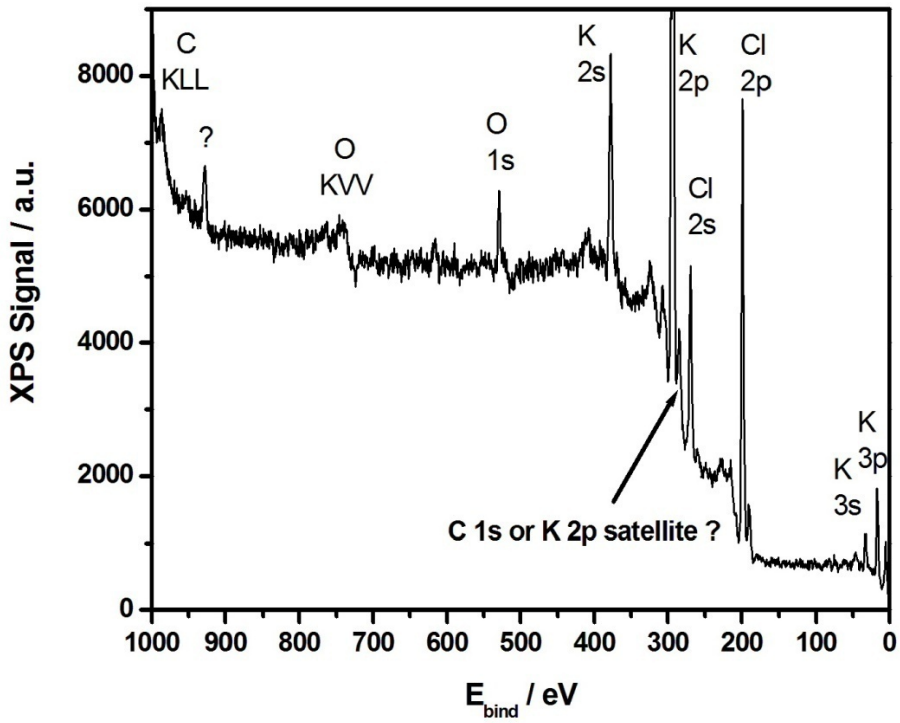

Fig: 6.1: XPS spectrum taken directly after installation and pump down. The peak at $\approx 930\ eV$ which can be seen in both spectra could not be assigned to an element (ghost). The small peak at

$285\ eV$, which can also be seen in both spectra, is not unambiguous. It could be the C1s peak, but also the Mg $K\alpha_3$ X-ray satellite of the K2p peak (displacement $8.4\ eV$, relative height 8.0 %).

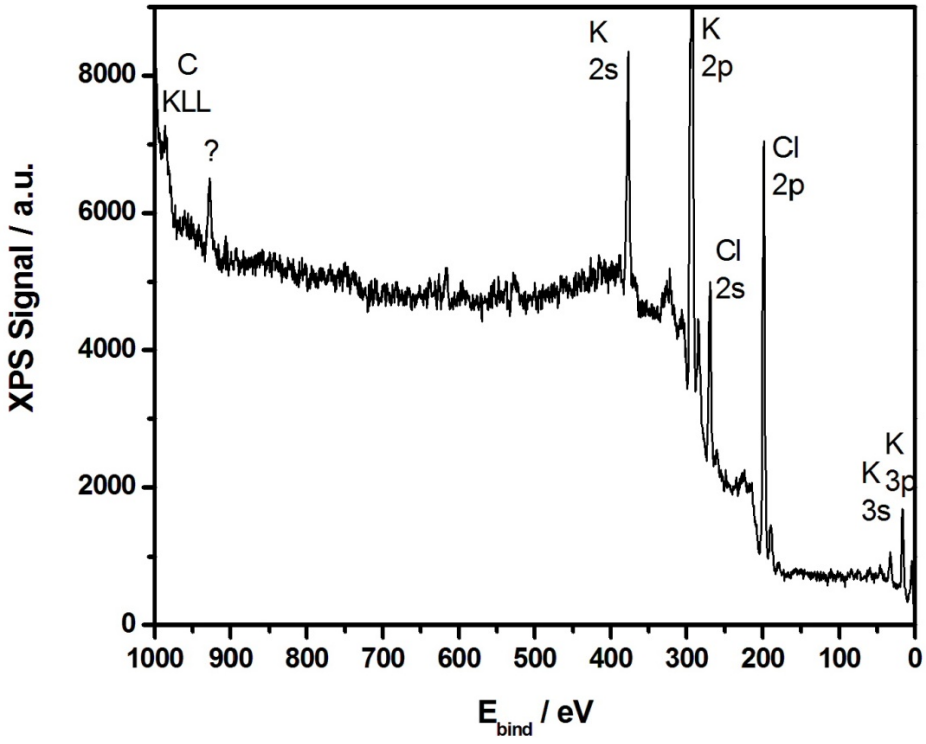

Fig. 6.2: XPS spectrum of KCl after annealing at $420K$ for 30 minutes. It can be seen that the oxygen is removed by annealing. The Auger peak of carbon is very small and almost coincides with the Auger peak of potassium ($\approx 1000\ eV$). Thus it is difficult to ascertain the amount of carbon on the KCl substrate.

The KCl (001) surface is a rather smooth surface which exhibits several steps and flat terraces of atomic height ($\approx 3.15\ Å$, see **Fig. 6.3**)

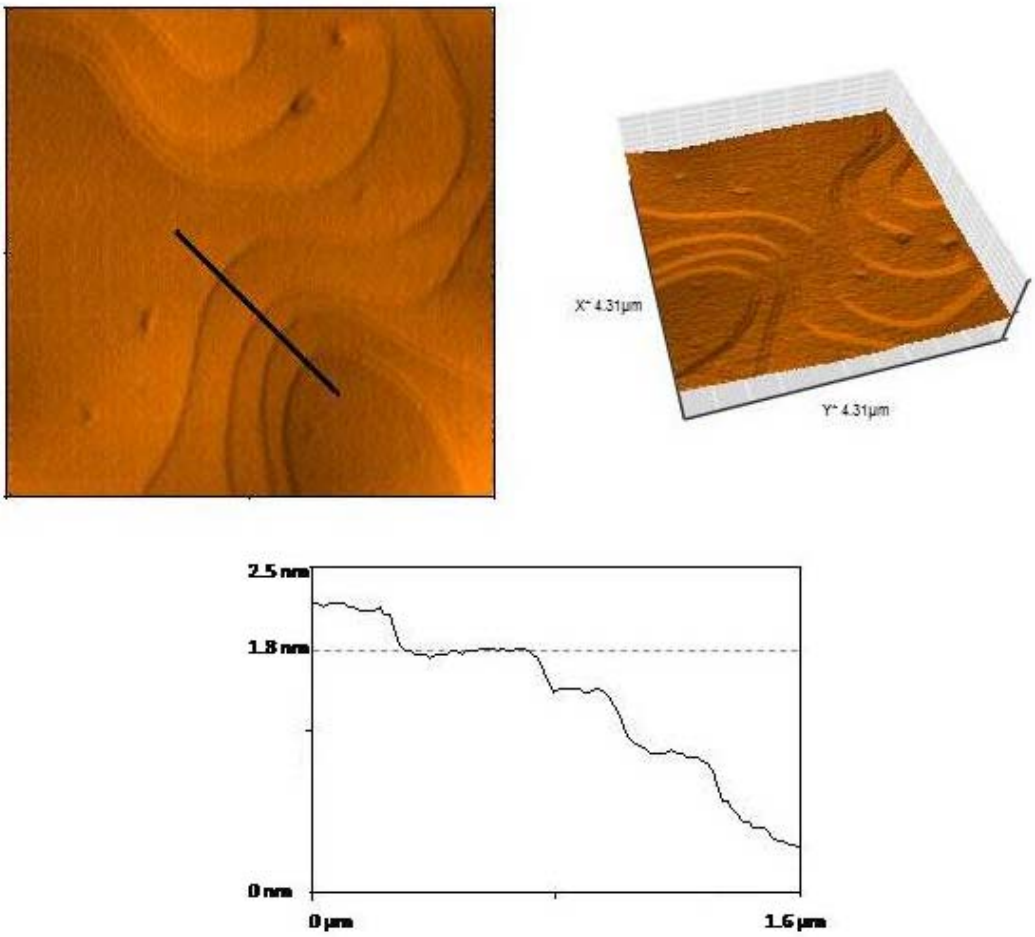

Fig. 6.3: AFM images of the clean KCl (001) surface. **Top left:** $4.3\ \mu m\ x\ 4.3\ \mu m$ image, shaded mode. Z-scale: $6\ nm$. **Top right:** 3-D AFM image of the KCl (001) surface, Z-Scale: $10\ nm$. **Bottom:** Cross-section along the black line. Atomic steps with a height of $\approx\ 3.2\ Å$ (lattice constant of $KCl = 6.3\ Å$) can be seen.

As shown in chapter **5 Hexaphenyl on mica (001)**, the p6P film growth often crucially depends on the formation of a wetting layer. Therefore the first step was to find out whether there existed a wetting layer or not.

6.1 Searching for a p6P wetting layer on KCl(001)

A series of thermal desorption spectra obtained after evaporation of different amounts of p6P on KCl (001) at $400\ K$, ranging from $0.1\ nm$ to $7\ nm$, are shown in **Fig. 6.4**. This adsorption temperature was chosen because it is frequently used in the literature.

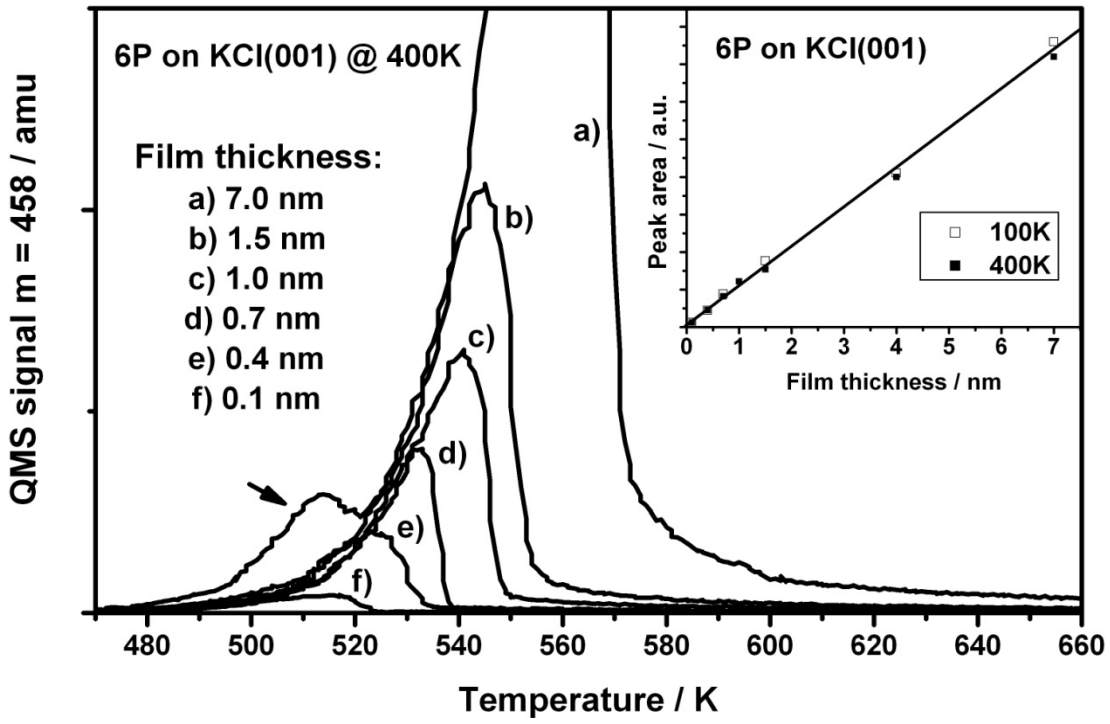

Fig. 6.4: Series of thermal desorption spectra for p6P from KCl (001). Adsorption temperature: $400\ K$, heating rate: $1\frac{K}{s}$. Parameter is the mean film thickness prior to desorption. The arrow points to a peak in curve **a)** which originates from desorption from the Ta clamps (compare with **Fig. 5.1** in section **5.1 Calibration of the TD-spectra**). The inset shows the linear dependence of adsorbed and desorbed p6P for two different adsorption temperatures, $100\ K$ and $400\ K$, respectively.

The asymmetric peak shape, the common leading edge of the spectra and the shift of the peak maxima to higher temperature with increasing coverage are characteristic of a zero order desorption, as expected for multilayer desorption. Similar desorption spectra were also obtained for multilayer desorption of p6P from Au (111) [20, 21, 71] and mica (001) (chapter **5**). However, in these cases additional desorption peaks at higher temperatures were observed at small coverage, which indicated the existence of the more strongly bound wetting layer. In **Fig. 6.4** no evidence for a strongly bound layer can be seen. Even for the smallest coverage of $0.1\ nm$ the peak is located at the common leading edge. The small peak (marked by an

arrow) which appears for the $7\ nm$ TD spectrum is an experimental artefact: It stems from desorption of a $7\ nm$ thick p6P film from the tantalum clamps, which are used to hold the KCl sample to the heating plate (see section **4.3.2 Experimental implementation** for details). It serves as a calibration point for the temperature scale since it can be assumed that the temperature of the metal wires corresponds quite well to that of the steel plate where the temperature is measured. The temperature maximum for the p6P multilayer desorption at the individual coverages is known from the above mentioned literature. From the common leading edge (after proper correction of the temperature scale) one can easily determine the desorption energy E_{des} (heat of evaporation) and also the pre-exponential factor for zero order desorption ν_0 by applying the Polanyi–Wigner equation (eq. 4.6):

$$E_{des} = 2.3\ eV$$

$$\nu_0 = 3 \times 10^{24}\ s^{-1}$$

This is in good agreement with the recently obtained values for p6P on Au (111) [71]. The relatively high value of the pre-exponential factor is typical for the desorption of large molecules [21, 71, 100-104]. However, most important is the fact that down to the smallest coverage of $0.1\ nm$ mean film thickness the p6P molecules show a multilayer desorption behavior, i.e. the molecules desorb from small islands and not from a more strongly bound wetting layer. Quite similar desorption spectra were obtained after p6P adsorption at $100\ K$. This demonstrates that no wetting layer exists, independent of the adsorption temperature.

In the insert of **Fig. 6.4** the correlation between the integral of the TDS peak areas (proportional to the desorbed amount) and the film thickness as obtained from the quartz microbalance is shown. It is a straight line, both for an adsorption temperature of $400\ K$, as

well as of $100\ K$. This shows that the sticking coefficient is independent of the coverage and of the sample temperature in this range. It can therefore safely be assumed that the sticking coefficient is unity at and below $400\ K$. The second important result from this experiment is that all of the adsorbed material desorbs again, i.e. no partial dissociation of the p6P molecules takes place. Such partial dissociation has been observed for p6P and p4P on polycrystalline gold and on stepped gold surfaces [21, 71]. One could argue that a wetting layer very well might exist at the adsorption temperature but that during the temperature increase in TDS the molecules in the wetting layer might become mobile enough to form islands, from where they then desorb in form of the observed zero order reaction kinetics. In order to check this possibility the change of the potassium K2p signal was followed as a function of the mean film thickness d at $400\ K$ and $100\ K$, respectively (**Fig. 6.5**).

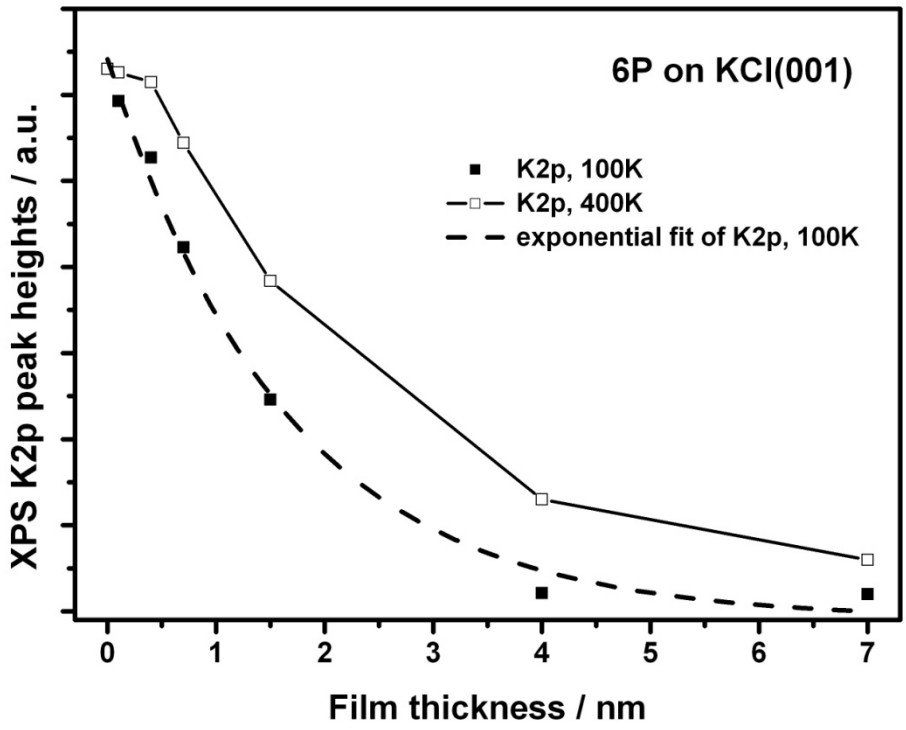

Fig. 6.5: $K2p_{3/2}$ XPS signal as a function of film thickness, grown at $100\ K$ and $400\ K$ substrate temperature, respectively. For the K2p signal at $100\ K$ the data points are fitted by an exponential function. In the other case the line is drawn as a guide to the eye.

At $100\ K$ the p6P molecules are not very mobile and a 'hit and stick' adsorption behavior can be assumed. In fact, in this case the decrease of the substrate K2p signal can be

approximated quite well by an exponential function, as one would expect for an amorphous layer-by-layer growth:

$$\frac{I\,(K\,2p)}{I_0\,(K\,2p)} = \exp\left(-\frac{d}{\lambda}\right) \tag{6.1}$$

A mean free path λ of $1.7\ nm$ for the K2p electrons ($E_{kin} = 961\ eV$) in the p6P film was calculated from this exponential fit. In contrast, if the p6P film was formed at a substrate temperature of $400\ K$ the K2p signal remained nearly constant up to a mean thickness of about $0.5\ nm$. If a wetting layer was formed at this temperature the XPS substrate signal should decrease at least as fast as at $100\ K$. The little change of the substrate signal shows that the molecules are already strongly de-wetting in this low coverage range by forming high islands with small footprints. Interestingly, with a further increase of the coverage the decrease of the substrate signal becomes similar to that at $100\ K$, just shifted by some thickness value. This indicates that further film growth does not proceed in form of islands with high aspect ratios (height vs. footprint), but that rather a continuous layer growth exists. A detailed characterization of films grown at different substrate temperatures is presented in the following sections.

6.2 Investigation of the p6P film morphology by AFM

Fig. 6.6 shows a typical AFM image of a $1.1\ nm$ thick film of p6P on KCl (001) prepared at $400\ K$. The film consists of characteristic p6P needles and in between large irregularly shaped islands can be found.

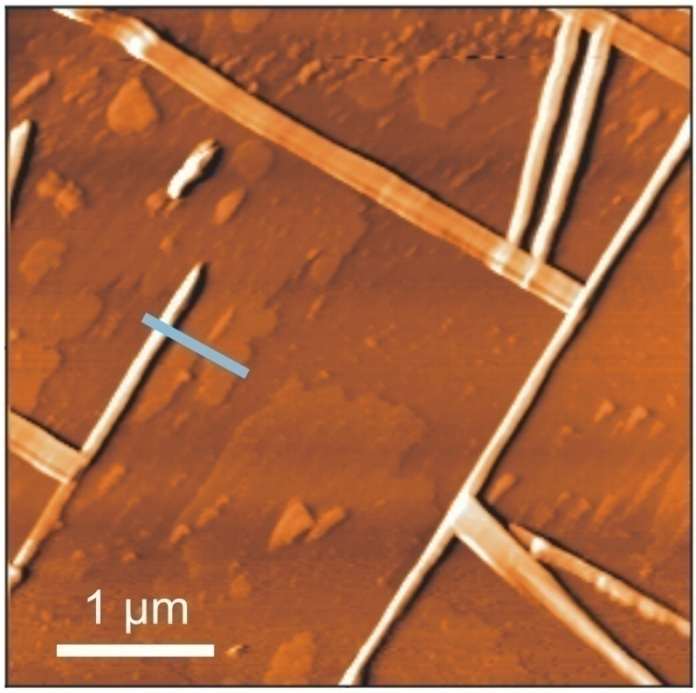

Fig. 6.6: AFM image of a $1.1\ nm$ thick p6P film on KCl (001) grown by PVD at $400\ K$ substrate temperature.

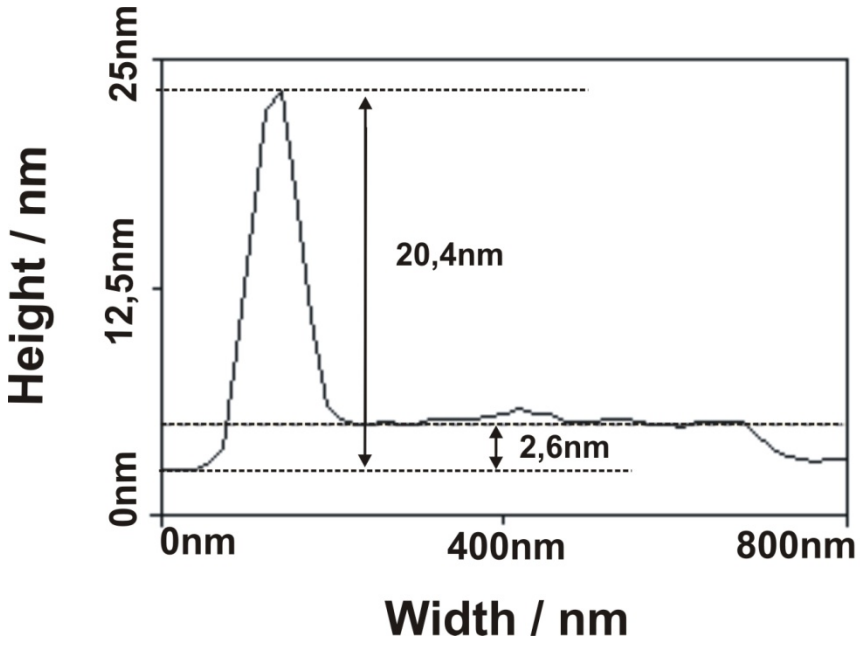

Fig. 6.7: Cross section along the line as depicted in **Fig. 6.6**.

A cross section along the blue line indicated in **Fig. 6.6** is shown in **Fig. 6.7**. The height of the broad terraces is $2.6\ nm$, showing that these islands are formed of standing molecules. The needle like island in this case has a footprint width of about $140\ nm$ and a height of about $20\ nm$. These needles grow mainly along two orthogonal KCl directions, in accordance with the surface symmetry of the substrate. This AFM result agrees quite well with previously obtained morphologies for p6P on KCl (001) grown by hot wall epitaxy (HWE) [47-49]. From XRD and TEM investigations it is known that both, the needle like islands and the terrace-like islands, grow epitaxially on the KCl (001) surface [45, 47]. It has also been shown that indeed the needles consist of side tilted molecules with their long axes being parallel to the surface, whereas the terraced mounds consist of standing molecules with a tilt angle of 17° from the surface normal (see **Fig. 6.8**).

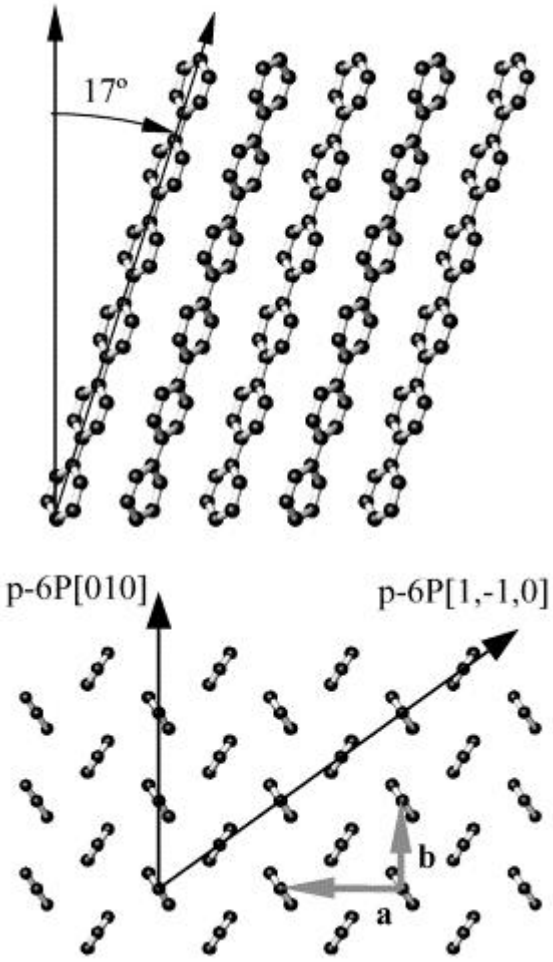

Fig. 6.8: Side view (**a**) and view along the molecular axis (**b**) of a molecular layer of standing molecules. The upper picture shows that the long molecular axes are tilted by 17° from the surface normal. The bottom picture shows the p6P [1−10]-direction (marked arrow) with rows of molecules,

which were found to be lined up with the KCl [110] azimuth. In-plane lattice vectors a and b and the high-symmetry azimuth p6P [010] are also indicated. From [45].

6.3 The influence of the substrate temperature on the p6P film morphology

As already shown in the previous chapter about p6P on mica and many times in the literature, the p6P film morphology in general strongly depends on the substrate temperature. This is of course also the case for p6P on KCl. In **Fig. 6.9**, a compilation of AFM images of films grown at different substrate temperatures is presented. The adsorption temperatures range from $300\ K$ up to $450\ K$ and the associated cross sections can be found in **Fig. 6.10**.

Fig. 6.9a shows an AFM image of a $1\ nm$ thick p6P film grown at room temperature. At this temperature the molecules form very short and mostly elongated islands which grow along preferential rectangular directions according to the four-fold symmetry of the KCl substrate. The islands have an average height of approximately (see **Fig. 6.10a**). No terraces of standing molecules can be seen under these conditions. The formation of needle-like islands on mica (001) comes along with a wetting layer of lying molecules covering the substrate and serving as a template for further film growth. Up to now, p6P on KCl is the first example where islands of lying molecules grow directly on the substrate, instead of growing on a wetting layer. In **Fig. 6.9b–d** AFM images of $1\ nm$ thick p6P films grown at $350\ K$ and $450\ K$ and a $1.1\ nm$ thick film grown at $400\ K$ are shown. These films are in particular suitable for the comparison between films grown by hot-wall epitaxy (HWE) and molecular beam epitaxy (MBE), because the HWE films are typically grown at adsorption temperatures which range from $350\ K$ up to $430\ K$. In general, it is known that the needles (lying molecules) are formed at the initial growth stage and that the terraces (standing molecules) develop after a certain coverage is reached [49]. In **Fig. 6.9b** we see that at $350\ K$ the p6P molecules form long needles which are in principle arranged in a rectangular network, but most of the needles are tilted and do not incline at an angle around 90° [132]. The height of the needles is between 11 and $15\ nm$ (see **Fig. 6.10b**). Few terraces of standing molecules (step height $2.6\ nm$) are observed. In **Fig. 6.9c** ($400\ K$) fewer needles but more terraces are found. The height of the needles is around $20\ nm$ (see **Fig. 6.10c**), that of the terraces is $2.6\ nm$ (standing molecules).

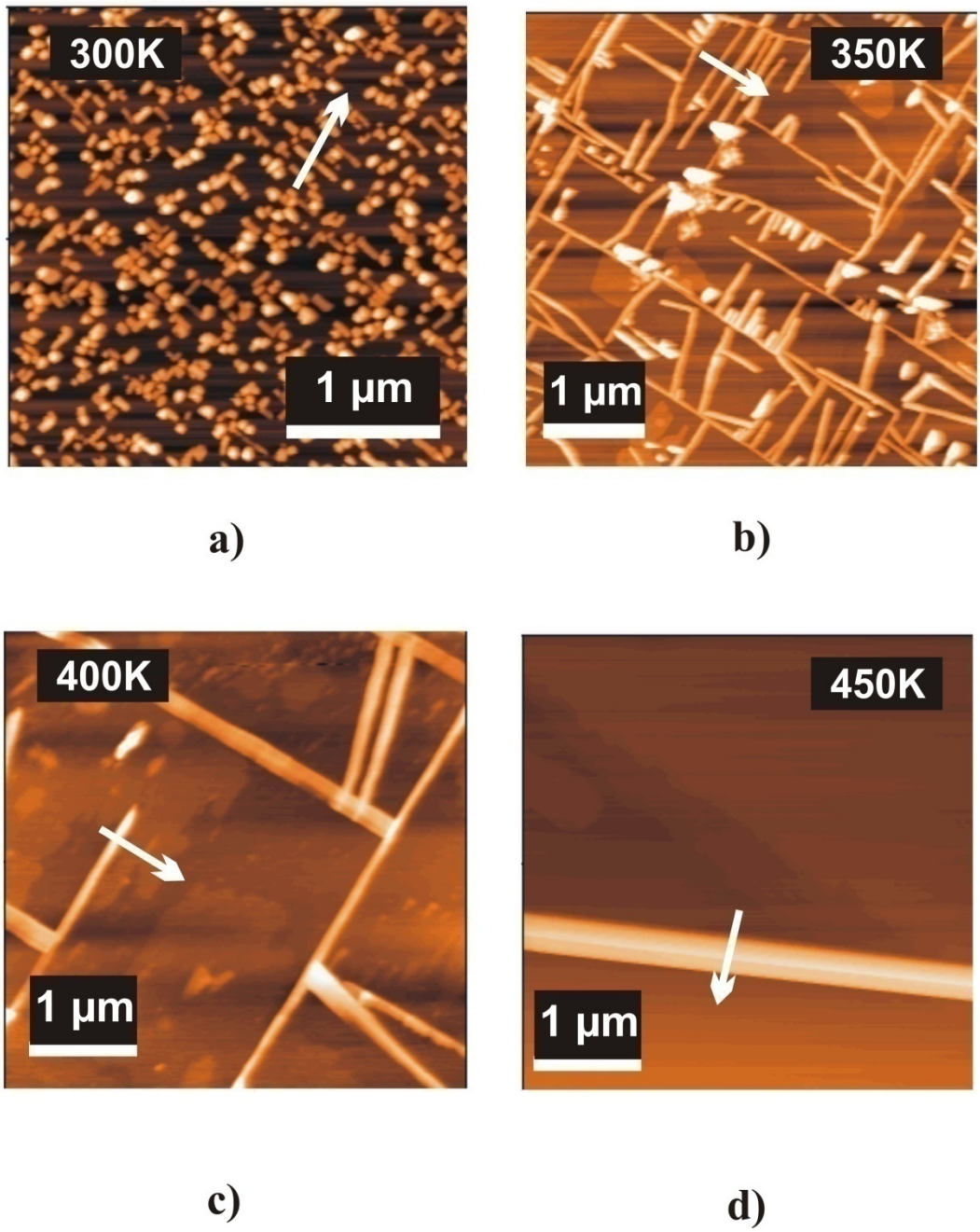

Fig. 6.9: AFM images of p6P films on KCl (001): (**a**) 1 nm grown at $300\ K$, *Z*-scale: $25\ nm$; (**b**) 1 nm grown at $350\ K$, *Z*-scale: $25\ nm$; (**c**) $1.1\ nm$ grown at $400\ K$, *Z*-scale: $35\ nm$; (**d**) $1\ nm$ grown at $450\ K$, *Z*-scale: $200\ nm$. The horizontal trenches, which are in particular visible in (**b**), are artifacts due to the image processing which was applied.

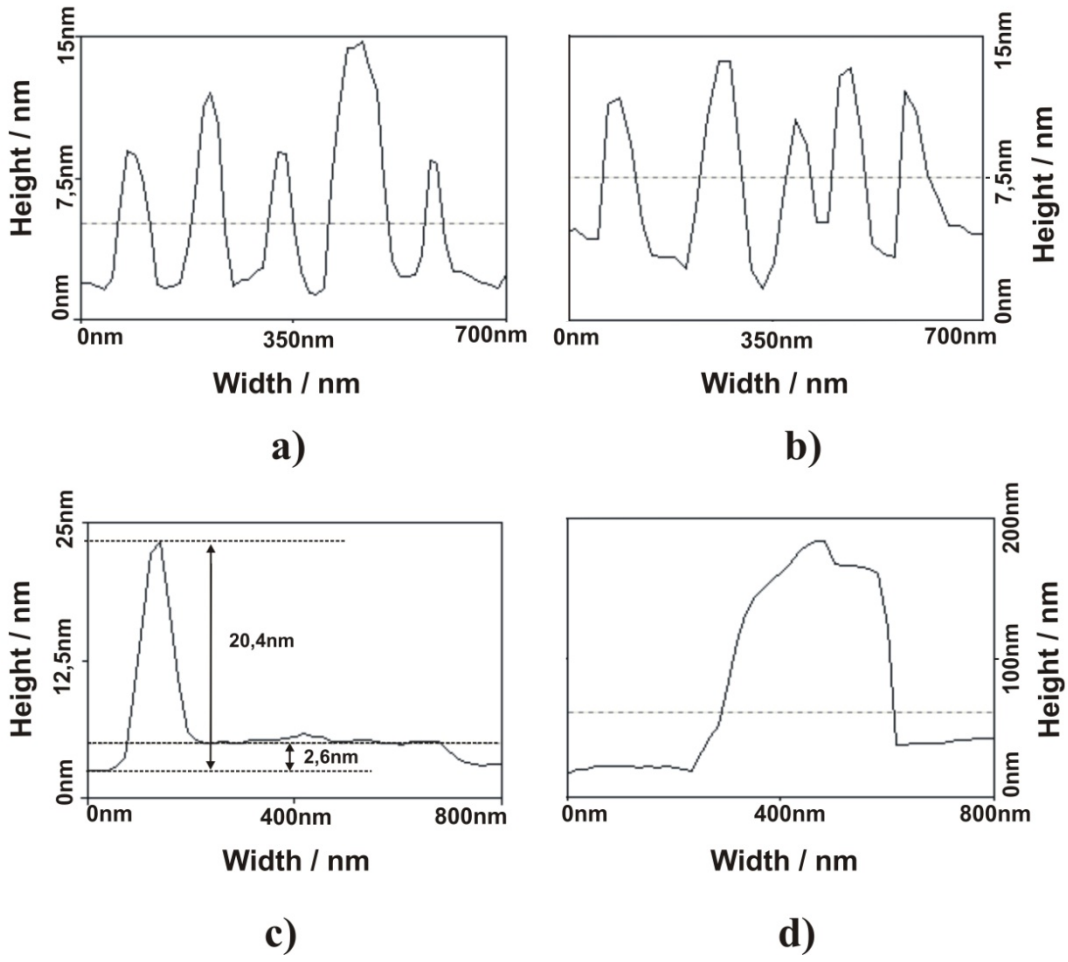

Fig. 6.10: AFM cross sections of the films along the lines as shown in **Fig. 6.9**: (**a**) $1\ nm$ grown at $300\ K$; (**b**) $1\ nm$ grown at $350\ K$; (**c**) $1.1\ nm$ grown at $400\ K$; (**d**) $1\ nm$ grown at $450\ K$.

Here, the needles are well aligned in a rectangular network and only a few of them are shorter and tilted. Finally, in **Fig. 6.9d** the AFM image of a $1\ nm$ thick p6P film grown at $450\ K$ is shown. What one sees is a single needle (cross section shown in **Fig. 6.10d**), which is significantly larger than the needles at lower temperatures in **Fig. 6.9a–c**. Here it seems that all the material is used to build up huge needles, which results in a strong decrease of the needle density. It should be added here that on most parts of the surface no needles can be found at all. Instead, some areas covered only with standing molecules are found.

Figure 6.11 shows a statistical analysis of the films shown in **Fig. 6.9**. For this analysis from five to eight different AFM pictures of each film at the individual temperatures were used. The lateral sizes of the analyzed pictures varied between $4\ \mu m$ and $0.5\ \mu m$.

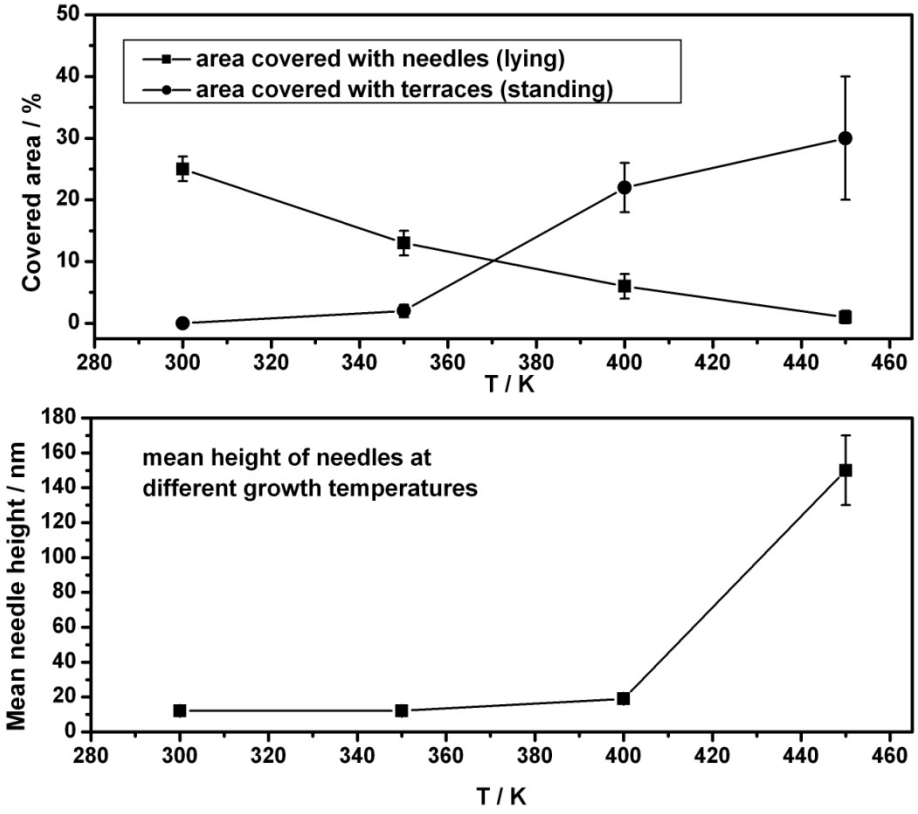

Fig. 6.11: Evolution of film morphology and mean needle height with increasing adsorption temperature for the $1\ nm$ films shown in **Fig. 6.9**. The continuous lines are just guides for the eye.

The figure on top shows how much of the surface area is covered with needles and terraces, respectively. This data was acquired by investigating AFM pictures utilizing a very simple MATLAB program. One can see that with increasing adsorption temperature the needle density decreases, whereas the terrace density, and thus the area covered with standing molecules, increases. The reason for the rather weak increase of terrace density from $400\ K$ to $450\ K$ is that the huge needles at $450\ K$ already contain most of the p6P molecules and therefore not enough material is left to form the terraces. Regarding the $450\ K$ film, it is worth mentioning that on most of the AFM images either needles or terraces are found and only very few images show needles coexisting with terraces. This makes a statistical analysis of the film difficult. The data of this film presented in **Fig. 6.11** is the mean value of the results gained from seven AFM images which were considered to be representative.

It is clear that there might be some error in the statistical analysis of this film since it is not possible to investigate the whole sample, but only small parts of the surface, at once with an

AFM. This is taken into account by the error bars. The figure at the bottom presents the evolution of the mean needle height with increasing temperature. The mean needle height was determined by a careful manual evaluation of numerous AFM cross sections. In the images obtained from the film grown at $450\ K$, only very few needles were found and therefore an uncertainty of the statistical evaluation in this case has to be taken into account. This statistical uncertainty is expressed by an error bar. One can see that the mean needle height slightly increases from $12\ nm$ at $300\ K$ to $19\ nm$ at $400\ K$. Between $400\ K$ and $450\ K$ a huge gain of needle height is observed (from $19\ nm$ to $150\ nm$), which is significantly stronger than the one between $300\ K$ and $400\ K$. This finding has been confirmed by preparation of another film grown at $450\ K$ with a higher film thickness ($7\ nm$). The mean needle height of this $7\ nm$ film is slightly higher, but comparable with the mean needle height of the $1\ nm$ film. With the data given in **Fig. 6.11**, a calculation of the mean film thickness of the different films was conducted. The error of the statistical evaluation is taken into account. The results are: $3.0\ nm$ with an error of $0.7\ nm$ for the $300\ K$ film, $1.8\ nm$ with an error of $0.6\ nm$ for the $350\ K$ film, $1.7\ nm$ with an error of $0.6\ nm$ for the $400\ K$ film and $2.3\ nm$ with an error of $1.5\ nm$ for the $450\ K$ film. By analysis of the AFM images a higher film thickness than the nominal film thickness, according to the microbalance ($1\ nm$ each, except for $1.1\ nm$ for the $400\ K$ film), is obtained. This can be explained by the convolution of the tip with the sample surface. The deviation from the nominal mean thickness is most significant for the $300\ K$ film because here all the islands are much smaller than at higher temperatures. Each steep needle wall causes an error and therefore the error increases with the needle density. The mean film thickness calculation for the film grown at $450\ K$ is not reliable because of its inhomogeneity, which is expressed by a huge error of the result.

When the film thickness is raised to $30\ nm$, as expected [49] the formation of mounds made up of standing molecules prevails for films prepared above RT (**Fig. 6.12**). Comparing the $1\ nm$ thick film with the $30\ nm$ thick film, the density and the size of the needles changes only little, whereas most of the substrate which was uncovered in **Fig. 6.9** is in **Fig. 6.12** covered with standing molecules. These images show that the formation of needle-like islands is favored at and below RT, whereas at elevated temperatures the molecules tend to stand up and form mounds, which resemble the p6P mounds on sputtered mica.

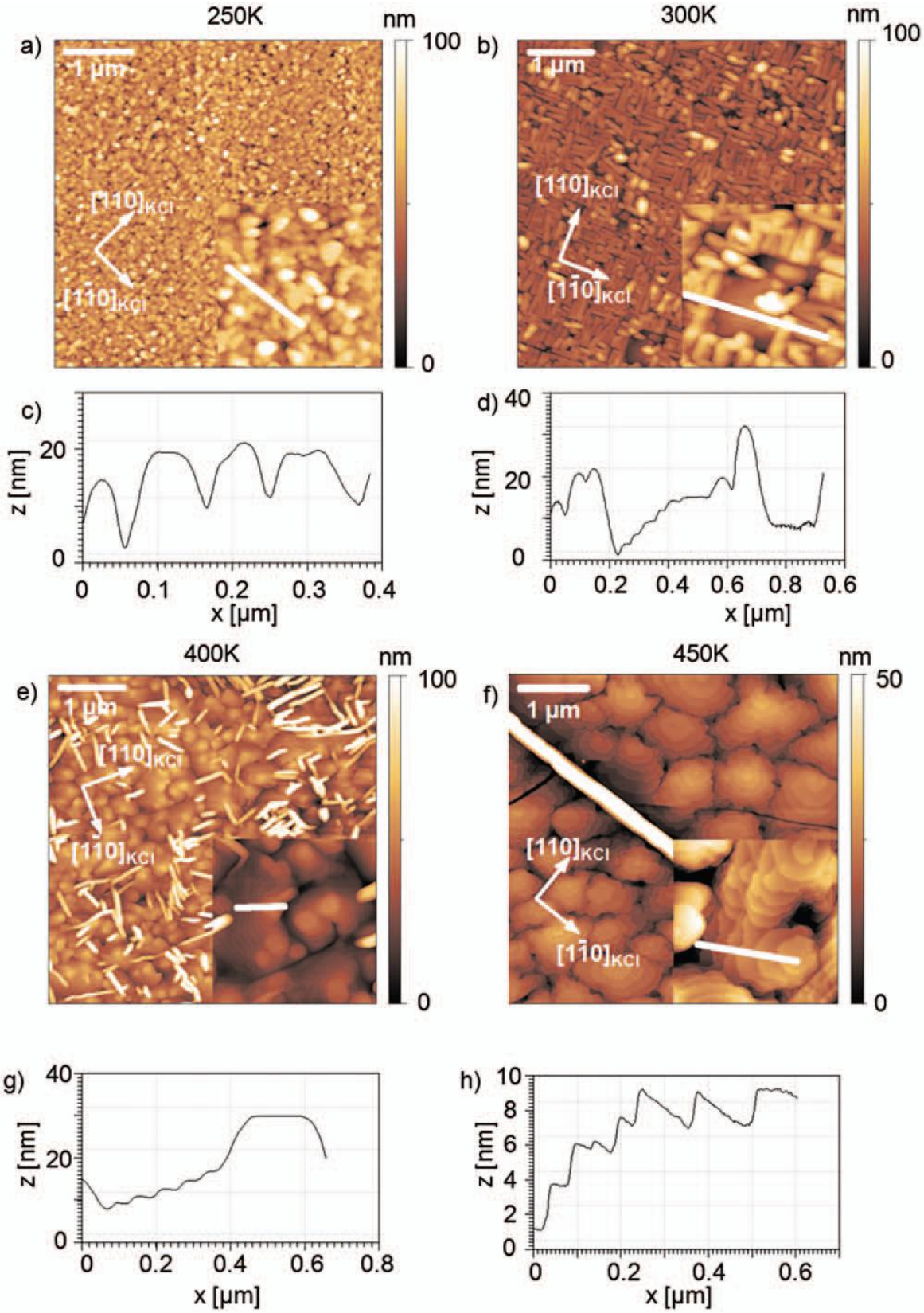

Fig. 6.12: AFM images $(5 \times 5\ \mu m^2)$ of the surface morphology of $30\ nm$ p6P films grown on KCl at different substrate temperatures: **a)** $250\ K$, **b)** $300\ K$, **e)** $400\ K$, **f)** $450\ K$. The insets show corresponding $(1 \times 1\ \mu m^2)$ AFM images. The cross sections along the white lines indicated in the insets are presented in **c)**, **d)**, **e)** and **f)**.

6.4 Thermal stability of p6P films on KCl (001)

So far, it is clear that the adsorption temperature has an important influence on the morphology of the p6P films. In addition, it is interesting to find out what happens with films which are grown at a certain adsorption temperature and then heated. This is in particular important for possible applications of p6P films when grown at a certain temperature and then exposed to a higher temperature. A further aspect concerns the stability of a film grown at low temperatures and then unfrozen to room temperature, where typically ex situ investigations are performed (AFM, XRD). In order to follow temperature-induced changes in situ, combined XPS and TDS measurements were carried out. The height of the XPS C1s signal is a measure of the area which is covered with the p6P film. In **Fig. 6.13** the XPS C1s peak heights of $7\ nm$ thick p6P films grown at different adsorption temperatures as a function of the sample temperature are shown on top. In addition, the TDS spectrum of a representative $7\ nm$ thick p6P film is shown at the bottom.

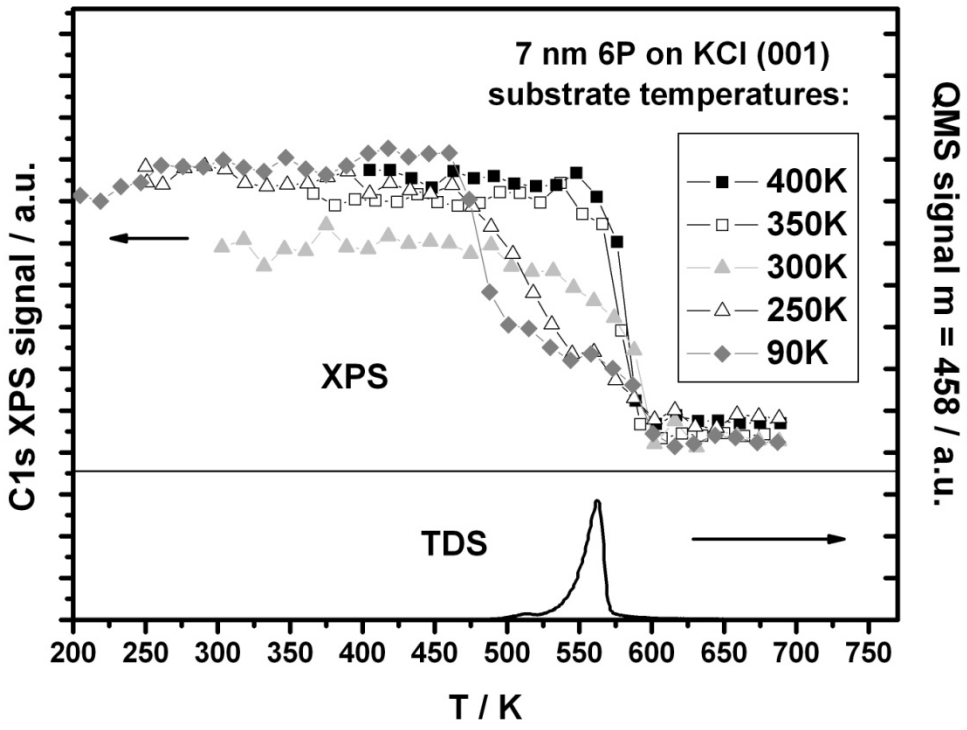

Fig. 6.13: XPS C1s signal heights (**top**) during heating and TDS (**bottom**) of $7\ nm$ thick p6P on KCl (001) grown at different adsorption temperatures.

The common feature of all the different films is the final decrease of the C1s signal around $560\ K$. As one can see in the TDS below, this is the temperature region where the p6P molecules desorb from the surface. During desorption, first the height of the needles will decrease and, since the mean free path of electrons at kinetic energies of about $950\ eV$ in p6P is only $1.7\ nm$ (see section **6.1**), the C1s signal will only change significantly when the height of the needles is in the range of the mean free path. Comparing the initial XPS C1s signals of all the $7\ nm$ thick p6P films grown at different adsorption temperatures, one observes a significantly smaller signal for the film grown at $300\ K$. In order to understand this, we have to look at **Fig. 6.9a–d** and at **Fig. 6.14a**, where an AFM image of a $7\ nm$ thick film grown at $90\ K$ is shown. In **Fig. 6.14a**, the whole surface is covered with short, randomly oriented and distributed islands. The lateral size of these islands ranges from $50\ nm$ up to $200\ nm$. At this low temperature an almost 'hit and stick' behavior for the impinging molecules can be assumed. The molecules are not mobile enough to form elongated and oriented needles like at higher temperatures. The height of these islands is lower; therefore, the island density is higher and more of the surface is covered with p6P than at $300\ K$, where the islands are already elongated and slightly oriented. A similar behavior has already been observed for p6P on mica (**Fig. 5.9**) where the XPS C1s signal decreased with increasing adsorption temperature. On mica, the height of the p6P needles increased with increasing adsorption temperatures, which came along with a decrease of the needle density. The difference on KCl is that the XPS C1s signal has a minimum at $300\ K$ and then increases again with increasing adsorption temperatures (up to $400\ K$). This can be explained by comparing **Fig. 6.9a**, **6.9b** and **6.9c**. At $300\ K$, all the p6P molecules are lying flat on the surface, forming high elongated islands. At temperatures above room temperature, patches of standing molecules are formed. The molecules in these patches cover a larger part of the surface than the same amount of molecules in the form of needles would do. Therefore, the free surface area decreases for adsorption temperatures above $300\ K$ although the needles keep growing higher. At $400\ K$ even more molecules are standing upright than at $350\ K$. Regarding the stability of the different films, one sees in **Fig. 6.13** that the films grown at and above room temperature remain stable upon temperature changes, whereas films grown below room temperature ($90\ K$, $250\ K$) exhibit a change in the XPS C1s signal height during heating already before desorption starts. This indicates a recrystallization taking place

between $450\ K$ and $525\ K$. On the other hand, these films remain stable up to room temperature, which means that no information on these films is lost during 'unfreezing'. To obtain information on the morphology of such a recrystallized structure, a film was prepared at $90\ K$ and then heated to $525\ K$, a temperature where the recrystallization has already taken place. An AFM image of this particular film is shown in **Fig. 6.14b**. For comparison in **Fig. 6.14a** a film grown at 90 K is shown which has not been heated.

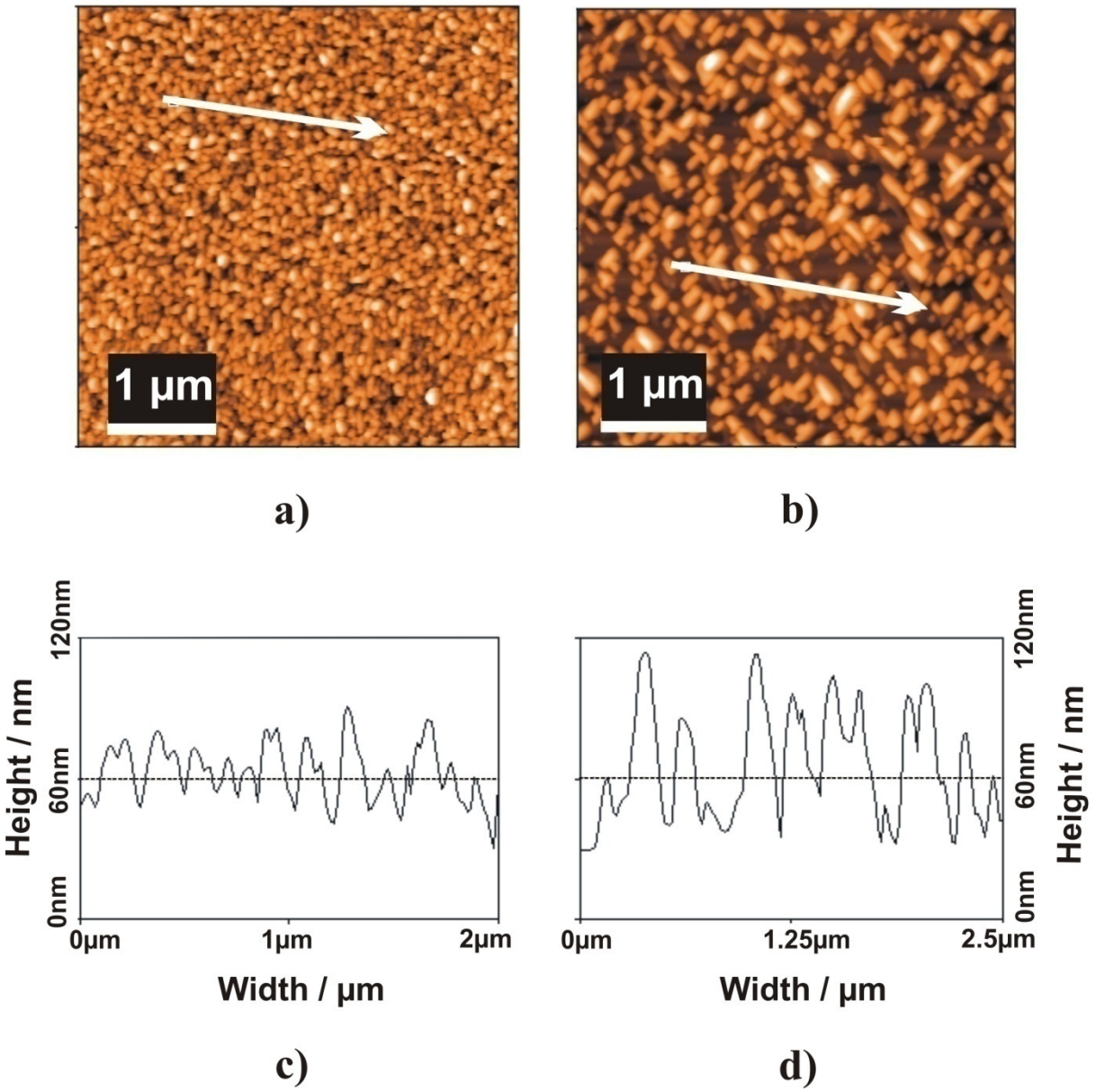

Fig. 6.14: AFM images of $7\ nm$ p6P on KCl (001): (**a**) grown at $90\ K$, image taken at room temperature, *Z*-scale: $70\ nm$; (**b**) grown at $90\ K$ and then heated to $525\ K$, *Z*-scale: $140\ nm$; (**c**) cross section of (**a**); (**d**) cross section of (**b**)

Comparing the film ‘before’ (**Fig. 6.14a**) and ‘after’ (**Fig. 6.14b**) recrystallization, one observes a significant change of the film morphology. While in **Fig. 6.14a** nearly all the KCl surface is covered with randomly arranged and randomly oriented islands with an average height of (**Fig. 6.14c**), we see in **Fig. 6.14b** that parts of the surface remain uncovered and that the islands with an average height of (**Fig. 5d**) are already oriented according to the four-fold symmetry of the substrate. Thus, the result of the recrystallization is a film consisting of slightly elongated and ordered islands which are significantly higher than the ones before the recrystallization.

7 HATCN on Au (111)

In this chapter the purification of the used HATCN molecules is explained in detail. The dry chemical as received from the group of Klaus Müllen (Max Planck Institute of Polymer Research in Mainz) contained to some extent residual solvent, namely acetonitrile (CH_3CN), which could be eliminated by annealing the source. The layer growth of this discoid molecular acceptor is rather complicated. The same applies to the desorption kinetics, which could be elucidated by the application of the heating rate variation method though, as described in section **4.3.1**, and by doing 'XPS vs temperature' measurements. Supplemental XRD and AFM investigations corroborated the growth model which arose from the thermal desorption studies.

7.1 Purification of HATCN and the cracking pattern

In order to determine the cracking pattern and to purify the HATCN dry chemical, the molecules were desorbed directly from the Knudsen cell into the QMS. A mass spectrum of the HATCN material as received at $380\ K$ is shown in **Fig. 7.1**. The base pressure in the vacuum chamber was around $1 \times 10^{-7}\ torr$, therefore the signal of residual gas components like CO, N_2, O_2 or H_2O was rather high. Nevertheless, also a high amount of the solvent acetonitrile (CH_3CN) was found. During long-time heating of the source ($\approx 12\ h$) up to $450\ K$, the decrease of the acetonitrile signal could be followed until the signal eventually disappeared. After the purification of the HATCN material the cracking pattern (**Fig. 7.2**) was determined by heating the source to about $500\ K$. Due to the high ionization energy ($E_I = 70\ eV$) of the QMS that was used, the signal of the intact molecule is relatively small compared to the signals of its cracking products. A detailed view of the higher masses is shown in **Fig. 7.3**, where the interval from $mass\ 200$ to $mass\ 400$ of the same cracking pattern is shown.

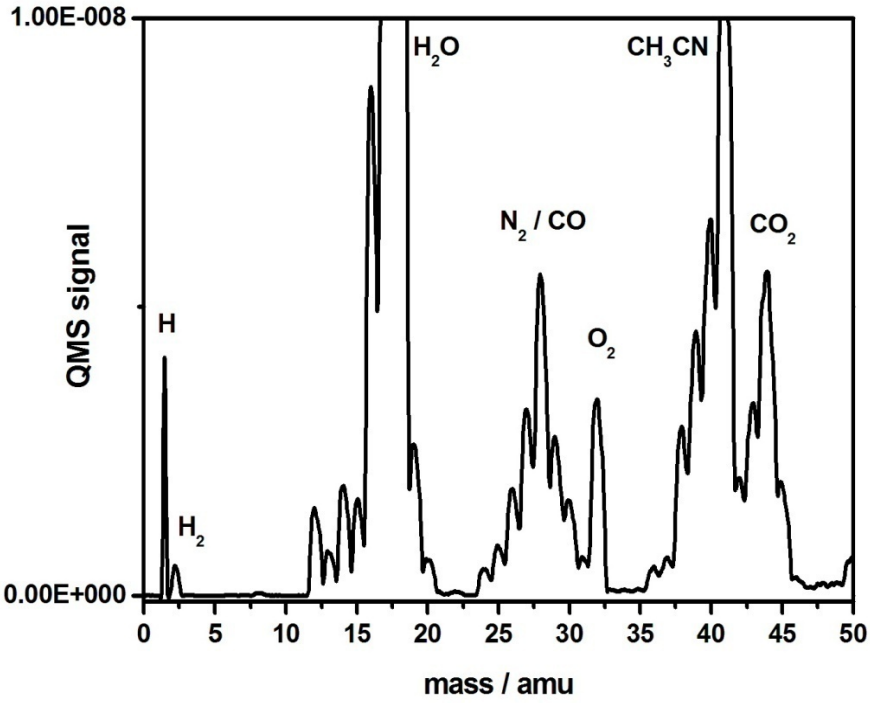

Fig. 7.1: Mass spectrum of the HATCN material as received, taken at $380\ K$. Apart from residual gas, the solvent acetonitrile (CH_3CN, $m = 41$) was seen, which stems from the synthesis of HATCN.

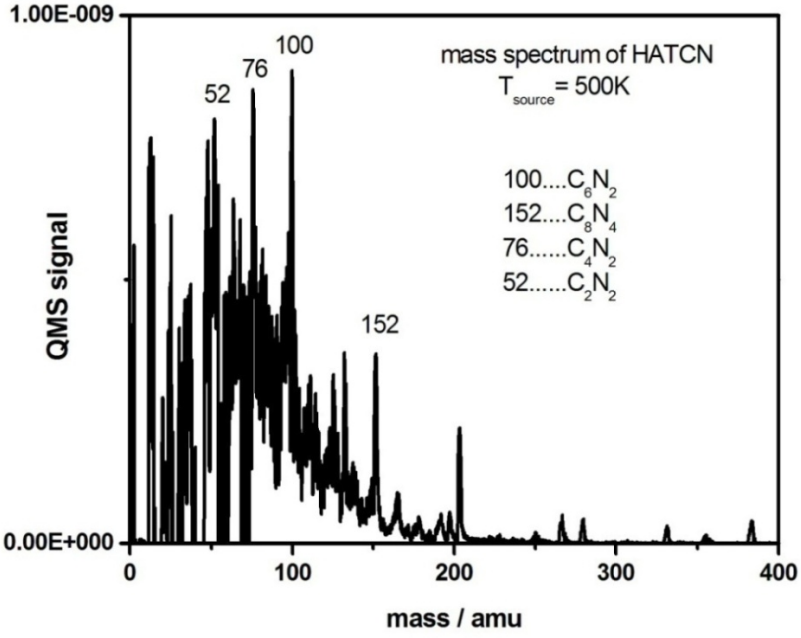

Fig. 7.2: Cracking pattern of HATCN, source heated to $500\ K$. Selected peak positions, mostly of the peaks with the highest intensity, are indicated and identified.

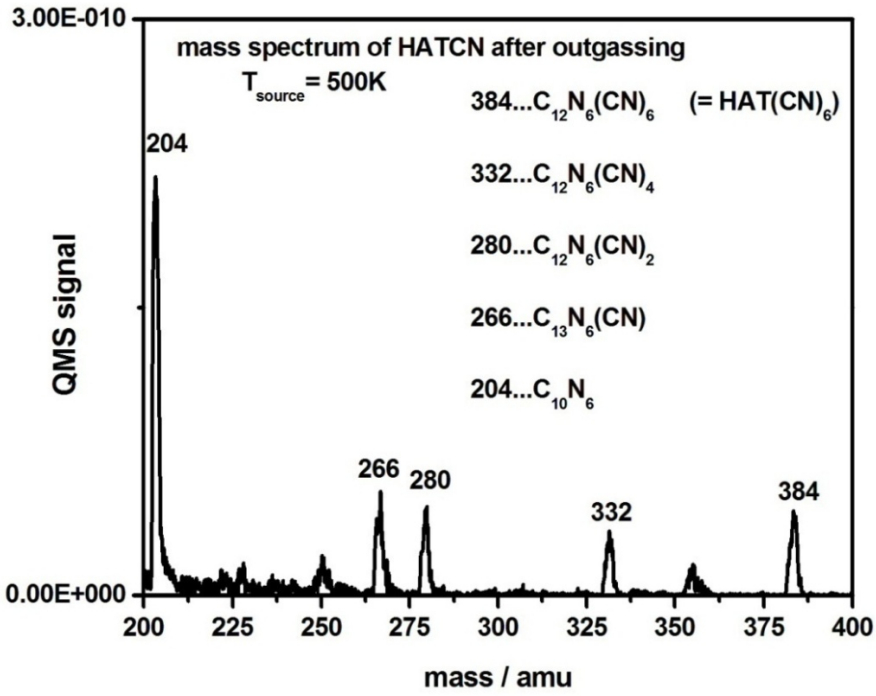

Fig. 7.3: Detailed view of the cracking pattern for masses above $m = 200\ amu$ plus peak positions and identification of the peaks.

The cracking pattern contains a variety of different peaks, which can predominantly be identified as C_xN_x fragments. The mass of the intact molecule is correctly found to be $384\ amu$. Most of the peaks in the cracking pattern can be correlated to each other by adding or subtracting $52\ amu$ (C_2N_2), which is one of the most likely formed cracking products among $mass\ 76$ and $mass\ 100$. For the multiplexed TDS experiments, the QMS was tuned to the masses with the highest intensities like $52, 100, 152, 204, 280, 332$ and 384. In successive TD experiments of films desorbing from Au (111) and Ag (111) it turned out that except $mass\ 52$, all the other multiplexed masses proceeded proportional to each other if no cracking on the substrate occurred, which was the case for the Au substrate. Therefore in the TDS images shown in this chapter only the mass with the highest intensity is shown, which was in our case $mass\ 100$. On Ag (111), it was observed that apart from cracking in the QMS, also cracking on the surface occurred (more details see chapter **8**).

7.2 The initial layer growth of HATCN on Au (111)

A typical series of TD-spectra of the extended monolayer regime (nominal mean film thickness $\leq 7\text{Å}$) is shown in **Fig. 7.4**. This series was obtained from films that were grown at a substrate temperature of $200\ K$. Equivalent spectra were obtained for films grown from $100\ K$ up to $400\ K$. In order to get the correct values for the absolute desorption rate that are shown in **Fig. 7.4**, a correlation between the measured quartz frequency change and the adsorbed amount on the sample surface in terms of monolayers had to be found. For this purpose discoid molecules (van der Waals diameter $\approx 1.5\ nm$) were assumed. The number of HATCN molecules in a densely packed layer of circular disks can be calculated to be $5.1 \times 10^{15}\ \frac{molecules}{cm^2}$. This corresponds to a quartz frequency change of $\approx 2.55\ Hz$ for the experimental setup (see **table 4.1**). With this information, a quantitative evaluation of the desorption spectra can be performed. A frequency change of $1\ Hz$ at the quartz microbalance corresponds to a thickness increase of $0.81\ \text{Å}$ (see again **table 4.1**). In Ref. [66] a different value for the density of HATCN was used (1.3 instead of 1.6 [58]) which led to a different conversion factor between the frequency change in Hz and the mean film thickness ($1\ Hz \approx 1\ \text{Å}$ instead of $1\ Hz \approx 0.81$).

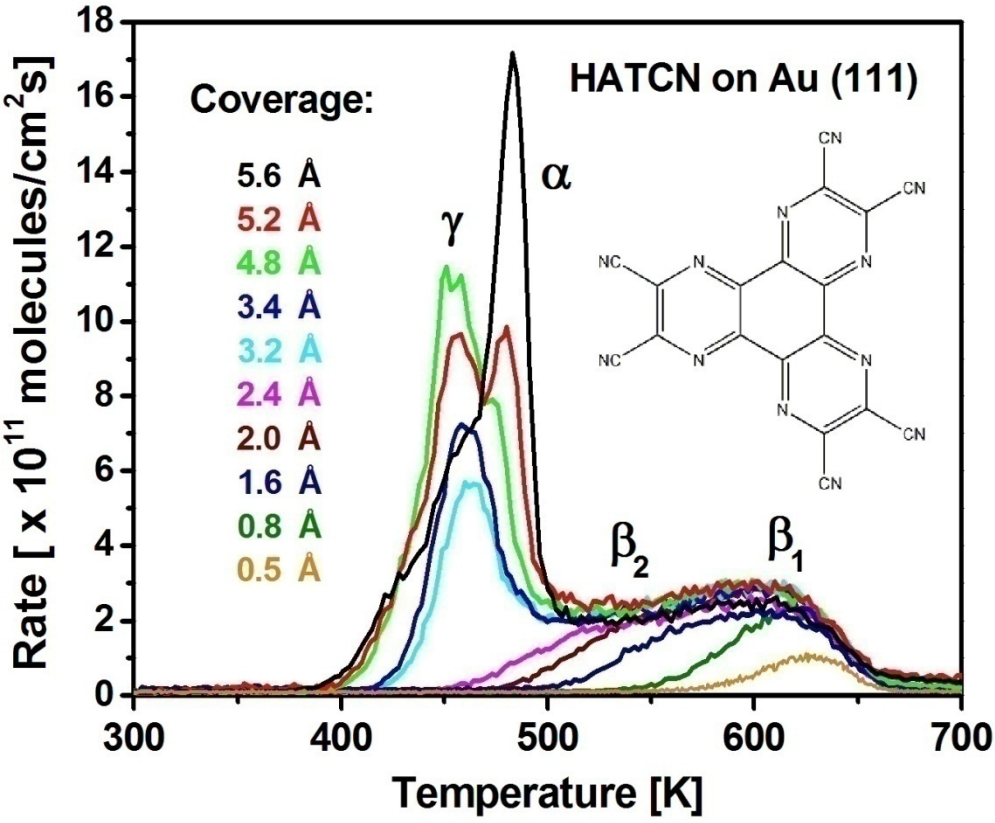

Fig. 7.4: Series of thermal desorption spectra of HATCN on Au (111) as a function of coverage. Adsorption temperature $200\ K$, heating rate: $1\frac{K}{s}$. The chemical structure of a single HATCN molecule is depicted in the insert.

The evolution of the desorption spectra can be divided into four different regimes:

- For coverages corresponding to less than $1.2\ \text{Å}$, (as based on our coverage calibration with the quartz microbalance) HATCN desorbs at $\approx 620\ K$. A small shift to lower temperature (by $< 10\ K$) with increasing coverage is observed. This peak is labeled as β_1 and it corresponds to a coverage of about ½ monolayer of flat lying molecules.

- For coverages above $1.2\ \text{Å}$ the desorption spectra exhibit a shoulder at the leading edge of the β_1 peak which shifts considerably (by more than $100\ K$) when increasing the coverage up to about $2.4\ \text{Å}$ (full monolayer). This additional feature is designated

as the β_2 peak and signifies the completion of the first layer of molecules lying flat on the surface.

- With further increase of the coverage a third, sharp desorption peak appears at $\approx 460\ K$. This peak increases in intensity up to a coverage of $\approx 4.8\ \text{Å}$, with a slight shift of the peak to lower temperature. This peak is designated as the γ peak, which corresponds to a 2nd layer of flat lying molecules.

- Interestingly, a further increase of the coverage leads to the disappearance of the γ peak and a new peak at a higher temperature ($\approx 480\ K$) emerges. This latter peak, designated as the α peak, shows the typical feature of zero order desorption (common leading edge for various initial coverages) and corresponds to desorption from the multilayer, which is going to be described in detail in the following sections. Thus, the second layer of flat lying molecules is integrated into the bulk structure.

The calculation of the kinetic desorption parameters of the β_1 and the γ peak was performed using the heating rate variation method (described in section **4.3.1 Theoretical background**). For that purpose five different heating rates β were applied. In **Fig. 7.5**, a series of TD-spectra with approximately the same film thickness ($4.8\ \text{Å}$), but different heating rates is presented. The peak maxima of the particular peaks shift to higher temperatures with increasing heating rates and the extent of this shift gives information on the desorption energy and on the pre-exponential factor, as described in eq. 4.11.

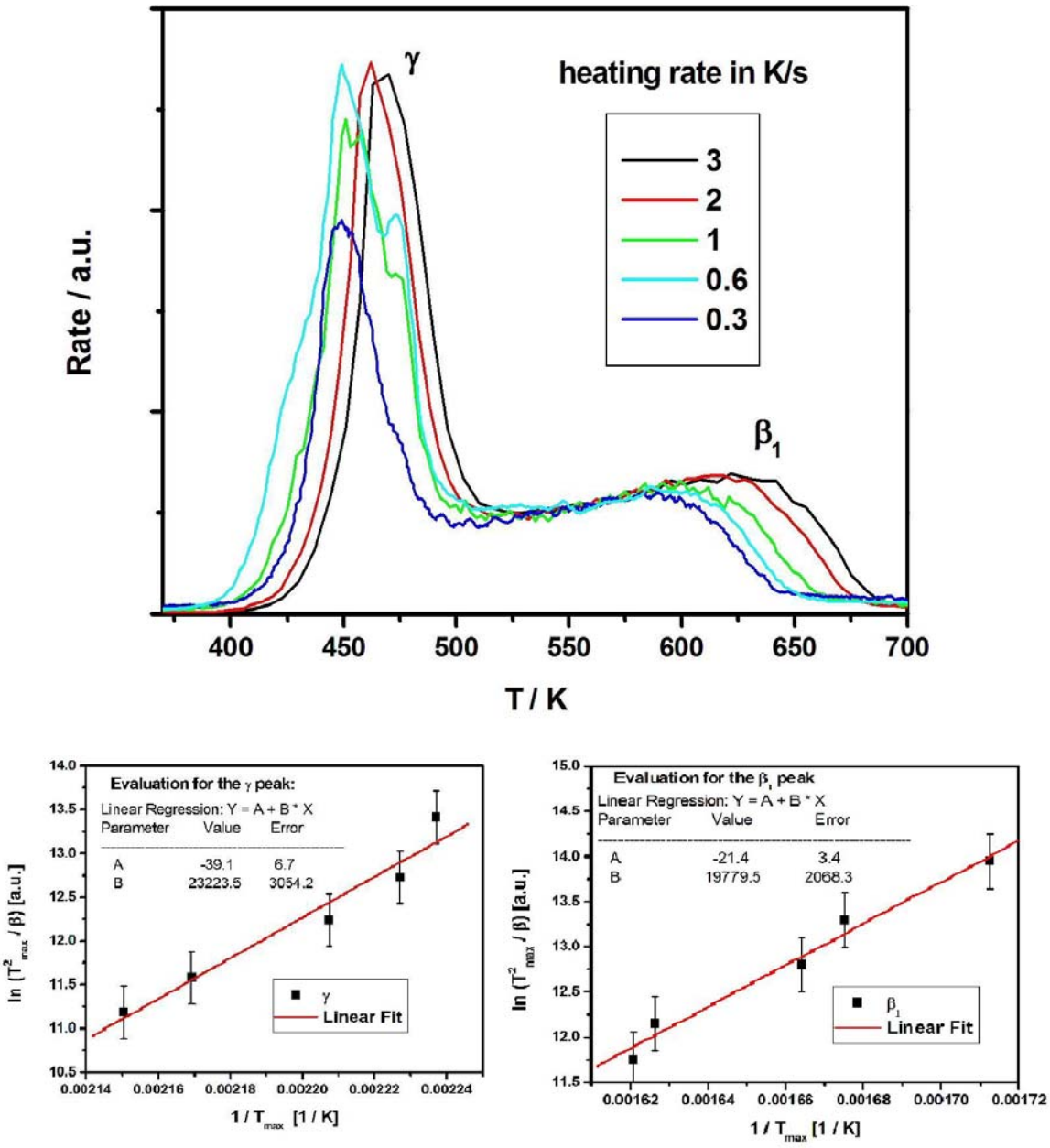

Fig. 7.5: Top: Series of TD-spectra obtained by applying different heating rates. Nominal mean film thickness in all cases $\approx$ **4.8 Å** . The shift of the peak maxima is used for the calculation of the kinetic desorption parameters. In this figure, the intensity of the individual spectra was normalized so as to visualize the shift of the peak maxima. **Bottom:** Evaluation for the γ peak and the β_1 peak. Parameters *A* and *B* of the linear fits can be used to calculate E_{des} and ν_1: $E_{des}\,[eV] \approx \frac{2 \cdot B}{23000}$, $\nu_1\,[s^{-1}] = \frac{B}{2 \cdot \exp(A)}$

The shift of the peak maximum of the β_1 peak is $\approx 50\ K$, the shift of the γ peak only $\approx 20\ K$. From this finding one could already guess that the kinetic parameters of these two adsorption/desorption states must be very different. A quantitative evaluation (**Fig. 7.5**, **bottom**) of various sets of desorption spectra, each set containing spectra with different heating rates and same film thickness, indeed yielded

$$E_{des}(\beta_1) = 1.7 \pm 0.2\ eV$$

$$\nu(\beta_1) = 1 \times 10^{13\pm2}\ s^{-1}$$

and

$$E_{des}(\gamma) = 2.0 \pm 0.2\ eV$$

$$\nu(\gamma) = 1 \times 10^{21\pm3}\ s^{-1}$$

Surprisingly, the binding energies of both states are calculated to be pretty similar, whereas apparently the difference of their desorption temperatures is only caused by different pre-exponential factors. For the β_2 state the peak maxima are not defined well enough to perform a quantitative evaluation, but from the qualitative similarity to the β_1 peak behavior a similar pre-exponential factor as for the β_1 state is proposed. The quantitative error for this type of evaluation is by nature larger than for a leading edge evaluation, due to the limited range of the heating rate variation (only five different heating rates were applied). The physical

meaning of the values of these parameters will be discussed in detail in the next section, after the calculation of the kinetic parameters of the multilayer (α) peak.

7.3 Further development of the film growth

Having a closer look at **Fig. 7.4**, one notices that the onset of the black curve ($5.6\ \text{Å}$) is not 'smooth', i.e. a certain amount of molecules still resides in the γ state, and that in the range from $500\ K$ up to $650\ K$ the black curve proceeds below the other ones, indicating a slight decrease of the high-temperature β peaks with increasing film thickness. The latter observation can also be followed explicitly in **Fig. 7.6**, which shows a series of thermal desorption spectra from $5.6\ \text{Å}$ up to $50\ \text{Å}$ mean film thickness.

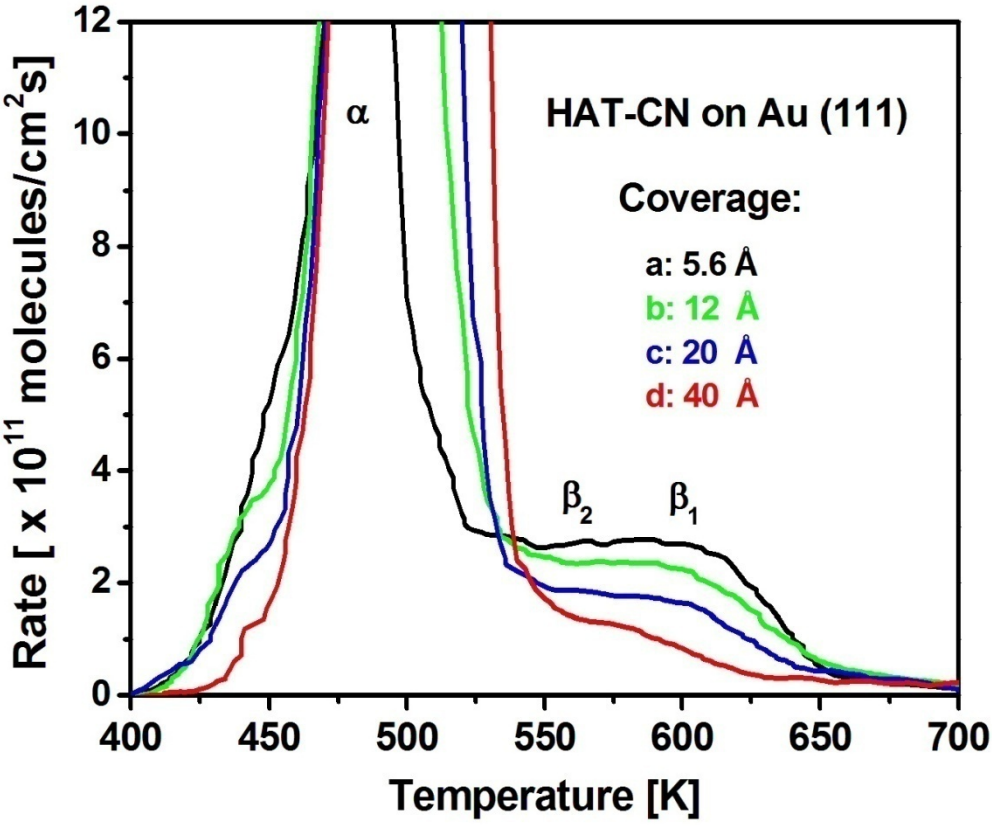

Fig. 7.6: Series of thermal desorption spectra of HATCN on Au (111) for larger coverages. Adsorption temperature: $200\ K$, heating rate $1\frac{K}{s}$. **a**) – **d**): Different initial coverages.

With increasing initial coverage the amount of molecules desorbing from the β_1 and β_2 peak decreases continuously. At a coverage of $40\ \text{Å}$ less than 20 % of a monolayer (flat lying molecules) desorb from the β_1 and β_2 states and no molecules from the γ state anymore. Thus, not only the low-temperature γ peak gets integrated into the bulk phase, but also the high-temperature β peaks. This finding is illustrated in **Fig. 7.7**, where the amount of molecules in the separate adsorption states is plotted as a function of the nominal mean film thickness.

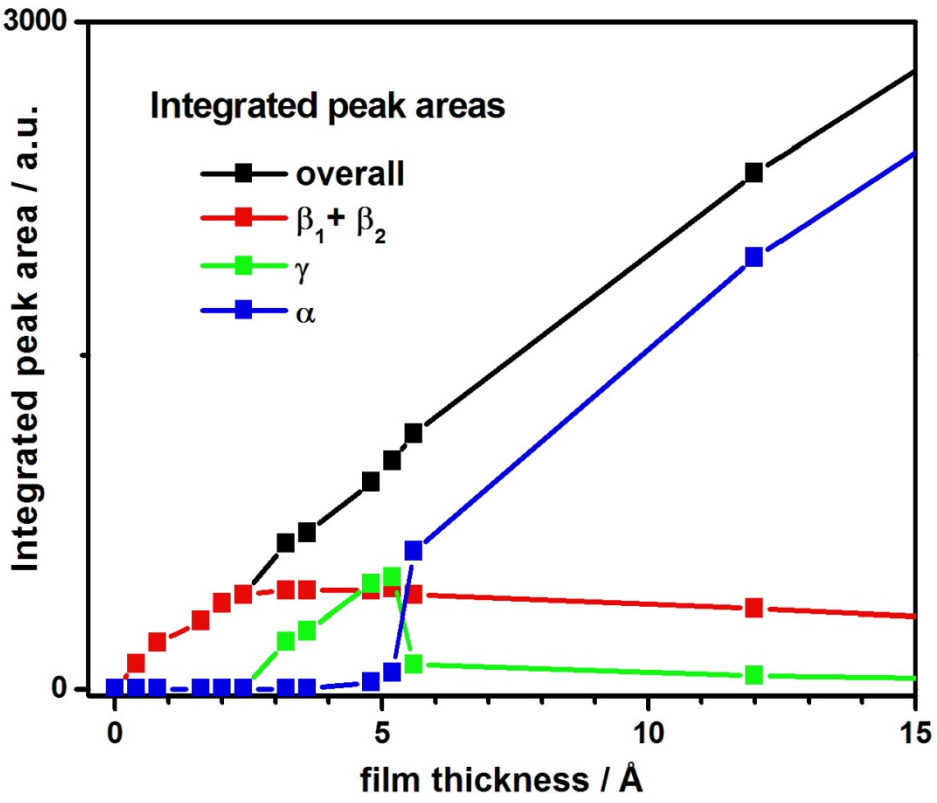

Fig. 7.7: Integrals of the separated TDS peaks and their sum from measurements such as in **Fig. 7.4** and **Fig. 7.6** as a function of mean film thickness. Heating rate $\frac{dT}{dt} = 1\frac{K}{s}$ in all cases. The parallel slopes indicate equal sticking coefficients for the various states which then is very likely equal to unity.

The linear slope of the overall sum of the peaks indicates a constant sticking coefficient during the whole adsorption process. The same holds for each of the various adsorption states and thus it is reasonable to assume a sticking coefficient of 1. The curve subtends the zero-

point, which indicates that all the molecules which were adsorbed at the surface subsequently desorbed from the surface upon heating. In other words: there is no dissociation of the HATCN molecules on the Au (111) surface.

The leading edge of the multilayer peak can be used to calculate the desorption energy and the pre-exponential factor:

$$E_{des}(\alpha) = 1.84 \pm 0.1\ eV$$

$$\nu(\alpha) = 1 \times 10^{19\pm1}\ s^{-1}$$

Comparing the desorption parameters of the three distinct adsorption states (α, β_1, γ), which have been determined in this section and in the previous one, it attracts attention that all the desorption energies are nearly the same (within the error). Actually, there is even an opposite trend between the desorption peak maxima and the desorption energies. Hence, the difference of the desorption temperatures for the individual adsorption states is mainly determined by the pre-exponential factors. Both, the multilayer peak (α) as well as the second layer peak (γ) exhibit the large pre-exponential factor expected for large molecules. Surprisingly, the monolayer peaks (β) show a very small pre-exponential factor, usually only observed for small particle (atom, diatomic molecule) desorption. According to the definition of the pre-exponential factor ν (eq. 4.7), the partition function of the molecules in the first monolayer is similar to that in the gaseous phase at the desorption temperature. In other words, the translational and rotational degrees of freedom are already highly excited in the adsorbed phase when desorption starts. Apparently, the activation energy for surface diffusion of the large HATCN molecules on the inert gold surface is very small and the molecules behave like a two-dimensional gas. The high pre-exponential factors for desorption from the 2nd layer and

the bulk phase indicate that only little excitation of the various degrees of freedom takes place prior to desorption. This is the case if the molecules are rather immobile.

As a matter of fact all the information gained by TDS is only valid at or directly below the desorption temperature. In order to find out whether the integration of the first two layers (β + γ) into the bulk phase α happens upon adsorption or during heating the substrate, it is necessary to examine the temperature dependence of the film morphology.

7.4 The influence of the substrate temperature

XPS was used to analyze the film morphology in-situ. **Fig. 7.8** shows the height of the C1s, N1s and the Au4f$_{7/2}$ XPS signals for a film thickness of $15\ Hz$, which corresponds to $1.2\ nm$, as a function of the substrate temperature during film preparation. The signals remain more or less constant up to $300\ K$, but when going to higher temperatures the substrate signal increases while the adsorbate signals decrease. This indicates a change in film morphology above room temperature, which will be explained in detail in the following.

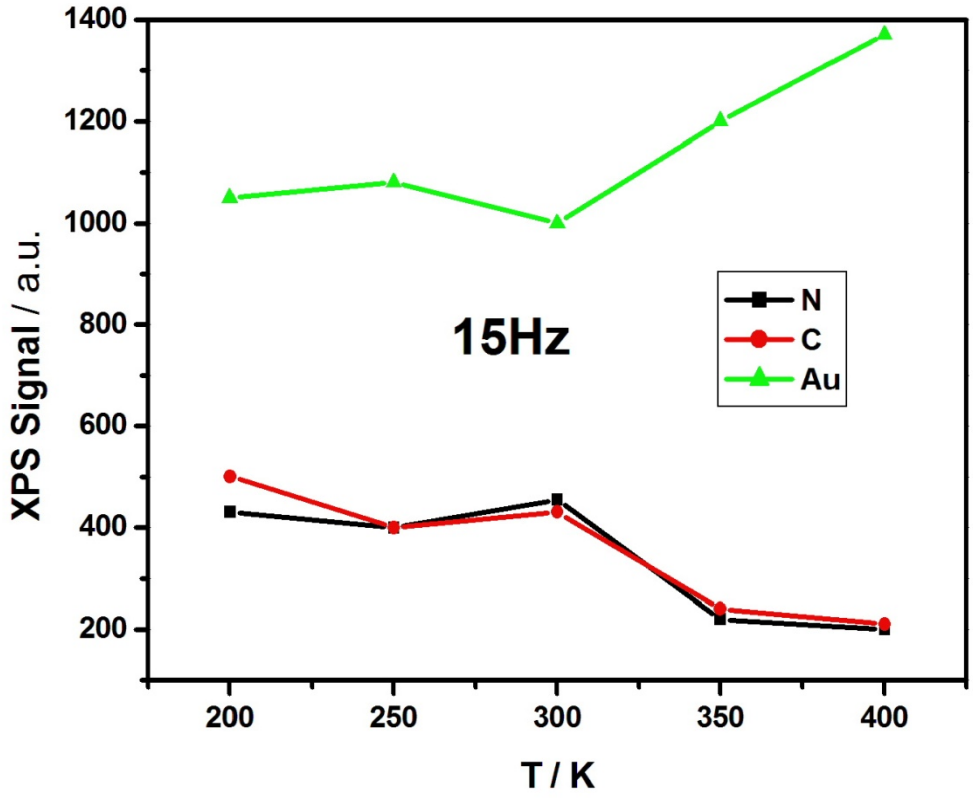

Fig.7.8: XPS signal heights of the substrate ($Au4f_{7/2}$) and the HATCN molecules (C1s and N1s) as a function of substrate temperature during film preparation. The sharp bend at room temperature points out a change of the film morphology. $15\,Hz$ correspond to a mean film thickness of $\approx 12\,Å$.

The next figures show the XPS signal heights against the film thickness for two films, one of them prepared at a rather low temperature ($200\,K$, **Fig. 7.9**), the other one prepared at a rather high temperature ($400\,K$, **Fig. 7.10**).

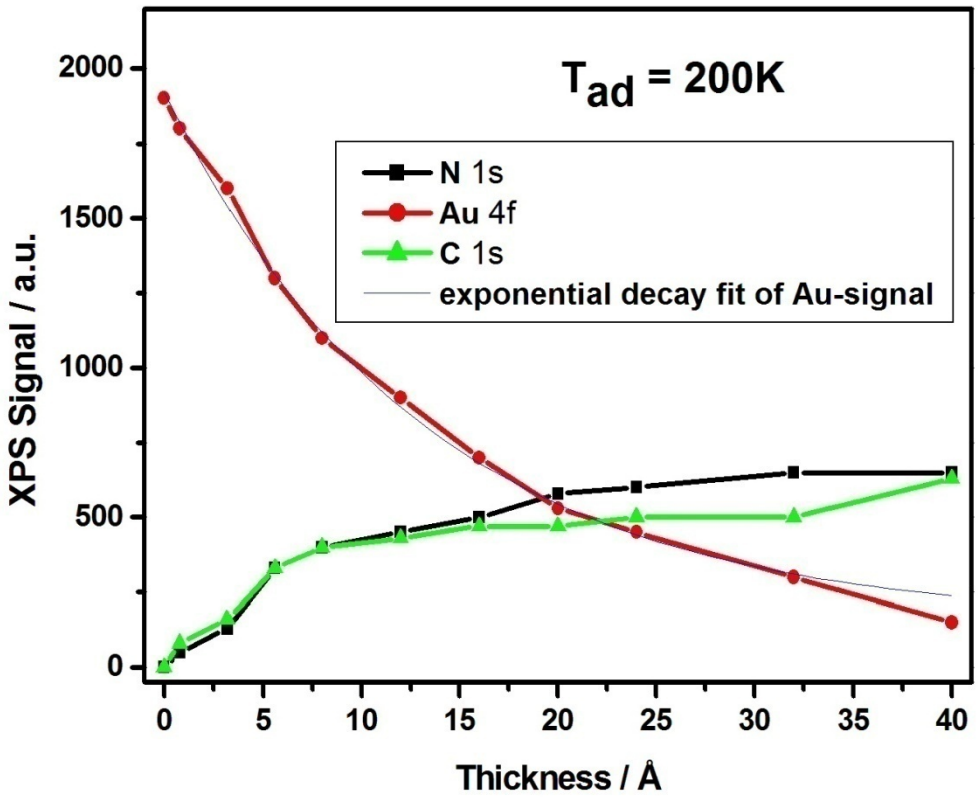

Fig.7.9: XPS signal heights of the substrate (Au $4f_{7/2}$) and the HATCN molecules (C1s and N1s) as a function of mean film thickness. Substrate temperature: $200\,K$. Blue: Exponential decay fitted to the Au4f signal which yields for the inelastic mean free path of the Au4f electrons $\lambda = 13.3\,Å$.

The substrate signal in **Fig. 7.9** can be approximated by an exponential decay,

$$\frac{I\left(Au\ 4f_{\frac{7}{2}}\right)}{I_0\left(Au\ 4f_{\frac{7}{2}}\right)} = \exp\left(-\frac{d}{\lambda}\right)$$

(7.1)

indicating that at this temperature the multilayer grows in a layer-by-layer like fashion (hit and stick behavior). From the exponential signal decay an inelastic mean free path for the Au4f photoelectrons ($E_{kin} = 1170\ eV$) of $\lambda = 13.3\ \text{Å}$ is determined. This value is significantly lower than the inelastic mean free path of electrons in p6P ($\lambda_{p6P} = 25\ \text{Å}$) [60] and p4P ($\lambda_{p4P} = 24\ \text{Å}$) [30].

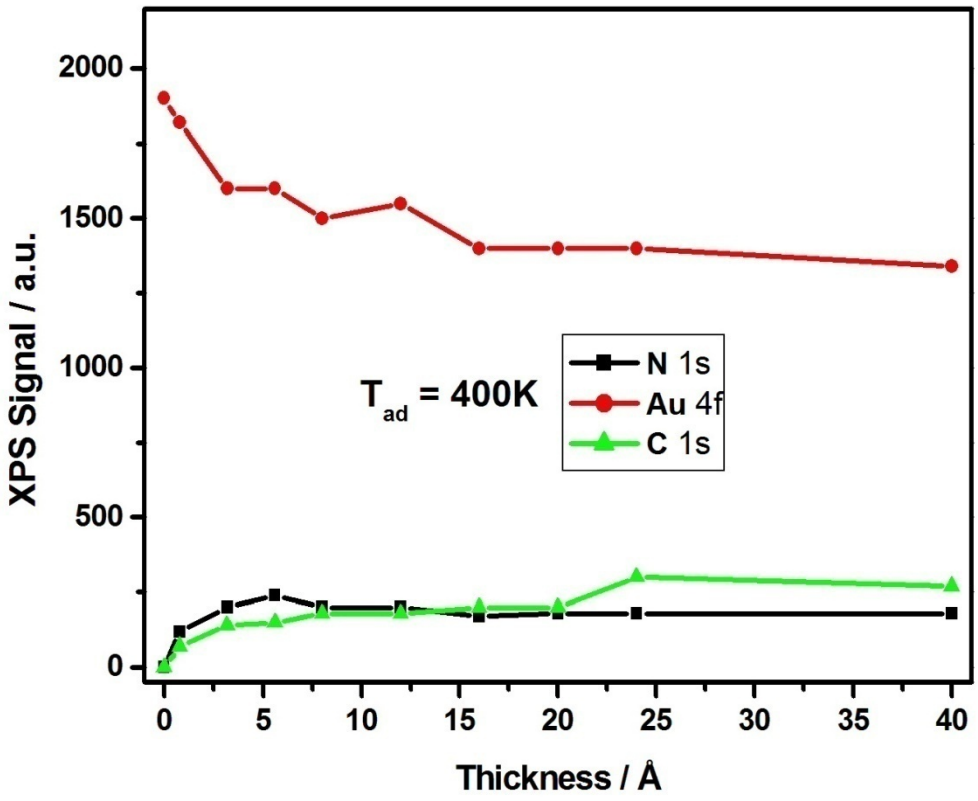

Fig. 7.10: XPS signal heights of the substrate ($Au4f_{7/2}$) and the HATCN molecules (C1s and N1s) as a function of mean film thickness. Substrate temperature: $400\ K$.

The substrate signal in **Fig. 7.10** decreases only at the beginning and remains almost constant above $16\ \text{Å}$. This is a sign of strong dewetting, i.e. island formation. Additional molecules tend to join the islands instead of covering the substrate.

In **Fig. 7.11a** and **7.11b** AFM images are presented for $16\ \text{Å}$ thick HATCN films grown on the Au (111) substrate at $300\ K$ and at $400\ K$. The AFM image of the film grown at $300\ K$ shows that the Au surface is nearly completely covered with the organic film, consisting of grains with an average diameter of $\approx 200\ nm$. From a cross section analysis a mean grain height of $3-4\ nm$ is obtained.

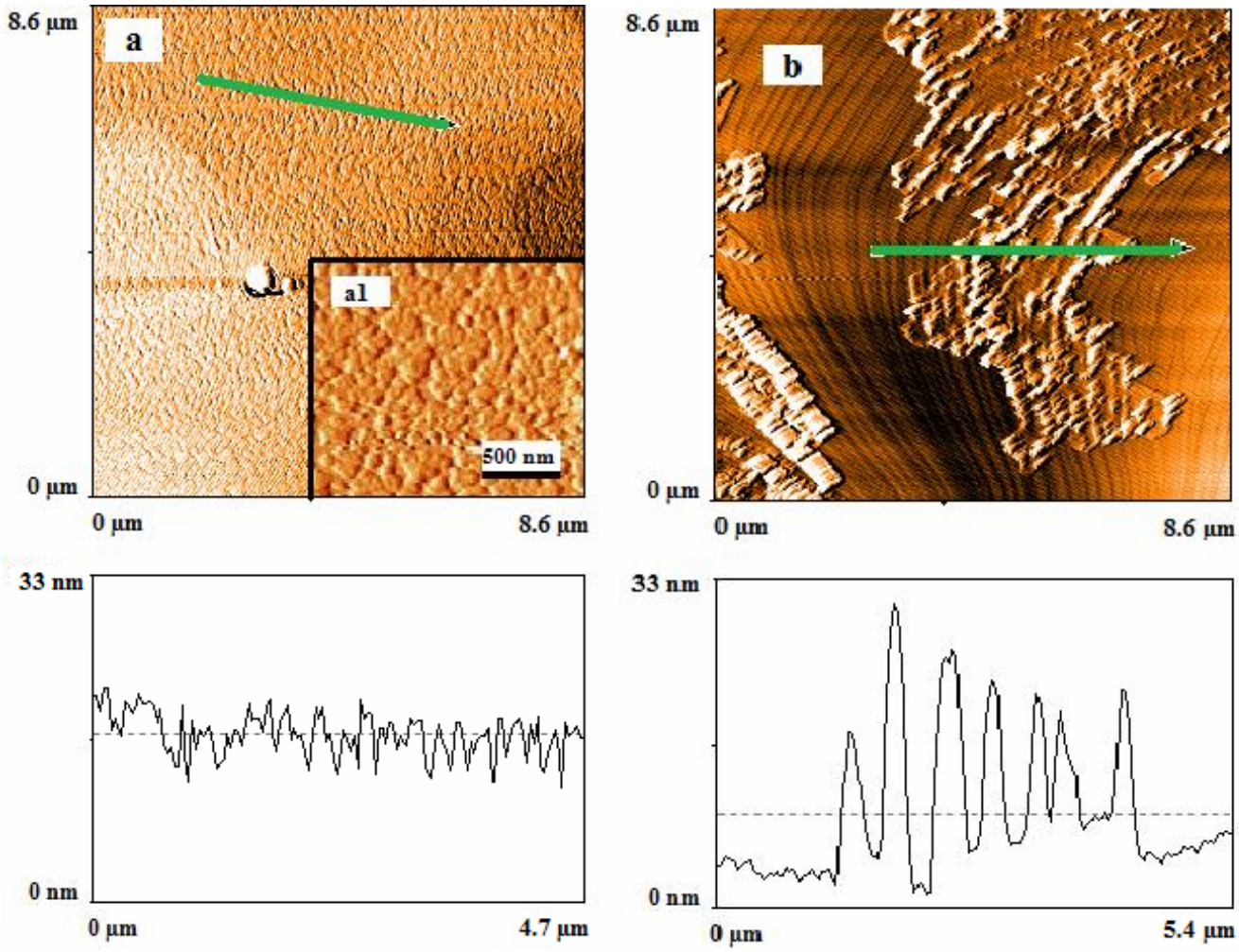

Fig. 7.11: a) AFM image in 'shaded mode' of HATCN films on Au (111) with a mean thickness of $16\ \text{Å}$, taken ex-situ at room temperature. Substrate temperature during HATCN adsorption: $300\ K$. The insert **a1)** shows an enlarged detail. The cross section is taken along the line depicted in the AFM image. **b)** AFM image in 'shaded mode' of HATCN films on Au (111) with a mean thickness of

$16\,\text{Å}$, taken ex-situ at room temperature. Substrate temperature during HATCN adsorption: $400\,K$. The cross section is taken along the line depicted in the AFM image.

A significant difference was observed for the film prepared at a substrate temperature of $400\,K$. The HATCN film shown in **Fig. 7.11b** consists of large islands of coalesced grains (typical size). A cross section reveals a mean height of the grains of about $10-20\,nm$. Thus the AFM images corroborate the results obtained by XPS.

The thermal stability of the film morphology was investigated in-situ by 'XPS vs temperature' measurements. For that purpose several films of different thickness were prepared at $200\,K$ and the substrate Au4f signal was followed during heating of the sample (**Fig. 7.12**).

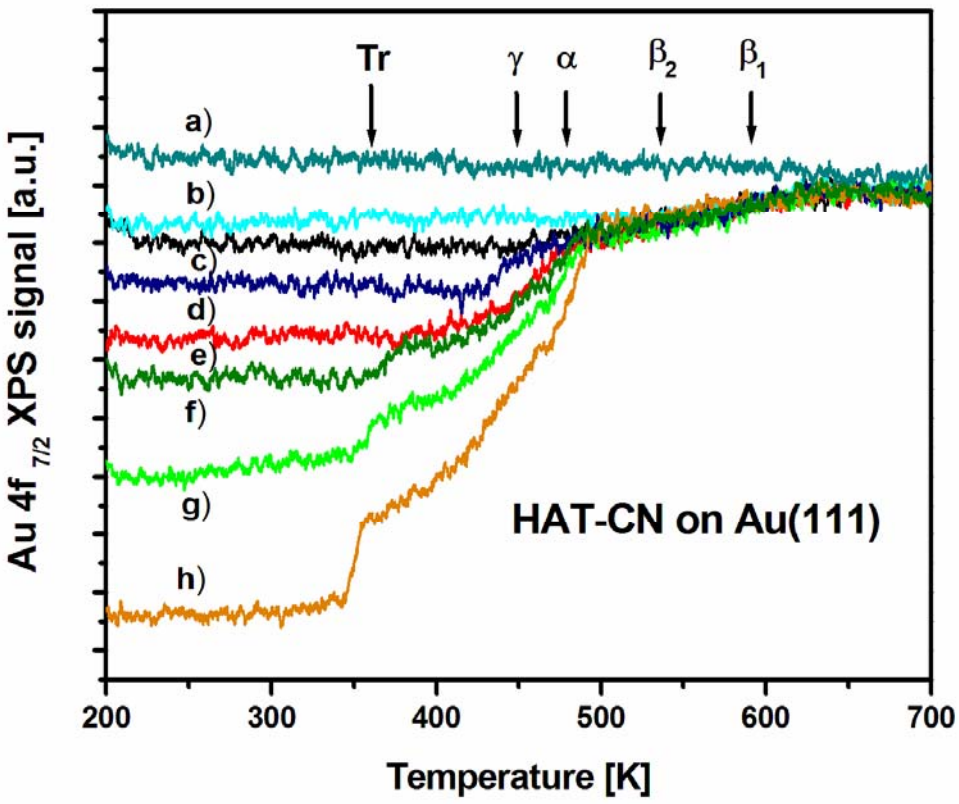

Fig. 7.12: XPS Au4f substrate signal change during heating of the sample, for various initial coverages of HATCN: **a)** $0\,\text{Å}$, **b)** $1.6\,\text{Å}$, **c)** $2.4\,\text{Å}$, **d)** $4\,\text{Å}$, **e)** $5.6\,\text{Å}$, **f)** $6.4\,\text{Å}$, **g)** $8\,\text{Å}$, **h)** $12\,\text{Å}$. Substrate temperature during film deposition: $200\,K$, heating rate $1\frac{K}{s}$. The peak maxima of the corresponding desorption peaks are indicated.

Curve **a)** in **Fig. 7.12** shows the XPS signal change vs. temperature without a film, indicating the signal attenuation due to the Debye-Waller effect and other experimental reasons. For initial HATCN coverages of $1.6\,\text{Å}$ and $2.4\,\text{Å}$ the Au4f substrate signal intensity does not change during sample heating between $200\,K$ and $500\,K$, but then starts to increase corresponding to the desorption from the β states (see **Fig. 7.4**). For the $4\,\text{Å}$ film the sharp signal increase around $450\,K$ corresponds to the desorption from the γ state, followed by the signal change between $500\,K$ and $600\,K$ due to desorption from the β states. At higher initial coverages ($> 8\,\text{Å}$), the Au4f signal intensity exhibits a first sharp increase already in the range of $350\,K$ to $380\,K$, signified by Tr. The further signal change up to $500\,K$ correlates with the desorption of the multilayer (α peak in **Fig. 7.4** & **7.6**). The low-temperature Au4f intensity increase is, however, not correlated with any desorption (see **Fig. 7.4** & **7.6**). This indicates that a morphological transition (Tr) from a layer-like film to 3D islands occurs in the range of $350\,K$ to $380\,K$. The Tr onset temperature slightly decreases with increasing coverage. It is proposed that at this transition temperature the integration of the molecules that are lying in first two layers (β- and γ-state) into the 3-dimensional bulk structure (α state) takes place. The driving force for the transition is presumably that according to Szalay et al. [58, 59] the HATCN molecules avoid π-stacking (parallel alignment). The crystal packing of HATCN is instead dominated by perpendicular CN-π interactions (T-stacking). Therefore, small amounts of molecules in the 3rd layer could act as nucleation centers for the formation of 3-dimensional islands which already exhibit the bulk crystal structure.

7.5 The bulk phase (3D-islands)

In order to verify the previous findings and the proposed growth model, the bulk structure had to be examined. This was done by XRD measurements. For this purpose, thicker films ($> 200\,\text{Å}$) were prepared. It is to mention that the characteristics of the films shown previously in **Fig. 7.11** do not change significantly upon adsorption of additional material. AFM images of much thicker films ($240\,\text{Å}$), prepared at RT and at $400\,K$, are shown in **Fig. 7.13** & **Fig. 7.14**.

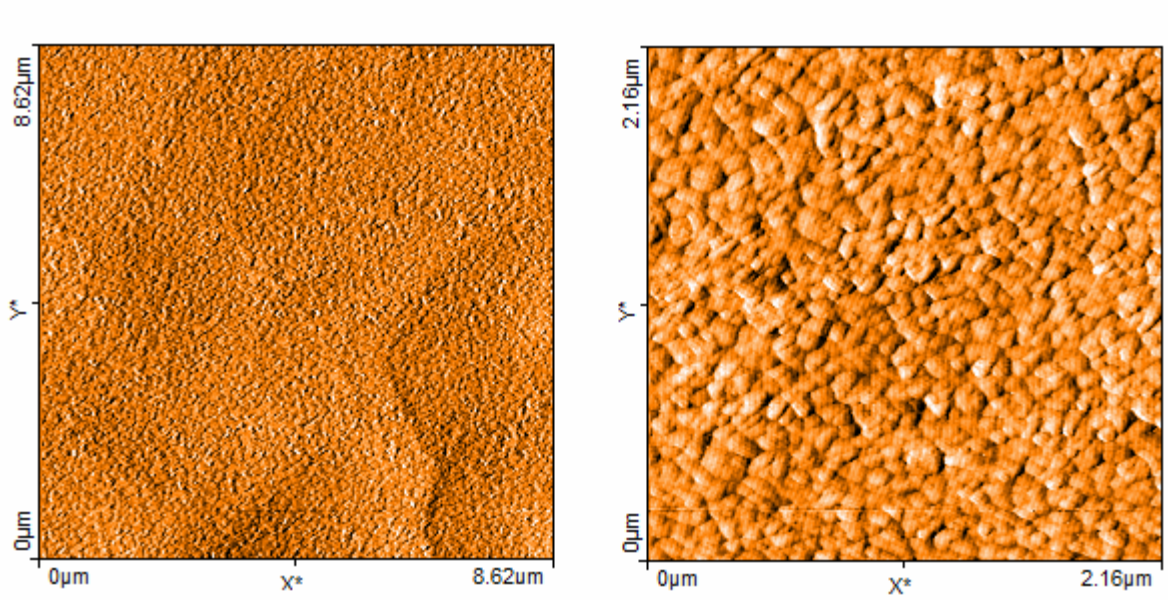

Fig. 7.13: AFM images in 'shaded mode' of HATCN films on Au (111) with a mean thickness of $24\ nm$, taken ex-situ at room temperature. Substrate temperature during HATCN adsorption: $300\ K$. Z-Scale: **left:** $40\ nm$, **right:** $20\ nm$. The right image is a detail view taken from the center of the left image.

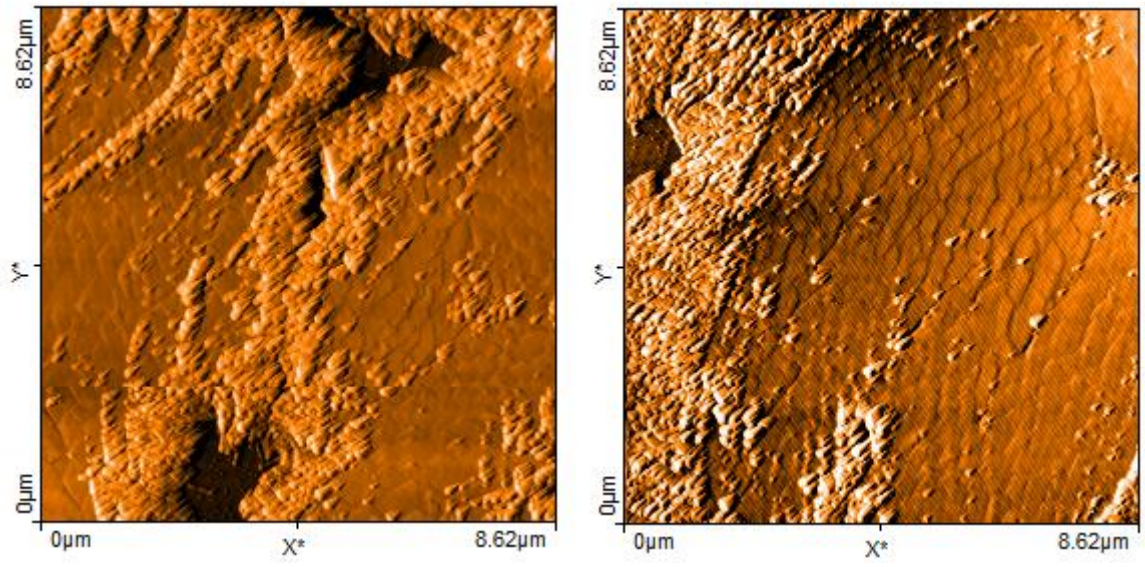

Fig. 7.14: AFM images in 'shaded mode' of a HATCN film at different positions on the Au (111) surface with a mean thickness of $24\ nm$, taken ex-situ at room temperature. Substrate temperature during HATCN adsorption: $400\ K$. Z-Scale of both images: $85\ nm$.

X-ray pole figure measurements which were performed at a $40\ nm$ thick film grown at $400\ K$ show that this film is composed of small crystallites, which exhibit a structure corresponding to the bulk structure of HATCN (see section **3.2, Fig. 3.3**): The molecules crystallize in a hexagonal symmetry with 18 molecules per unit cell resulting in a complex three-dimensional network formed by T-stacking of neighboring molecules. No significant line broadening of the diffraction peaks is observed which reveals the strong tendency of HATCN for crystallization with crystallite sizes of at least $100\ nm$. From the pole figure measurements (**Fig. 7.15**) a preferential orientation of the crystallites with the (143) orientation (**Fig. 7.16**) parallel to the substrate surface, but with random azimuthal orientation is obtained. In the (143) orientation one third of the molecules is orientated parallel (flat-on) to the substrate. The residual molecules are oriented perpendicular to the flat-on molecules and in turn perpendicular with respect to each other. In all three molecular conformations the molecules which are parallel to each other are stepwise offset with respect to each other.

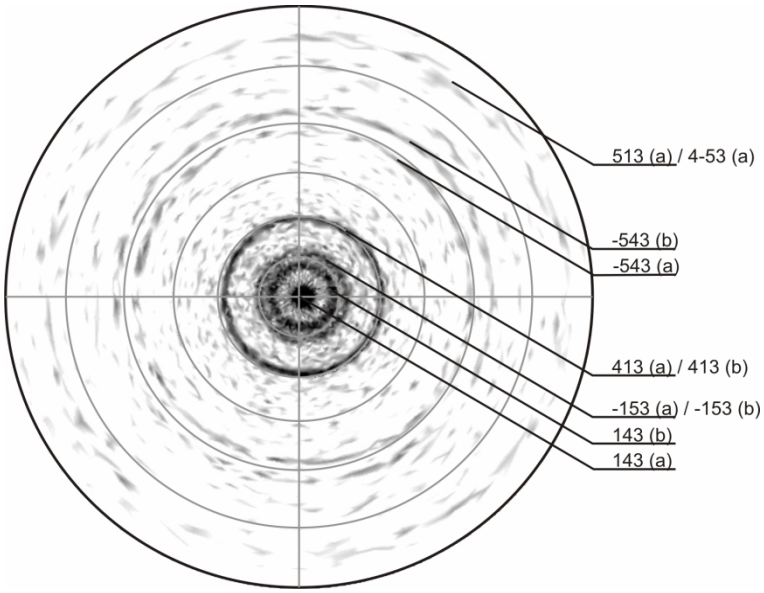

Fig. 7.15: X-ray pole figure of HATCN measured at a $\frac{\theta}{2\theta}$ angle of 40° to detect the 143 diffraction peaks. The strong intensity at the polar angle of 0° shows that the crystallites are aligned with their (143) plane parallel to the surface. Note that for this hexagonal system Miller-Bravais indices $(h\,k\,i\,l)$ can be used with $h = 1, k = 4, i = -5$ and $l = 3$. A permutation of the indices $h\,k\,i$ yields equivalent planes. The ring structures at 15° and 30° stem from diffraction of the equivalent planes (-153) and (413) of the hexagonal structure, indicating that no preferred azimuthal alignment of the crystallites exists.

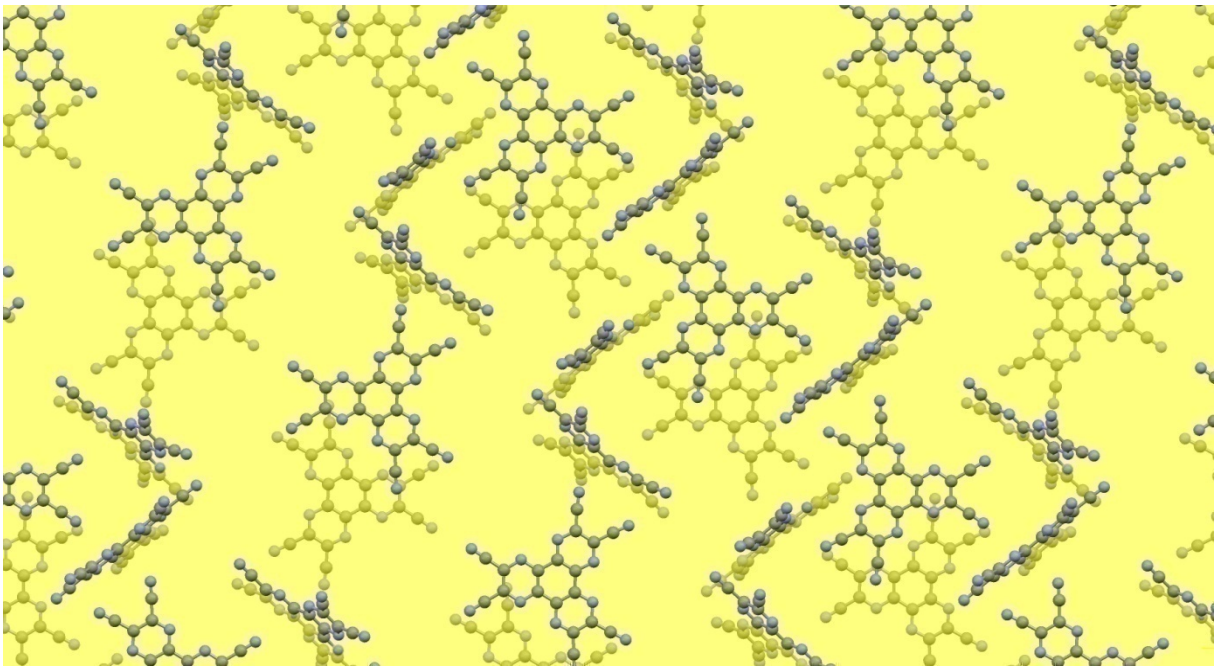

Fig. 7.16: Top view of the HATCN (143) plane. The dark yellow molecules are parallel to the flat-on blue/grey molecules, but significantly offset. Neighboring molecules prefer perpendicular arrangement with respect to each other (T-stacking).

7.6 Work function modification of Au (111) by HATCN

The work function of the Au (111) surface can be modified by HATCN adsorption. When performing work function measurements using the Kelvin probe, it is of uttermost importance to maintain a low base pressure in order to prohibit water adsorption on the surface during the measurement. The work function was measured as a function of the film thickness. However, the reproducibility of these measurements on Au (111) was rather unsatisfying, in contrast to those on Ag (111) (see section **8.4**). In **Fig. 7.17**, two representative measurements are shown. The red curve shows the results of a measurement which was performed in September ’08, when the base pressure was rather high, and the black curve shows a measurement, which was done in February ’09, directly after a bake-out of the chamber and therefore at a lower base pressure. The substrate temperature was in both cases $300\,K$. Unfortunately, the work function could not be measured at other temperatures very well, because the sample was heated by resistive heating, which influences the work function.

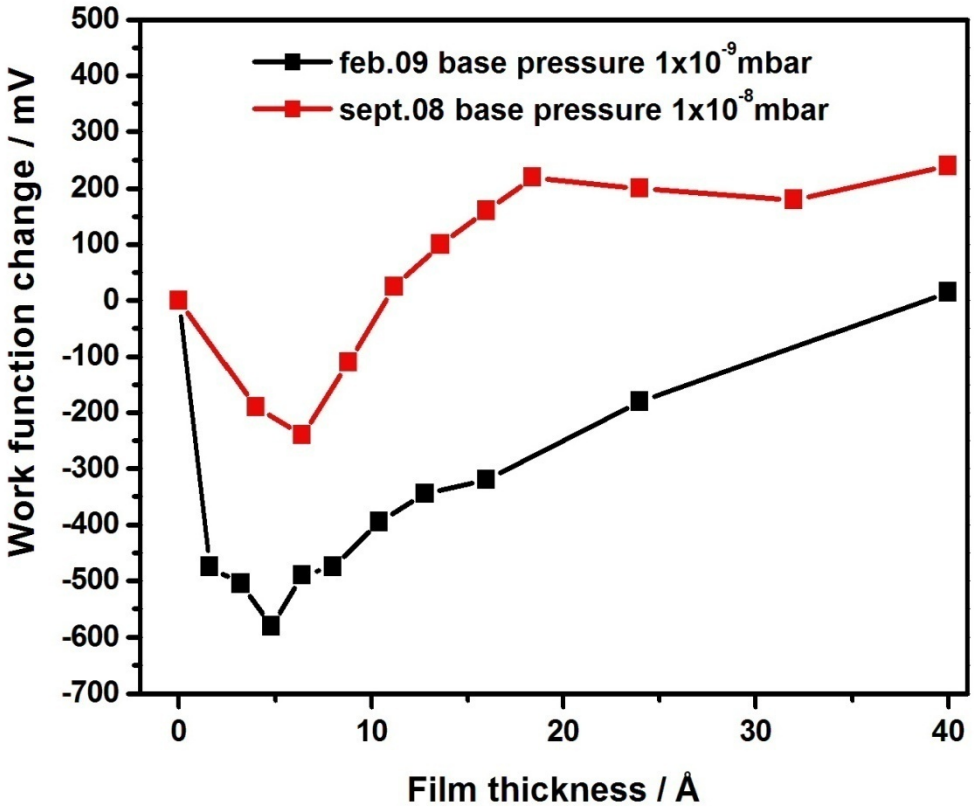

Fig. 7.17: Work function against film thickness. Y = 0 corresponds to the WF of clean Au (111). The results of two different measurements performed at different base pressures are shown. Substrate temperature $T_{ads} = 300\ K$.

They differ quantitatively from each other, but nevertheless, there exists a certain qualitative similarity. Up to a coverage of $5.6\ \text{Å}$, the work function decreases. Interestingly, the minimum of the curve, which is located at a film thickness of approximately $6\ \text{Å}$ for both measurements, coincides roughly with the disappearance of the γ peak in **Fig. 7.4** and **Fig. 7.12**. For thicker films, the work function increases with increasing film thickness. A possible explanation for the decrease of the work function for thin films $< 6\ \text{Å}$ might be the formation of a film consisting of molecules lying flat on the surface, whereas the increase of the work function could be attributed to the formation of the alpha phase and the integration of formerly lying molecules into this multilayer phase. A more detailed discussion about the work function change due to HATCN in general can be found in section **8.4**, where the work function change of an Ag (111) single crystal is investigated. Thus, the presented work function measurements would agree with the TD-spectra shown in **Fig. 7.4** and **Fig. 7.6**. The reason for the bad reproducibility of the work function change could be explained by the dynamic process of the rearrangement of the first layer. The films could be influenced by the

time passing by during film preparation (linked to the deposition rate) and the time passing by between the preparation of the films and the work function measurements. Hence the waiting time at room temperature would influence the structure of the film, especially the structure of the very mobile first layer which has the strongest impact on the work function.

7.7 HATCN on CN-contaminated Au

Although no dissociation of HATCN on Au (111) was observed, it was noticed that after several TD experiments the characteristics of the obtained spectra changed, if the substrate was not sputtered after each TD-spectrum. Obviously the amount of dissociated molecules which remain on the surface during heating up to $900\ K$ is very small and it needs several cycles of adsorption and subsequent heating until a noteworthy contamination appears. In order to investigate the influence of contaminants on the film growth, a saturation layer was prepared by X-ray induced dissociation, analog to the preparation of C-mica, which is described in the related section (**5.5 p6P on carbon contaminated mica (001)**). In order to create a uniform and homogeneous layer, a thick film of HATCN was prepared at a low temperature. This film was irradiated with Mg Kα X-radiation for several hours and subsequently the substrate was heated to get rid of non-dissociated molecules by thermal desorption. This procedure was repeated until a saturation coverage was reached. This coverage was checked by XPS (**Fig. 7.18**) and AES (**Fig. 7.19**).

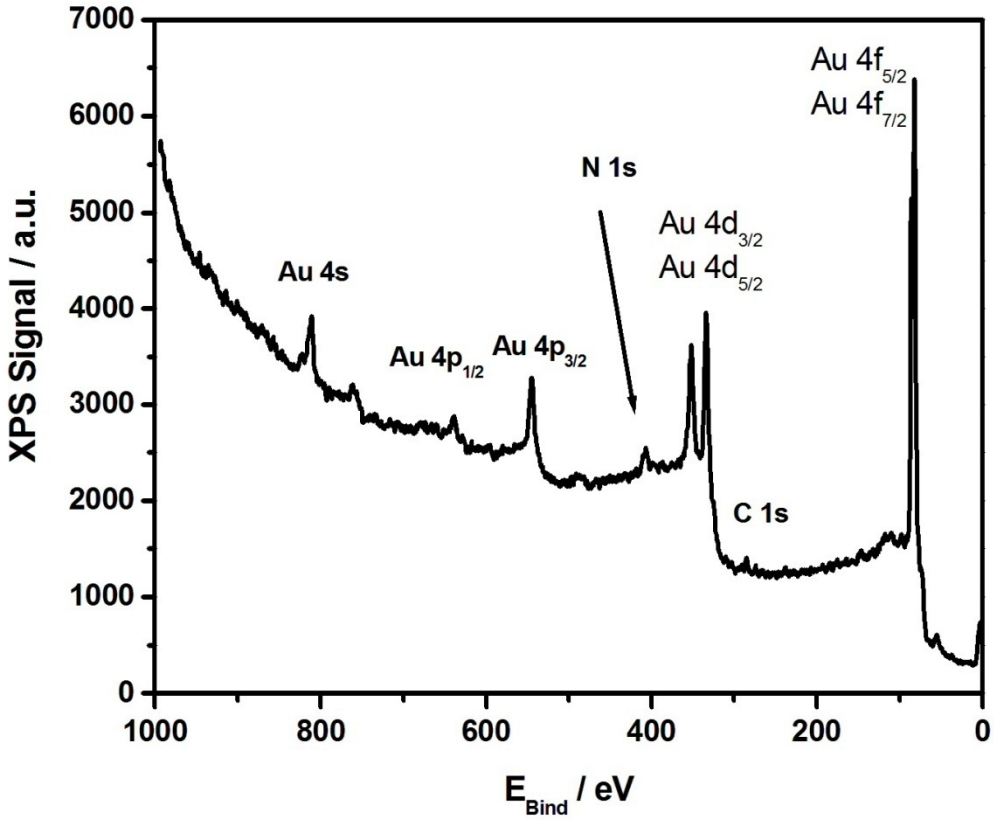

Fig. 7.18: XP-spectrum of Au + saturation layer of carbon and nitrogen (Au + CN), as obtained by X-ray induced dissociation of HATCN.

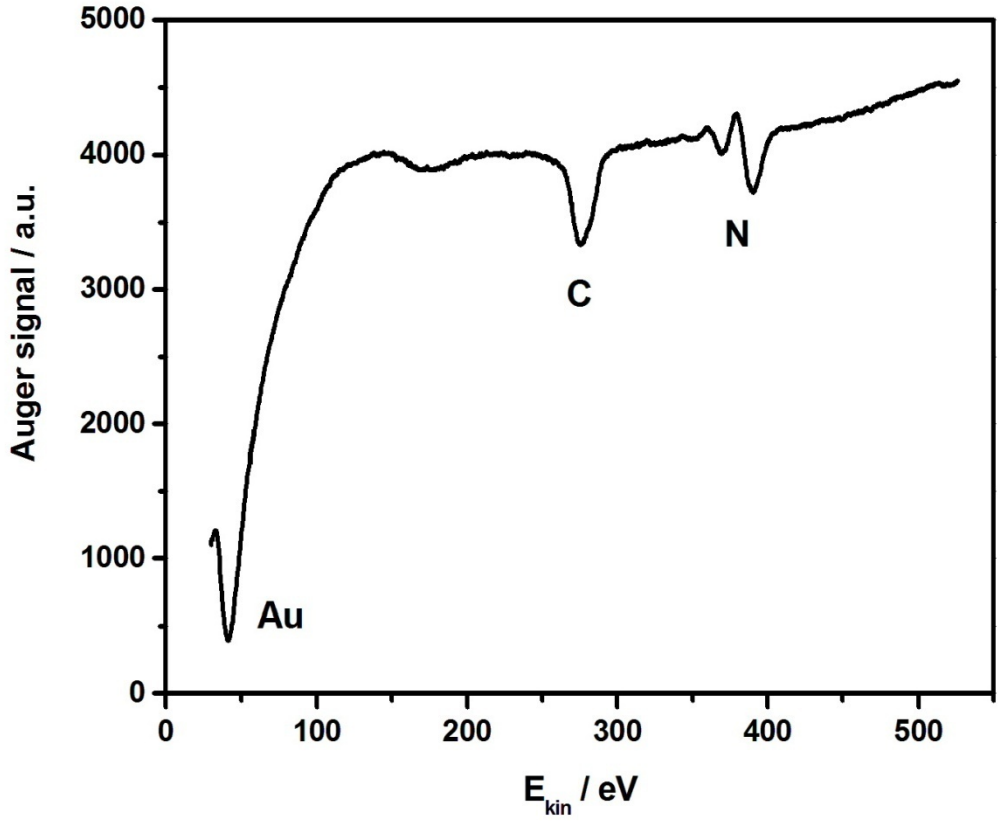

Fig. 7.19: AE-spectrum of Au + saturation layer of carbon and nitrogen (Au + CN), as obtained by X-ray induced dissociation of HATCN. This spectrum was obtained from the same surface as the XP-spectrum shown in **Fig. 7.18**.

Comparing **Fig. 7.18** and **Fig. 7.19**, it is remarkable that the contamination layer, which naturally consists of carbon and nitrogen, can be seen clearly only in AES, while for instance the carbon peak in the XP spectrum is hardly visible. Therefore XPS is not well suited to specify the cleanliness of the surface in this case.

This saturation layer of carbon and nitrogen leads to a considerable change in film growth, as can be seen in a TD-spectrum (**Fig. 7.20**). Again, the TD-spectra do not depend on the adsorption temperature. The presented spectrum was obtained from a film which was prepared at $200\,K$. Quantitatively equivalent spectra were obtained for adsorption temperatures up to $400\,K$.

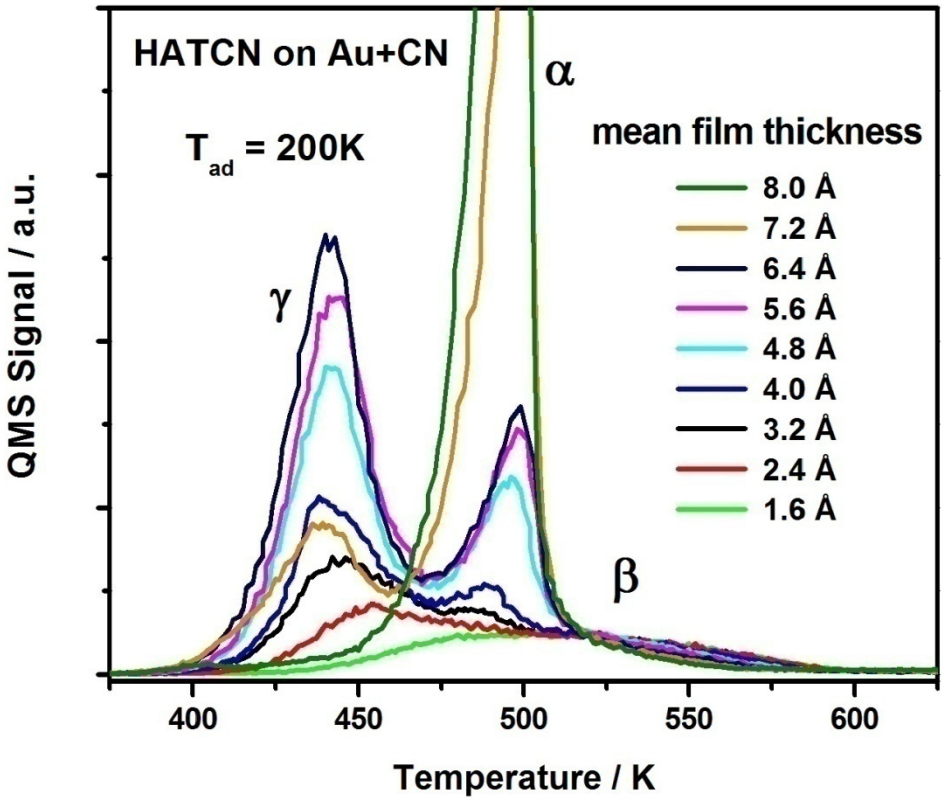

Fig. 7.20: Series of thermal desorption spectra of HATCN on Au + CN as a function of coverage. Adsorption temperature: $200\ K$, heating rate $1\frac{K}{s}$.

For initial coverages a small peak (β) arises which saturates already at $1.6\ Å$ or even below. With increasing mean film thickness the γ peak is formed, which is accompanied by the formation of the multilayer peak (α). The maximum of the γ peak shifts to lower temperatures which can be explained by repulsive interactions. The γ peak reaches its highest intensity at a coverage of $6.4\ Å$, which apparently corresponds to a critical film thickness since upon further adsorption suddenly the molecules from the γ phase shade off into the bulk phase. At a coverage of $8\ Å$, the γ peak has already completely disappeared. A comparable behavior is shown by the β peak, which can be discovered in a detailed view of this spectrum (**Fig. 7.21**).

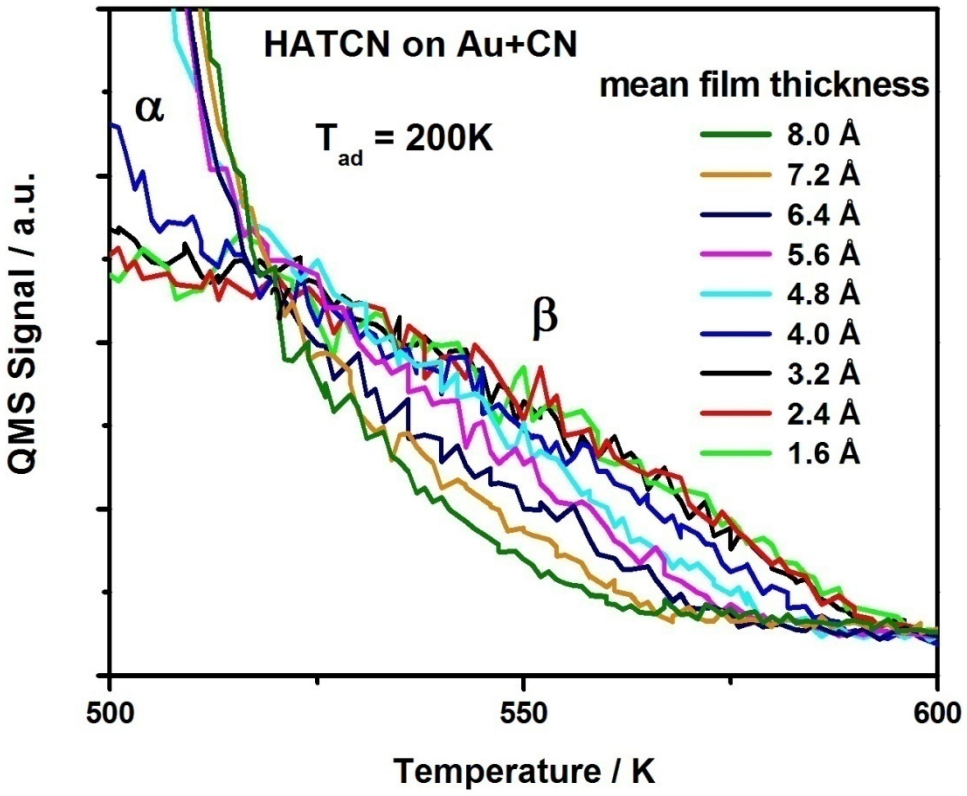

Fig. 7.21: Detail of **Fig. 7.20**. The β peak decreases steadily with increasing film thickness.

In **Fig. 7.22**, the amount of molecules in the separate adsorption states is plotted as a function of the nominal mean film thickness.

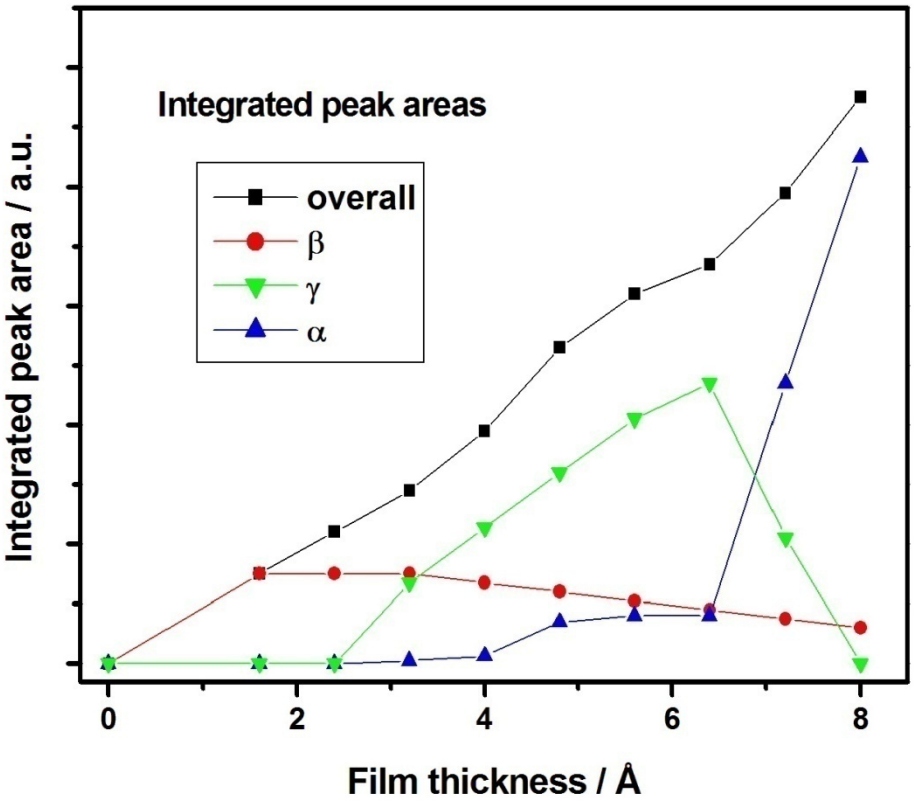

Fig. 7.22: Integrals of the separated TDS peaks and their sum from measurements such as in **Fig. 7.20** as a function of mean film thickness. Heating rate $\frac{dT}{dt} = 1\frac{K}{s}$ in all cases.

In order to explain the film growth on the modified Au surface, the TD-spectra shown in this section have to be compared to the TD-spectra on the clean Au surface (**Fig. 7.4** & **Fig. 7.6**). On the clean surface first two layers of flat lying molecules are formed, which later on get integrated into the bulk phase with increasing film thickness. Keeping in mind this growth model, the TDS data presented in this section can be explained as follows. The very small β peak, which ranges from $\approx 450\ K$ up to $575\ K$, saturates even below $1.6\ \text{Å}$. This peak contains much less molecules than the β peak on the clean surface, where one monolayer of lying molecules corresponds to a mean thickness of $2.4\ \text{Å}$. The range of the desorption temperature of this peak is significantly lower than the one of the monolayer peak on the clean Au surface which indicates either a reduced binding energy or a reduced mobility (higher pre-exponential factor) on the CN-modified surface. Unfortunately, the definite morphology of the CN saturation layer is unknown. It is assumed that upon dissociation the remnants of the HATCN molecules form densely packed and uniformly distributed flat

islands consisting of carbon and nitrogen. Thus a possible explanation for the lower desorption temperature is that either the binding energy of these molecules is reduced compared to the clean Au surface, or that the molecules are immobilized by the roughness of the surface. As seen in **Fig. 7.21**, the destabilization of this layer starts earlier (at ≈ 4 Å) than on the clean Au surface (at ≈ 5.6 Å). It is assumed that the reason for the decrease of the β peak is in both cases the same, namely the integration of molecules into the multilayer and that this integration starts as soon as the multilayer phase exists. Hence the earlier destabilization of the β peak on the modified surface can be explained by the earlier formation of the bulk (α) phase, which begins at ≈ 4 Å (see **Fig. 7.20** and **Fig. 7.22**). The γ peak increases up to a film thickness of 6.4 Å and is most probably formed by molecules lying flat in the first and the second layer. In contrast to the clean surface, the γ and the α peak are separated more clearly. Hence the destabilization of the assumedly flat lying molecules in the γ peak and the subsequent integration of these molecules into the bulk structure (α) is seen more clearly in **Fig. 7.20** than in **Fig. 7.4** and **Fig. 7.6**. Monitoring the Au4f XPS signal during the heating of films of different film thickness yielded the spectrum shown in **Fig. 7.23**.

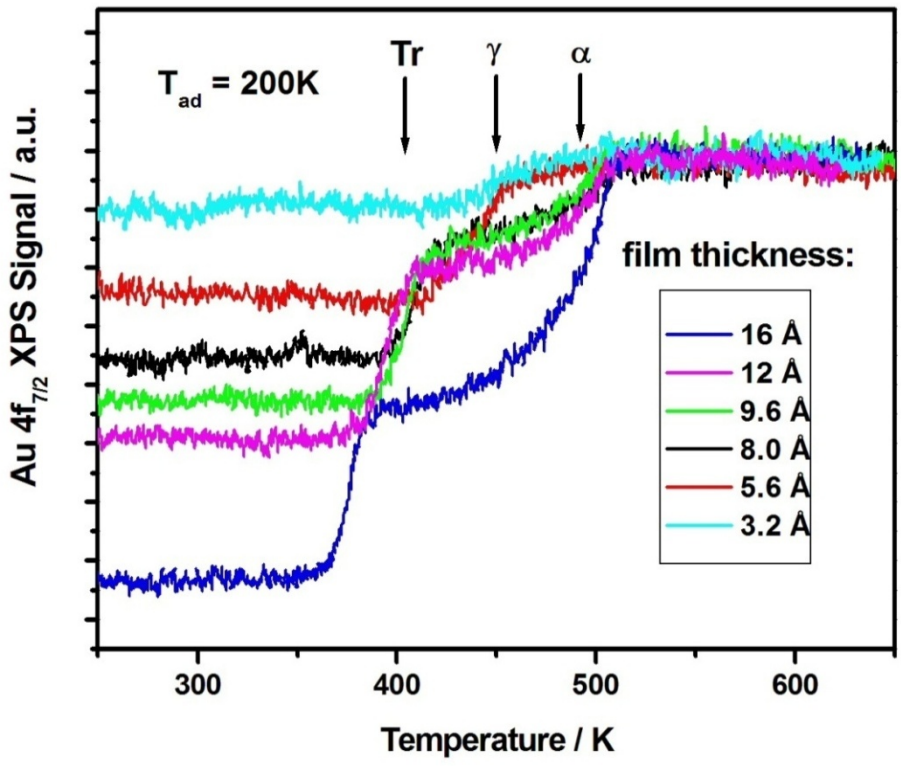

Fig. 7.23: XPS Au4f substrate signal change during heating of the Au + CN sample, for various initial coverages of HATCN. Substrate temperature during film deposition: $200\ K$, heating rate $1\frac{K}{s}$. The peak maxima of the corresponding desorption peaks are indicated.

This spectrum is very similar to the one shown in **Fig. 7.12** from the clean Au substrate. In contrast to **Fig. 7.12**, the substrate signal change caused by the desorption of the first layer (β) is too small to be seen above $500\ K$. However, for the coverages of $3.2\ \text{Å}$ and $5.6\ \text{Å}$ there is a slight increase of the signal between $450\ K$ and $500\ K$, which can be correlated to the desorption from the first layer.

For the $5.6\ \text{Å}$ film the sharp signal increase around $450\ K$ corresponds to the desorption from the γ state. At higher initial coverages ($\geq 8\ \text{Å}$), the Au4f signal intensity exhibits a first sharp increase already in the range of $370\ K$ to $400\ K$, signified by Tr. The further signal change up to $500\ K$ correlates with the desorption of the multilayer (α peak in **Fig. 7.20**). Just like on the clean surface, this low-temperature Au4f intensity increase is not correlated with any desorption (see **Fig. 7.20**) on the CN-modified surface. This indicates that a morphological transition (Tr) from a layer-like film to 3D islands occurs in the range of $370\ K$ to $400\ K$. The Tr onset temperature slightly decreases with increasing coverage. It is proposed that at this transition temperature the integration of the molecules that are lying in first two layers (β- and γ-state) into the 3-dimensional bulk structure (α state) takes place like on the clean gold surface.

8 HATCN on Ag (111)

The growth of HATCN on Ag (111) is in the following subdivided into three regimes: Section **8.1** addresses the initial film growth (≤ 2.4 Å), section **8.2** the growth of intermediate films between 3 Å and 10 Å mean film thickness and section **8.3** the film growth beyond that thickness. The thickness of the films shown in this chapter is the nominal mean thickness that has been obtained by applying the density of the crystal structure ($\rho = 1.6 \frac{g}{cm^3}$, see **table 4.1**). Therefore in the monolayer regime this nominal mean film thickness does not correspond to the 'real' thickness of the films, but has to be seen as a measure for the amount of molecules on the surface.

8.1 Initial film growth: The lying monolayer

When films with a film thickness ≤ 2.4 Å are heated, no desorption of intact molecules and also no desorption of fragments is observed in the TD-spectra. This is a sign of a very strong bond between the substrate and the HATCN molecules. The LEED images in **Fig. 8.1** show that this monolayer is highly ordered and that the structure of the monolayer is a (7x7) superstructure.

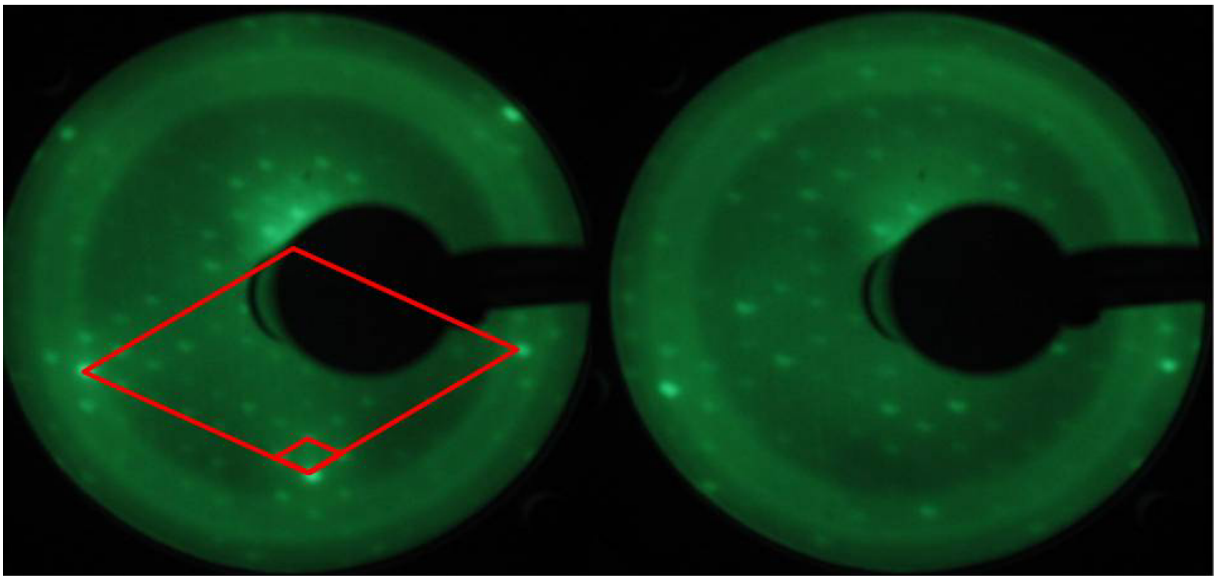

Fig. 8.1: LEED images of a $2.4\,\text{Å}$ thick HATCN film on Ag (111). The image on the left was taken at $113\,V$, the one on the right at $88\,V$. The images show the (7x7) superstructure of the HATCN monolayer on the hexagonal Ag (111) substrate. The respective unit cells are drawn in red.

The best images were obtained for the $2.4\,\text{Å}$ thick films, which corresponds to a molecular density of $6.0 \times 10^{13} \frac{molecules}{cm^2}$ according to the calibrated microbalance. With increasing film thickness the spots fade away and cannot be seen for films thicker than $4\,\text{Å}$. This observation could be an indicator of a rearrangement of the lying molecules in the (7x7) structure with ongoing HATCN deposition.

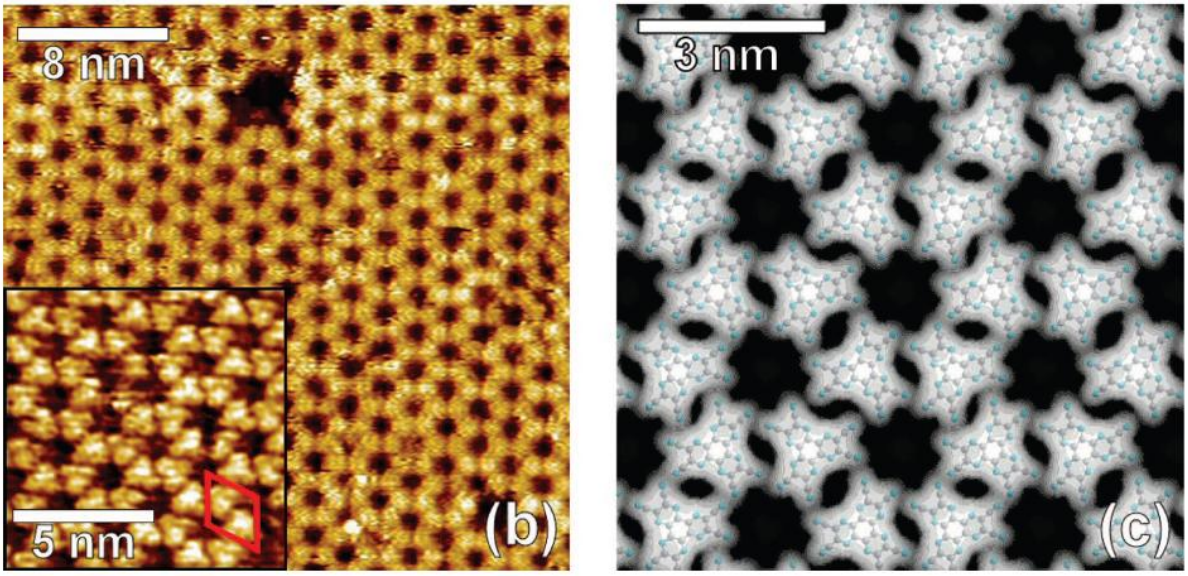

Fig. 8.2: STM images of the HATCN monolayer on Ag (111), taken from [126]. The image on the left shows the honeycomb structure of the lying molecules. The inset resolves individual molecules; the red rhombus indicates the hexagonal unit cell with $a = 2.0\,nm$. The image on the right shows a simulated STM image of a HATCN monolayer on Ag (111). The structures of the individual HATCN molecules are overlaid as a guide to the eye to be able to correlate the STM picture with the molecular arrangement.

STM measurements (**Fig. 8.2, left**) show that the monolayer of HATCN on Ag (111) forms a honeycomb structure, which is characterized by a hexagonal unit cell containing two molecules and a lattice parameter of $(2.0 \pm 0.1)nm$ [126]. The areal density of this structure can be estimated to be $5.8 \times 10^{13} \frac{molecules}{cm^2}$. In the inset individual molecules can be

discerned. The right hand side of **Fig. 8.2** shows a simulated STM image, which is in excellent agreement with the measured images. Six HATCN molecules form one closed ring-like feature, leaving a hole in its center. Together with the lattice constant of Ag (111) ($a = 2.89$ Å) one can demonstrate that this honeycomb structure is in accordance with the (7x7) superstructure seen in LEED:

$$a(HATCN) = 2.0\ nm \approx a(Ag) = 0.289\ nm \approx 7$$

8.2 Intermediate film growth: The standing monolayer

This section addresses the growth of films between a nominal thickness of 2.4 Å and 8 Å. These films show no desorption of intact molecules upon heating too, but in contrast to the films smaller than 2.4 Å, in the intermediate regime the desorption of $(CN)_2$ fragments is clearly seen (**Fig. 8.3**). The $(CN)_2$ desorption saturates at about 8 Å, which corresponds to an areal density of $2 \times 10^{14}\ \frac{molecules}{cm^2}$. From this TD-data it follows that there is an approximately 8 Å thick layer, which is bonded very strongly to the substrate because the molecules dissociate prior to any desorption.

A layer of standing molecules on a layer of lying molecules should be thicker, considering the diameter of a HATCN molecule to be $1.5\ nm$ and most probably such a layer would be a physisorbed one which then would desorb without dissociation at the surface. A layer of molecules standing in the holes of the honeycomb structure of the lying layer is ruled out since such a layer would comprise too few molecules (0.5 times the number of molecules in the lying monolayer, thus together with the lying monolayer at most a nominal thickness of 4 Å). Thus the most reasonable explanation for the desorption behavior of the HATCN fragments is that after the saturation of the lying monolayer the molecules tend to stand upright directly on the surface as the molecular density on the surface is increased. As a consequence, the CN groups which are in direct contact with the Ag (111) surface remain in this state even upon heating up to $900\ K$ while the residual CN groups separate from the molecules (probably the ones on the top of the standing layer) and desorb at elevated temperatures ($600\ K - 900\ K$). The driving force for this rearrangement of the lying monolayer into a standing monolayer is most probably a mixture of several mechanisms that

all favor standing molecules: First the HATCN molecules are known to avoid π-stacking [58, 59] (compare also chapter **5**), which argues against the formation of a layer of lying molecules growing on top of the lying monolayer. Additionally, DFT modeling [133] suggests that the molecules in the lying monolayer are distorted because the CN groups bend down towards the surface. In the standing monolayer the molecules are no longer distorted.

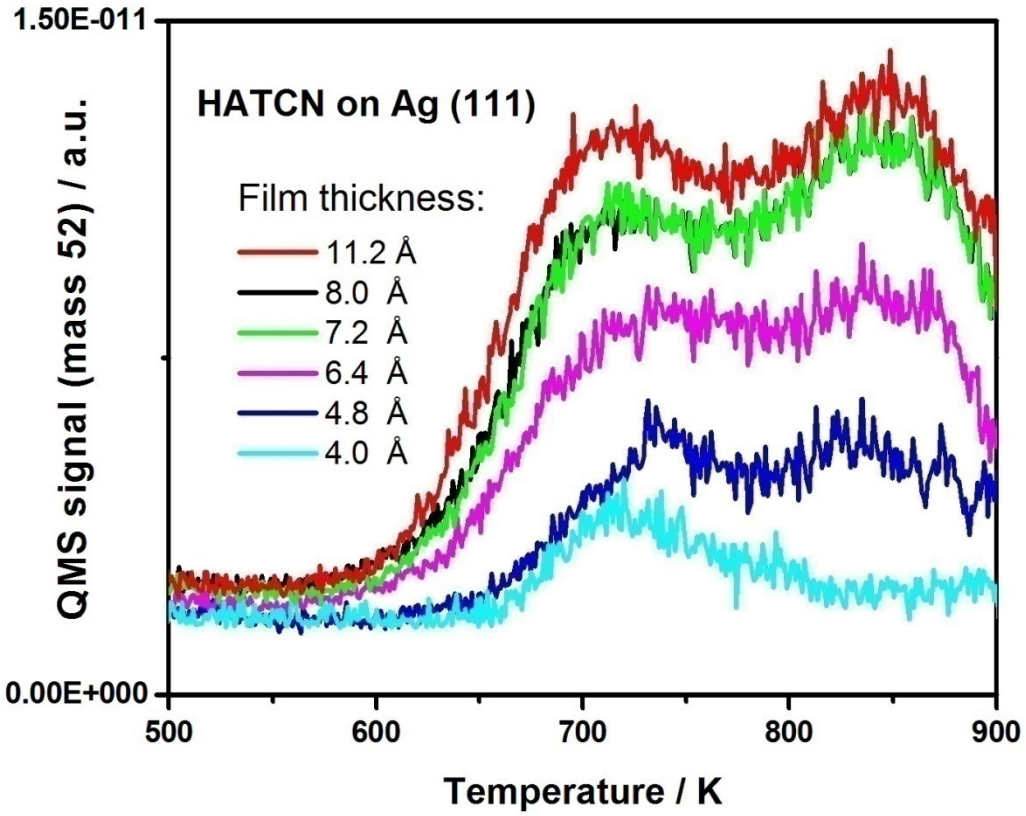

Fig. 8.3: TDS of HATCN on Ag (111). This figure shows the change of the mass 52 $(CN)_2$ signal. No increase of any of the masses related to the intact molecule was noticed up to $900\,K$.

The reason for the appearance of two distinct $(CN)_2$ peaks in the TDS is not clear yet. Obviously not all the CN groups, which are not in direct contact with the Ag (111) surface, separate from the molecule at the same temperature, which indicates a different binding strength to the molecule. A possible explanation for the two peaks could be that the CN groups next to the ones which are in direct contact with the Ag (111) surface exhibit a different binding strength to the molecule than the ones farther away.

8.3 The multilayer regime

After the desorption peak of the HATCN fragments has saturated the desorption of intact molecules starts to appear. For the sake of clarity the TDS series is split into two parts. **Fig. 8.4** shows a TDS series of the regime between $8.8\ \text{Å}$ and $13.6\ \text{Å}$. Two peaks can be seen, γ and α', which both increase nearly simultaneously with increasing film thickness. In this regime the γ peak is always higher than the α' peak. **Fig. 8.5** shows the further evolution of this TDS series. The films were prepared at room temperature and the heating rate was in all cases $1\frac{K}{s}$. Quantitatively similar spectra are obtained if the films are prepared at different adsorption temperatures $\leq 350\ K$.

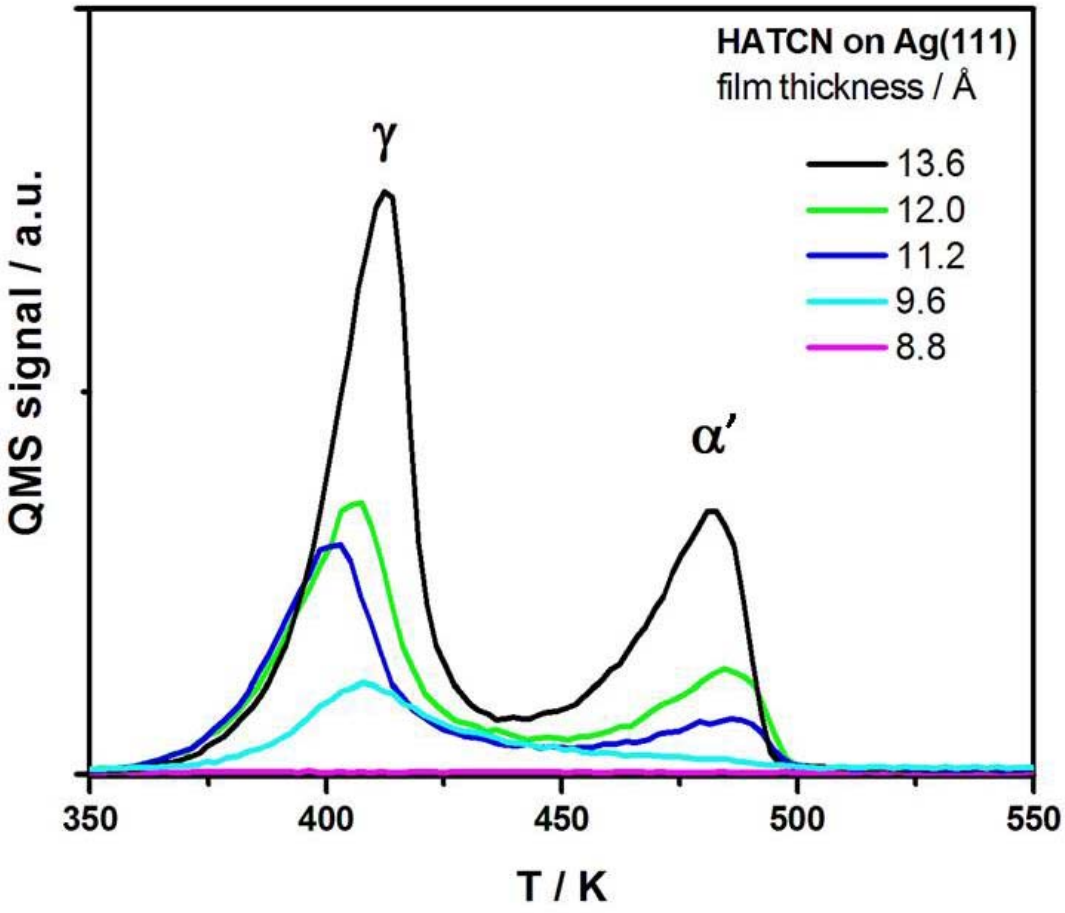

Fig. 8.4: TDS series of the beginning multilayer, $T_{ads} = 300\ K$. Up to a film thickness of $13.6\ \text{Å}$ the metastable γ peak shows a higher intensity than the α' peak.

Above a film thickness of ≈ 14 Å the γ peak and the α‘ peak start decreasing with increasing film thickness which leads to an excessive increase of the α peak, which stems from the multilayer. This finding is in detail illustrated in **Fig. 8.6**, where the integrated peak areas of **Fig. 8.4** and **Fig. 8.5** are plotted versus the film thickness. Starting at 8.8 Å , the total quantity (‘overall’) of desorbing molecules increases linearly with the coverage, which indicates a sticking coefficient of unity. In general, there is good reason to assume a sticking coefficient of unity for condensable molecules. However, the increase of the integrated peak area of the α peak in the range between 8.8 Å and 16 Å can be regarded as an almost exponential one, which is together with the decrease of the γ peak an apparent sign that an incorporation of molecules from one adsorption state (γ) into another adsorption state (α) is taking place. Similar to the growth on gold, also on silver a metastable phase exists which gets incorporated into the bulk phase as the film thickness is increased beyond a certain critical film thickness. In fact the spectra shown in **Fig. 8.4** and **Fig. 8.5** resemble the TD-spectra obtained on the CN-contaminated Au (111) surface: in both cases no high-temperature monolayer peak can be seen and the γ-peaks are clearly separated from the multilayer α-peak.

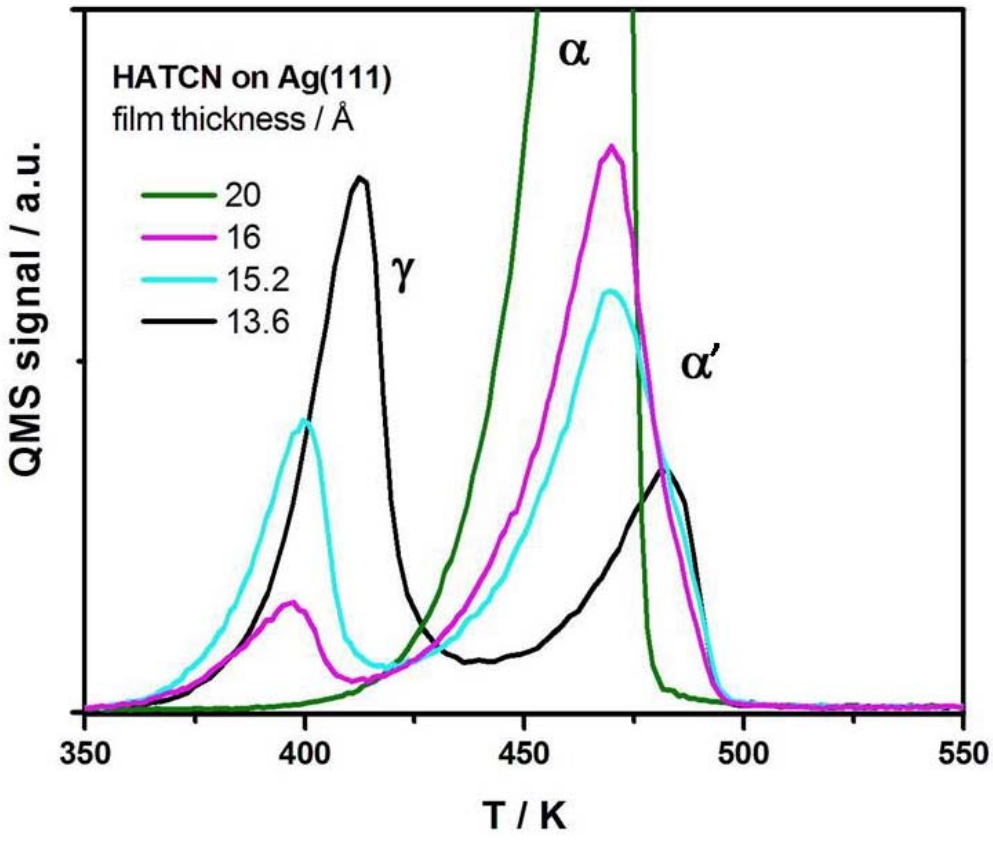

Fig. 8.5: TDS series of the ‘true’ multilayer regime, $T_{ads} = 300\ K$. The black curve in this image is the same as in **Fig. 8.4**. The metastable γ peak decreases with increasing film thickness, similar to the

γ peak on Au (see **Fig. 7.6**) and on CN-covered Au (**Fig. 7.20**). To the same degree the multilayer (α) peak increases in this regime.

The desorption temperature of the multilayer on Ag (111) is assumed to be the same as on Au (111). In fact, the onset of the multilayer desorption in **Fig. 7.6** is at $\approx 430\ K$, whereas the onset of the α peak in **Fig. 8.5** is at $\approx 400\ K$. This deviation can be explained by the different mounting of the thermocouple to the respective single crystals. On Au (111) the Ni/NiCr thermocouple was spot-welded directly onto the gold. The purchased silver single crystal featured a small hole on the back side where the thermocouple could be squeezed in. Obviously the thermal contact was poorer in the latter case, which led to a delay of the measured temperature during heating.

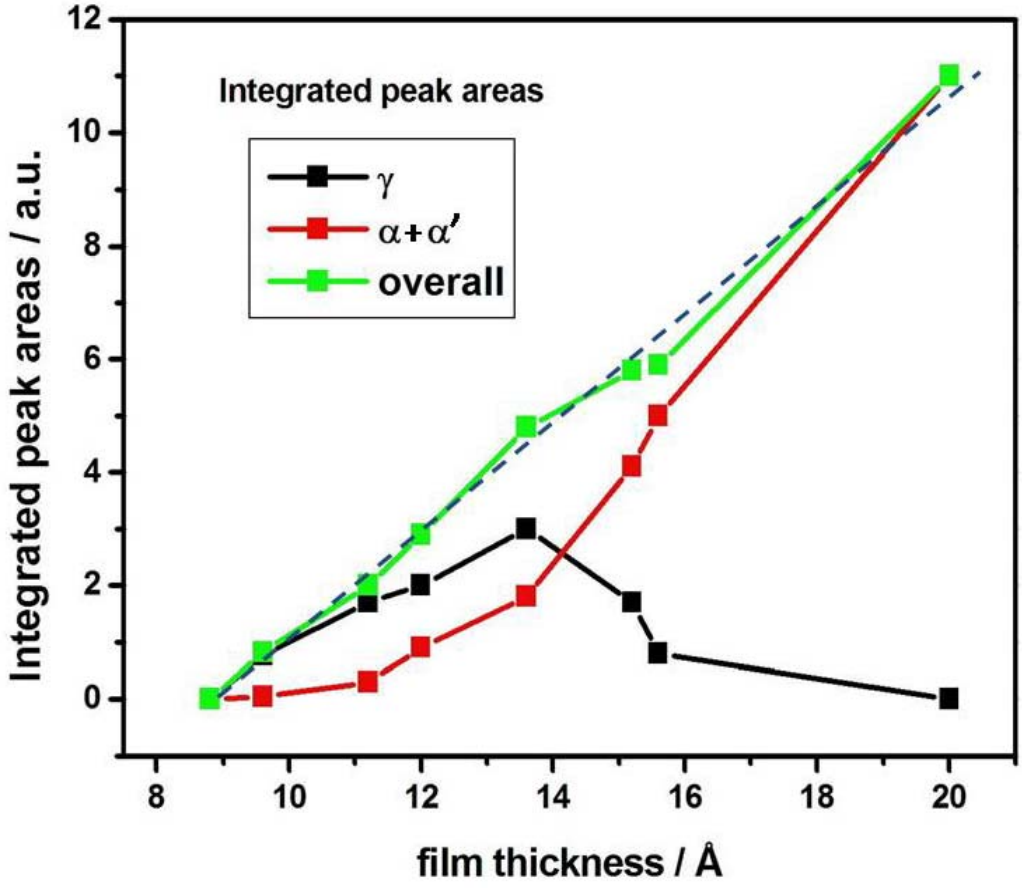

Fig. 8.6: Integrated peak areas from **Fig. 8.4** and **Fig. 8.5** as a function of the mean film thickness (adsorbed amount vs. desorbed amount). The dashed blue line is a linear fit of the integrated overall peak area.

The thermal stability of the film morphology was investigated in-situ by 'XPS vs temperature' measurements. For that purpose several films of different thickness were prepared at $200\ K$

and the substrate Ag3d signal was followed during heating of the sample (**Fig. 8.7**). The signal of the clean substrate features a slight decrease due to the Debye-Waller effect and other experimental reasons, which will not be discussed here. The $8\ \text{Å}$ thick film is stable up to $700\ K$. Above $700\ K$ the substrate signal increases, which fits to the desorption of $(CN)_2$ in this range. According to the desorption characteristics discussed in section **8.2**, the increase of the signal is caused by the desorption of the HATCN fragments on top of the standing layer, i.e. the outermost parts of the HATCN molecules in the monolayer. In agreement with **Fig. 8.3**, the signal increase induced by the desorption of HATCN fragments is already saturated at $8\ \text{Å}$. There is no significant signal change between $200\ K$ and $700\ K$. This can be explained in two ways: either the standing layer forms already below $200\ K$ or the rearrangement of approximately three layers of lying molecules into one layer of standing molecules taking possibly place somewhere between $200\ K$ and $700\ K$ cannot be seen because in either way the attenuation of the signal would be the same. As the film thickness is increased up to $13.6\ \text{Å}$ strong signal changes can be seen. In total agreement with the TD-spectra presented above (**Fig. 8.4** and **Fig. 8.5**), the substrate signal increases at $400\ K$ due to the desorption of the γ peak and around $480\ K$ due to the desorption of the α' peak.

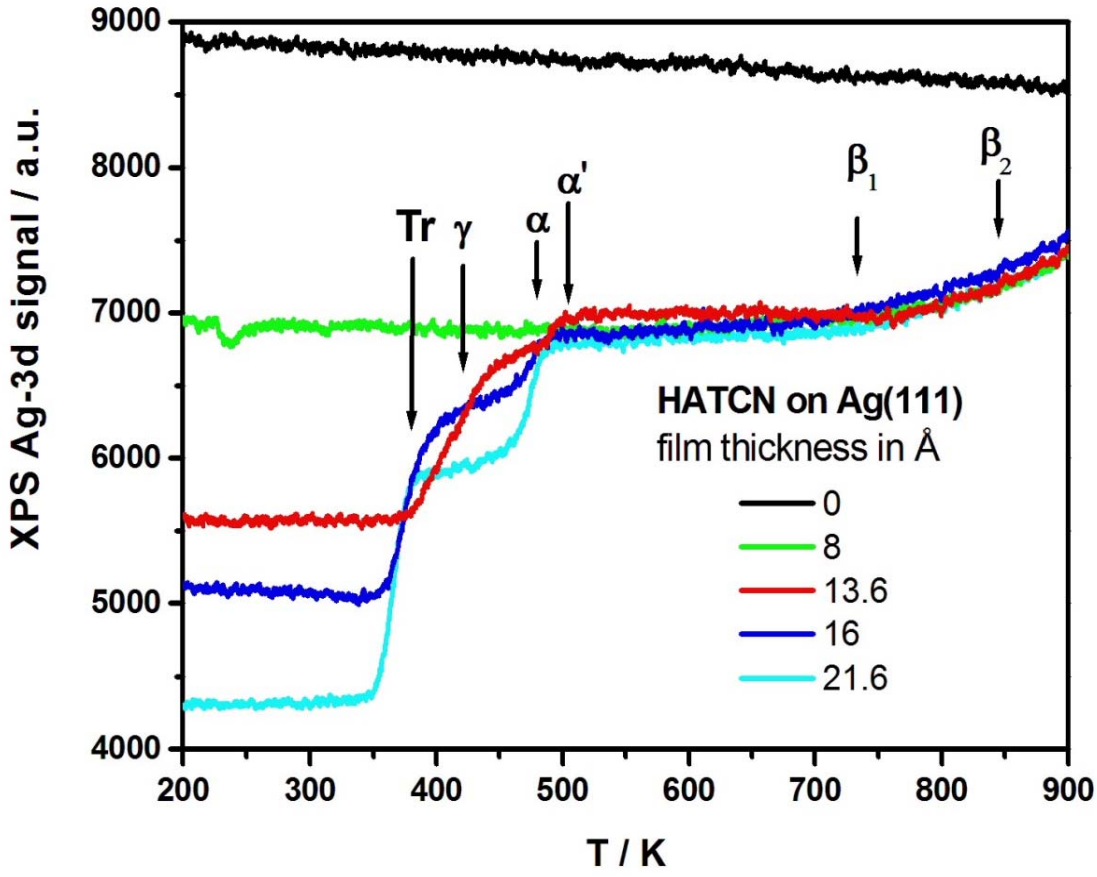

Fig. 8.7: XPS Ag3d substrate signal change during heating of the sample, for various initial coverages of HATCN. Films were prepared at $200\ K$ and the heating rate was $1\frac{K}{s}$. The peak maxima of the corresponding desorption peaks are indicated.

A new feature (at least for the Ag substrate) is seen as the film thickness is raised to $16\ Å$ and above. The substrate signal intensity rises already before the desorption starts, demonstrating a morphological rearrangement from a continuous layer-by-layer like film into an island like film around $350\ K$, which is definitely an expected behavior of HATCN multilayers (see chapter **7**). This rearrangement is only seen above a critical film thickness of $\approx 14\ Å$. Films which have undergone this rearrangement feature no XPS substrate signal increase around $400\ K$ and no (or only a very small) γ desorption peak in the TDS. These observations allow the conclusion that the γ peak stems from a film which grows in a layer-like fashion (wetting layer) and that the α peak stems from an island like film and that the incorporation of molecules into the α state takes place around $350\ K$. This idea is corroborated by AFM images of films prepared at $300\ K$ and at $400\ K$ (**Fig. 8.8**):

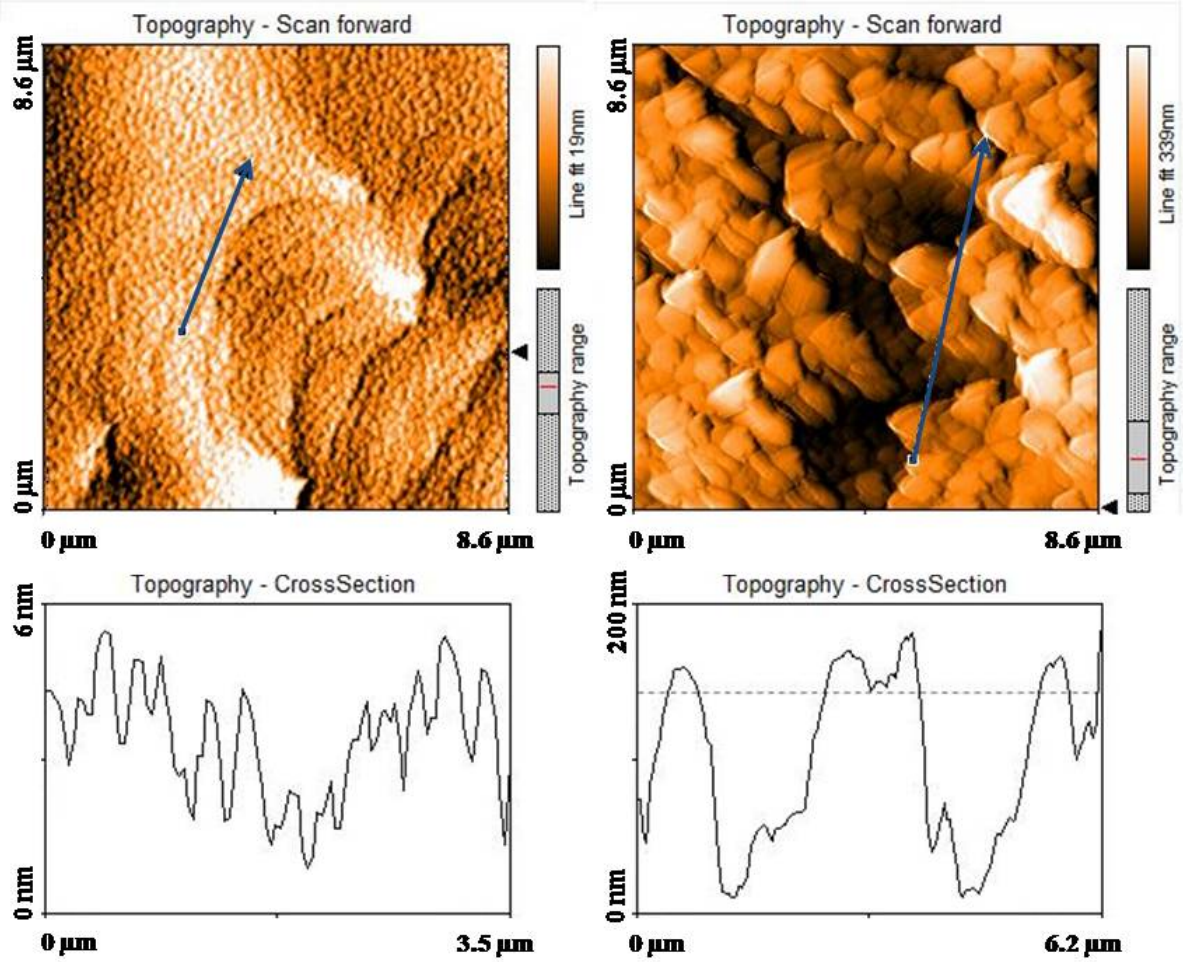

Fig. 8.8: AFM images in 'shaded mode' of HATCN films on Ag (111) and related cross sections along the marked arrows. The left image shows a $24\ nm$ thick film grown at room temperature, the right image shows a $40\ nm$ thick film grown at $400\ K$. Both images were taken ex-situ at room temperature.

The film grown at $300\ K$ consists of very small grains and can be characterized as an almost continuous layer-by-layer like film, whereas the film grown at $400\ K$ forms large islands. An XRD investigation of the film grown at $400\ K$ (see **Fig. 8.9**) has shown that the islands are crystalline yielding a similar reflection signal as the HATCN powder. In contrast to the huge crystalline islands on gold, on silver there is no preferential orientation of the crystallites with respect to the surface.

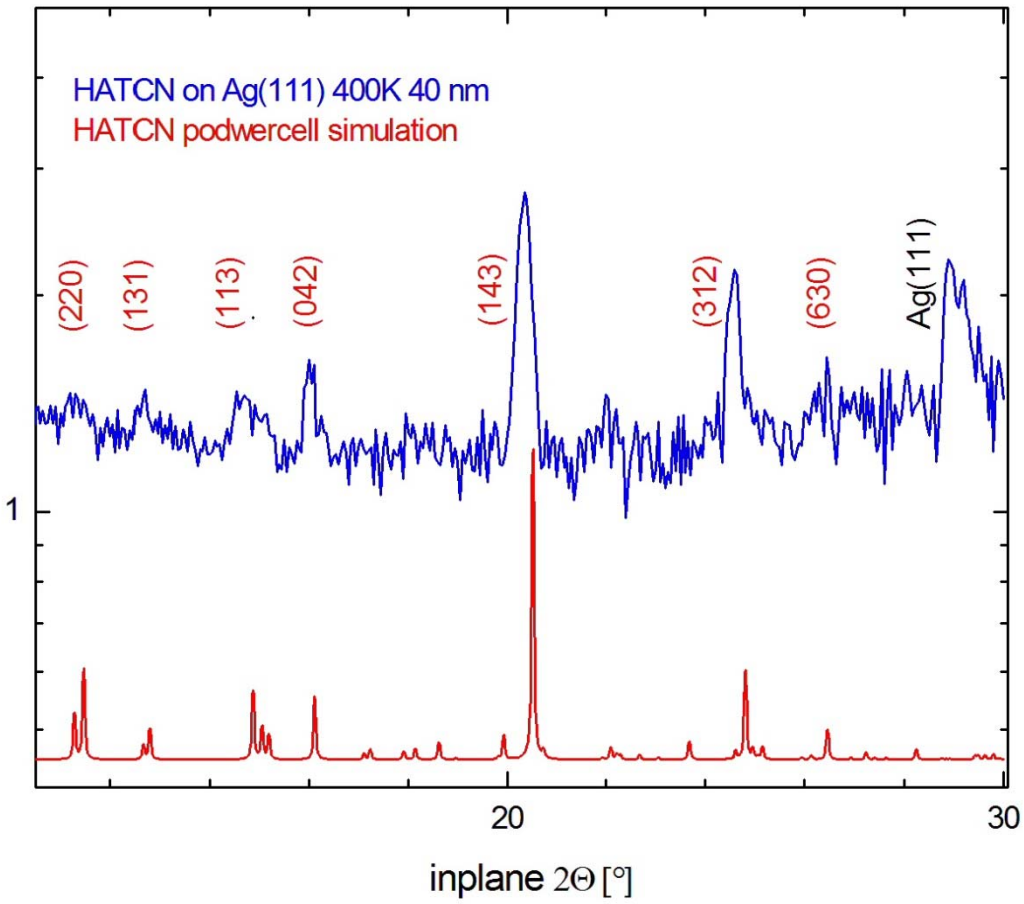

Fig. 8.9: Specular XRD scan of a $40\ nm$ thick HATCN film prepared at $400\ K$ on Ag (111). The peak positions fit very well to the simulated pattern of the HATCN powder.

8.4 Work function modification

The change of the work function of the Ag (111) surface relative to the clean surface as a function of the HATCN coverage is shown in **Fig. 8.10**. The films were prepared and measured at RT. The first series that is shown here in black was taken in January 09, the second series approximately one month later. Unlike the series on gold, both Ag-series exhibit similar characteristics. A possible reason of the better reproducibility on silver could be that the forces acting between the substrate and the HATCN molecules are stronger, leading to a more well defined growth of the first layers.

In general, the work function modification of a surface due to adsorption of material is regarded as an interplay of the Pauli push-back and the charge transfer between the material and the substrate. The push-back for large organic molecules on coinage metals is usually in

the range of 0.7 – 1.0 eV [131]. In the regime of the first lying monolayer ($0\,Å - 2\,Å$) the work function decreases by only $\approx 100\,mV$, indicating that the charge transfer almost compensates the push-back. Between $2\,Å$ and $8\,Å$ the work function increases by $\approx 1\,V$. In this regime, the molecules start standing upright. Thereupon the surface density of HATCN molecules increases by a factor of more than three ($0.58\frac{molecules}{nm^2}$ lying vs. $2\frac{molecules}{nm^2}$ standing). It is not clear yet to what extent the increase of the work function is related to a higher charge transfer. Preliminary DFT results [133] suggest that the charge transfer per molecule is smaller for standing molecules than for lying molecules, but the calculated values for the charge transfer depend strongly on the molecular arrangement in the standing monolayer, which is not known yet.

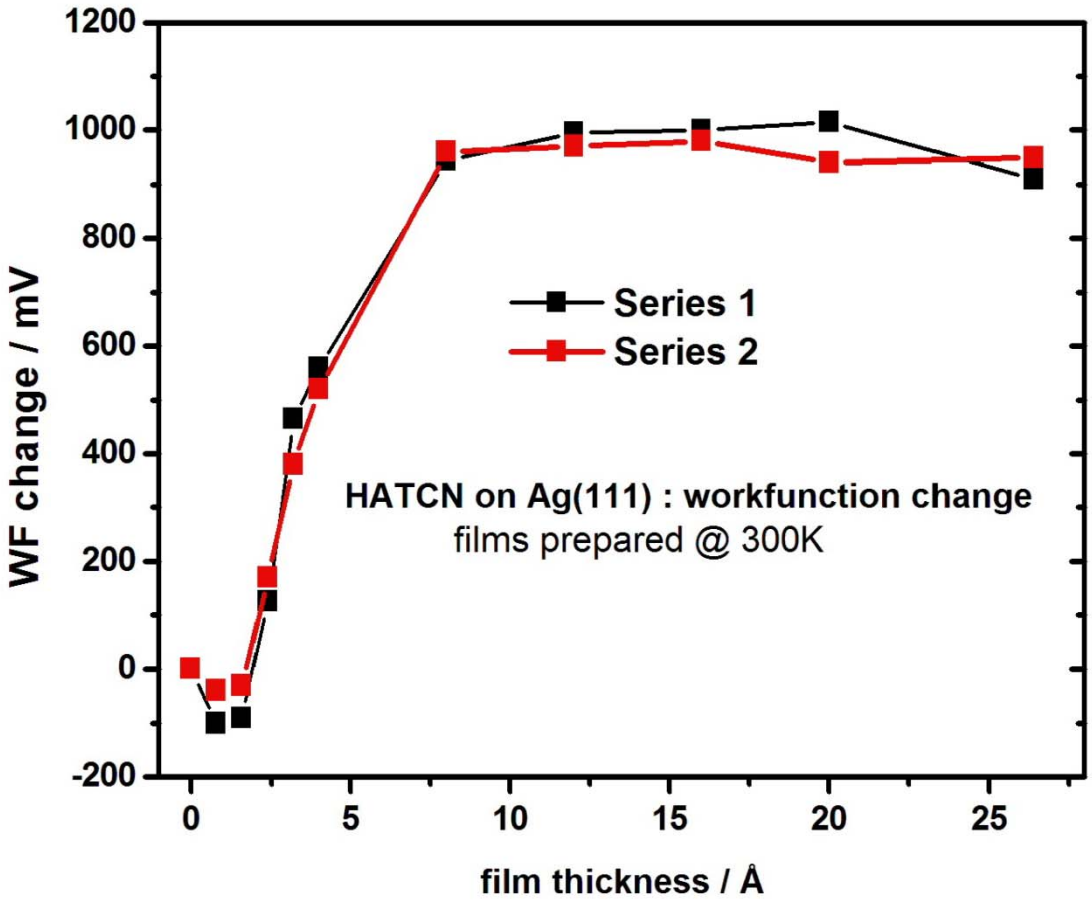

Fig. 8.10: Work function against film thickness. Y = 0 corresponds to the WF of clean Ag (111). Results of two different series taken at different dates are shown. Substrate temperature during film growth and measurements: $300\,K$.

At $8\,\text{Å}$ the work function saturates and remains constant thereafter. A very interesting comparison can be made between the work function change characteristics and the evolution of the mass 52 desorption (**Fig. 8.11**). In this figure the integrated thermal desorption peak areas of mass 52 and of the intact molecule are plotted against the film thickness according to the microbalance (desorbed molecules vs adsorbed molecules). $(CN)_2$ is a QMS cracking product of HATCN too and its signal is therefore proportional to the signal of the intact molecule. No desorption of intact molecules was observed above $\approx 500\,K$. Therefore the integration of the mass 52 peaks was performed from $550\,K$ up to $900\,K$ as only to take into account the $(CN)_2$ molecules which are formed by the dissociation of HATCN directly on the Ag surface.

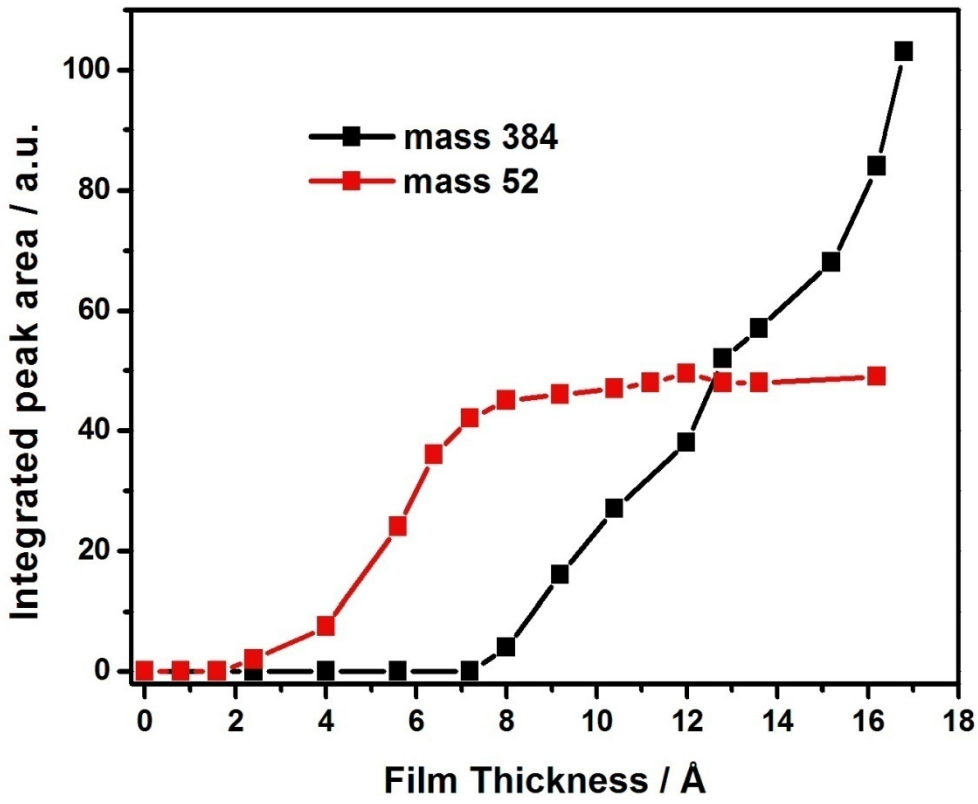

Fig. 8.11: Integrated peak areas of mass 52 ($(CN)_2$) and mass 384 (HATCN) from **Fig. 8.3**, **Fig. 8.4** and **Fig. 8.5** as a function of the mean film thickness (adsorbed amount vs. desorbed amount).

It is remarkable that in all coverage regimes the desorption of the mass 52 shows similar features as the work function change: The lying monolayer exhibits no desorption and almost

no work function change. As discussed in the previous sections, these lying molecules tend to stand up and form a monolayer of standing molecules as the molecular density on the surface is increased. These standing molecules feature a partial desorption the intensity of which can be followed in TDS and which fits nicely to the increase of the work function of the surface. Both curves, the work function change and the integrated peak area of the mass 52 desorption, saturate at $8\,\text{Å}$. At this coverage the standing layer is completed and additional molecules start building up the multilayer, which desorbs intact. Thus these molecules do not dissociate at the sample surface and do not lead to an increase of the desorption signal of the mass 52 between $550\,K$ and $900\,K$. The work function is also not influenced by the molecules growing on top of the monolayer. Considering all the presented data, the increase of the work function can be linked to the formation of a standing monolayer through the mass 52 desorption signal.

9 Summary

In this thesis the film growth and the adsorption/desorption kinetics of two different molecules, namely hexaphenyl (p6P) and hexaaza-triphenylene-hexacarbonitrile (HATCN), on various substrates (mica, KCl, Au, Ag) have been investigated with several surface science techniques. Particular attention was paid to the thermal stability of the grown films and to the influence of surface modifications. In the following a short summary including the most important results on the different systems is given.

9.1 p6P on mica (001)

On a surface which was cleaved under ambient conditions and subsequently taken into the vacuum chamber, the typical needle-like island growth takes place at room temperature. Thermal desorption spectroscopy revealed that prior to the formation of the islands, a more strongly bound wetting layer of $0.2\ nm$ mean thickness is formed (*Stranski–Krastanov* growth mode). In both, the wetting layer and the needle-like islands, the molecules are oriented with their long axes parallel to the surface. The initial adsorption and ultra-thin film layer growth of hexaphenyl (p6P) on mica (001) can be significantly influenced by surface modifications and by altering the surface temperature. Evaporation of p6P at $110\ K$ leads to small crystallites, which cover almost the whole surface. This film is stable up to room temperature, but recrystallizes to a needle-like film above $350\ K$, prior to desorption at about $500\ K$. From XPS and LEED measurements one finds that the freshly cleaved mica substrate is well ordered, but covered with approximately half a monolayer of carbon. By irradiation of a thick p6P film on mica with X-rays one can dissociate a fraction of the molecules and thereby increase the carbon amount of the mica surface up to a saturation coverage of one monolayer. This increased carbon coverage affects the p6P layer growth dramatically. The wetting layer disappears completely and the ultra-thin film consists of standing molecules, forming circular shaped islands. In the same way the layer growth can be influenced by

sputtering the mica surface, which leads to a disorganization of the well ordered surface structure. Again, no wetting layer is formed on this surface and the initial layer growth proceeds in the form of circular shaped islands of standing p6P molecules (island growth mode). This change of layer growth is attributed to changes of the dipole field on the surface, which exists on the freshly cleaved mica surface, but vanishes either due to a change of the chemical composition or due to a disordering of the surface structure.

From these results and from results reported in the literature one could deduce a 'general rule for p6P growth': If a wetting layer exists, it serves as a template for further film growth and because p6P molecules favor π-stacking, i.e. parallel alignment of the long molecular axis, the multilayer will be made up of lying molecules, too. Such a behavior is generally seen if the bonding between the p6P molecules and the substrate is quite strong and if the substrate is well ordered. In cases where the wetting layer is missing, the binding strength of the molecules to the substrate is so small that it is more favorable to stand up, thus minimizing the contact area to the substrate and maximizing the π-stacking. However, this general rule is disproven by the results shown in the following section on p6P on KCl (001).

9.2 p6P on KCl (001)

Thermal desorption spectroscopy measurements showed that no wetting layer of lying p6P molecules exists on KCl (001). On the other hand the film starts to grow in form of needle like islands made up of lying molecules. This is a quite unique result and contradicts the 'general rule for p6P growth' discussed in the end of the previous section. To the best of my knowledge, the p6P-KCl (001) system is the first example where needle like islands with lying molecules are formed without the existence of a wetting layer. From the very similar growth behavior of p6P on other alkali halide substrates, like NaCl and KBr [127], one can speculate that in general no wetting layers may exist on alkali halide substrates.

The p6P growth on KCl (001) was thereupon investigated as a function of temperature. Utilizing AFM, two different morphologies were found: the already mentioned needles which most probably consist of lying molecules and terraces consisting of molecules standing upright. These film morphologies strongly depend on the adsorption temperature of the films. At room temperature only islands of lying molecules are formed, whereas at higher temperatures the molecules tend to form terraces of standing molecules. Additionally, the

needle size increases with increasing temperature. The most significant change is observed between $400\ K$ and $450\ K$, where the height of the needles increases nearly by an order of magnitude. Additionally, films grown at temperatures far below room temperature ($90\ K$) were investigated in situ with combined XPS and TDS measurements and ex-situ with AFM. At an adsorption temperature of $90\ K$ the film consists of small crystallites, which cover almost the whole surface. This film remains stable up to $400\ K$, but recrystallizes above $450\ K$. The result of the recrystallisation is a film consisting of slightly elongated and ordered islands which are significantly higher than the ones before the recrystallization.

9.3 HATCN on Au (111)

The HATCN films on Au (111) exhibit a quite unusual temperature stability which depends on the initially adsorbed material. At and below room temperature, the first two layers grow in a layer-like fashion resembling wetting layers and are made up of lying molecules. Such layers are meta-stable since an increase of the coverage beyond two monolayers leads to a destabilization of the second layer which leads to a transition to an island like growth proceeding on the first monolayer. The temperature at which this transition takes place depends slightly on the initial film thickness and lies in the range of $350\ K$ (thick films) – $375\ K$ (thin films). The molecular arrangement within the islands corresponds to that of the HATCN bulk structure and features a preferential orientation with respect to the Au (111) surface. At the substrate-island interface, the primarily flat lying molecules of the first monolayer adapt to the bulk structure of the islands. With increasing initial coverage the average island size also increases and thus the amount of molecules of the first layer incorporated into the 3D islands increases too. The molecules in the first layer which are not covered by islands remain stable up to a higher temperature than those which have been incorporated into the islands. The reason for that is that the molecules in the first layer exhibit the same binding energy as the molecules in the islands, but a smaller pre-exponential factor which is a sign for a high mobility of the molecules. Therefore these molecules desorb at higher temperatures because prior to desorption more degrees of freedom can be excited. If the substrate surface is modified by a C-N layer prepared by intentional HATCN dissociation, the molecules in the first layer desorb at smaller temperatures, indicating either a lower binding energy or a reduced mobility of the molecules on the roughened surface. Keeping in

mind that the binding energies of all adsorption states on the clean surface are very similar and that the desorption temperature of HATCN on Au is mostly governed by the pre-exponential factor, the latter explanation seems more likely.

The work function change due to HATCN adsorption has turned out to be reproducible qualitatively, but not quantitatively. For thin layers the work function decreases until at ≈ 7 Å a minimum is reached which lies $200\ mV - 700\ mV$ below that on clean Au. Subsequent deposition leads to an increase of the work function which happens to go on up to 50 Å and above. During that increase the work function reaches values which range from the work function of the clean Au up to $200\ mV$ above that.

9.4 HATCN on Ag (111)

The growth of HATCN on Ag (111) is more complex than that on gold and features two coverage-dependent rearrangements of the molecules which in addition take place at different substrate temperatures. The initial film growth is characterized by molecules lying flat on the substrate forming a highly ordered (7x7) (so-called 'honeycomb') superstructure, as seen in LEED and STM. This layer is stable up to $900\ K$ which means that neither desorption nor dissociation of the molecules was observed. Therefore the binding strength of the molecules in the first lying monolayer could not be determined by TDS, but must be very high. Interestingly, the molecules in this temperature-stable layer rearrange as the coverage is increased above 2.4 Å and form a monolayer made up of standing molecules which exhibits desorption of HATCN fragments at $700\ K$, indicating a dissociation of the molecules. However, no intact molecules desorb which shows that the Ag-CN binding is very strong in this layer, too. The rearrangement of the lying monolayer into the standing monolayer was already seen at room temperature. When this layer has saturated at 8 Å, meta-stable layers form which wet the standing monolayer and on these layers again the film growth proceeds in form of islands. The meta-stable layers get incorporated into the islands as the coverage is increased, which is similar to the growth of HATCN on Au (111). Again, this rearrangement takes place between $350\ K$ and $375\ K$ depending on the film thickness.

The work function of Ag can be tailored by HATCN adsorption in a well-defined way. Up to 2.4 Å, i.e. as long as the molecules are lying flat on the surface, the work function somewhat

decreases by up to $100\ mV$. With the molecules standing up the density of Ag-CN bonds is increased which leads to a higher charge transfer and hence to an increase of the work function by $\approx 1\ V$ from 3 to $8\ \text{Å}$. Subsequent adsorption does not affect the work function.

In conclusion it has been shown in this work that the tailoring of thin organic films is possible and can be achieved by altering the growth parameters and by chemical and structural modifications of the substrates. It was found that there exists a delicate dependence of the film structure and morphology on the substrate temperature during and after adsorption, which determine to a large extent their physical and electronic characteristics. Thus the insights gained in the course of this thesis could help to improve the performance of novel devices based on thin organic films.

10 Appendix

A Tutorial on the use of the Nanosurf easyScan2 AFM

In this section it will be shortly explained how to handle a properly installed and working *nanosurf easyScan2 AFM system*. Detailed information on this AFM system can be found in the manuals of the manufacturer [112, 113].

A.1 Setting up the measurement

The first step is to put the *scan head* onto the *AFM sample stage* and to connect the *scan head* with the *controller* via the *scan head cable* (see **Fig. 10.1**). Furthermore it is recommended to connect the *scan head* with the *sample holder* via the *ground cable*. After having set up the AFM system properly, the sample is put on the *sample holder*.

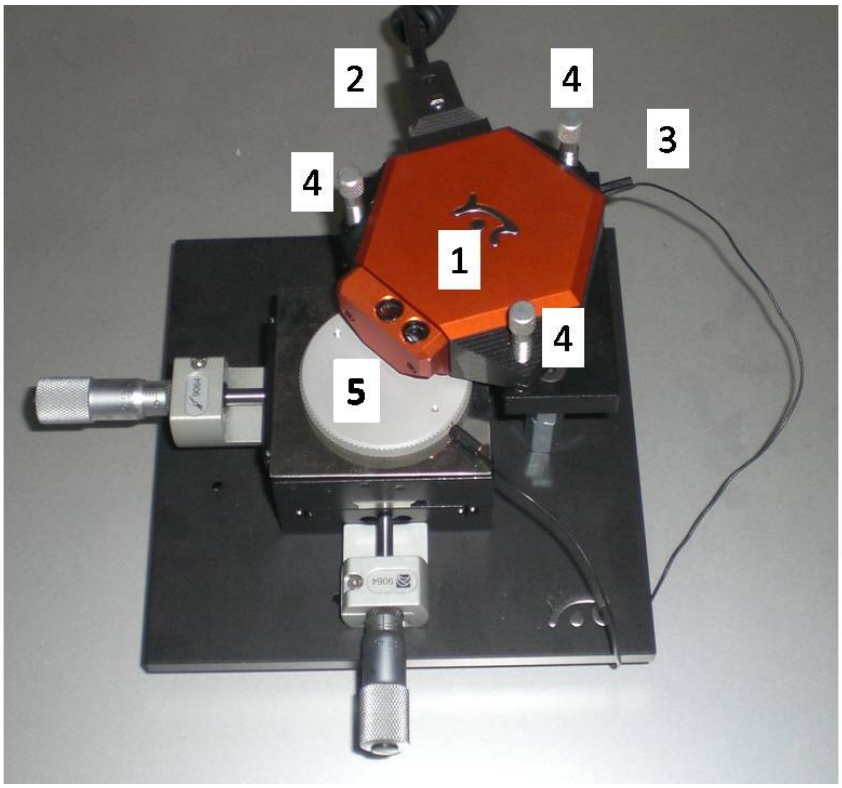

Fig. 10.1: Scan head (1) on the AFM sample stage. 2: Scan head cable, 3: Ground cable, 4: Leveling screws, 5: Sample holder.

After switching on the *controller unit*, the software is started by clicking the desktop symbol shown in **Fig. 10.2**.

Fig. 10.2: Desktop symbol of the nanosurf software.

Before approaching the tip to the sample, the *vibration isolation table* has to be switched on and by pressing *E* the isolation is activated. During the isolation process one can monitor the decrease of the vibrations in the *observing mode* by pressing the down button four times. After the finishing of the isolation process the red light will flash and now the tip can be approached to the sample in three different ways (see also **Fig. 10.3**):

1. manual coarse approach via the *leveling screws* on the *scan head*.
2. manual coarse approach via the software (*Advance*).
3. automatic fine approach via the software (*Approach*).

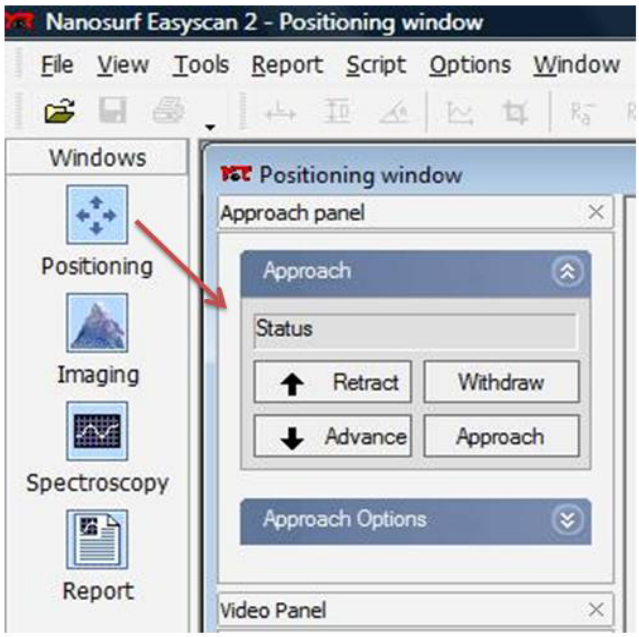

Fig. 10.3: Positioning window. *Retract* and *Advance* can be used for a coarse increase or decrease of the distance between the sample and the tip. *Approach* and *Withdraw* start the automatic fine adjustment of the tip position.

When using the manual approach (either via the leveling screws or by pressing *Advance*) it is recommended to keep a certain distance of $\approx 0.5\ mm$ between the cantilever and the sample in order to avoid any physical contact, which could damage the tip. If desired, this distance can be monitored with the magnifier glass, which is located on top of the scan head. In the final position the scan head should be as horizontal as possible. After finishing the manual coarse approach, the automatic fine approach can be triggered independently from the sample-tip distance, but the smaller this distance, the faster the scan head reaches its measuring position. After finishing a measurement or if one desires to investigate another part of the sample, the tip has first to be automatically withdrawn via the software (*Withdraw*) and afterwards manually via the software (*Retract*) or the leveling screws.

Right after starting the automatic approach, the software checks the condition of the tip by measuring the resonance curve which contains a measurement of the resulting cantilever vibration as a function of the excitation frequency. When the search is successful, the resonance curve contains a single peak at the free resonance frequency of the cantilever. Afterwards a second, fine-tuning search is performed in a $3\ kHz$ frequency range around the resonance frequency detected in the coarse search, as shown in **Fig. 10.4**.

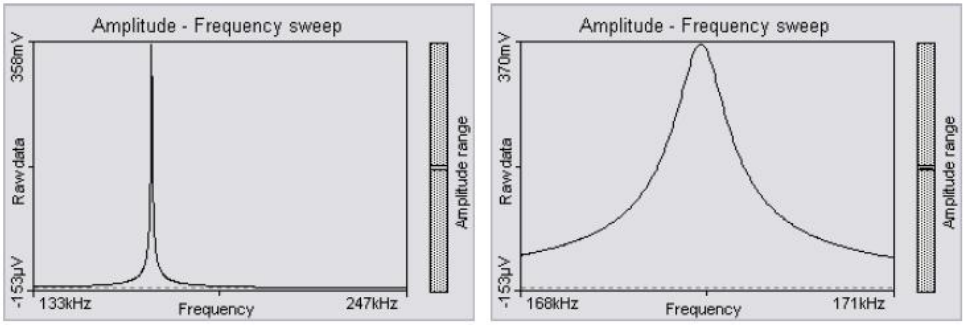

Fig. 10.4: Cantilever resonance curve. **Left:** Coarse search; **Right:** Fine-tuning search.

If the search of the resonance frequency has not been successful, very often a restart of the software can solve this problem. If this is not the case, the tip has to be changed (instructions in ref. [112], p. 31).

A.2 Imaging

The imaging window allows setting up the basic image properties and is almost self-explanatory (see **Fig. 10.5**). The rotation determines the direction of the scan and thus which slope has to be altered in order to correct the tilting of the sample with respect to the scan head:

- If the rotation is set to 0° the X-slope has to be corrected.
- If the rotation is set to 90° the Y-slope has to be corrected.

Another very important button is the *photo*-button on the right upper corner of **Fig. 10.5**. If this button has been activated, the software will automatically save the image as soon as it has been finished. The recorded image is now displayed in a new window with the name *image x* (*x* being a sequence number) and can be saved in two different ways: Either by *File - Save* or *File - Save as*, which saves the whole data file belonging to this image in the standard .nid format and allows an off-line processing of the image data any time. The other possibility is to export (*File – export*) either the *current chart* (activated chart, blue frame) or the *current document* (all charts) as an image (e.g. .jpg or .bmp file) without any data information.

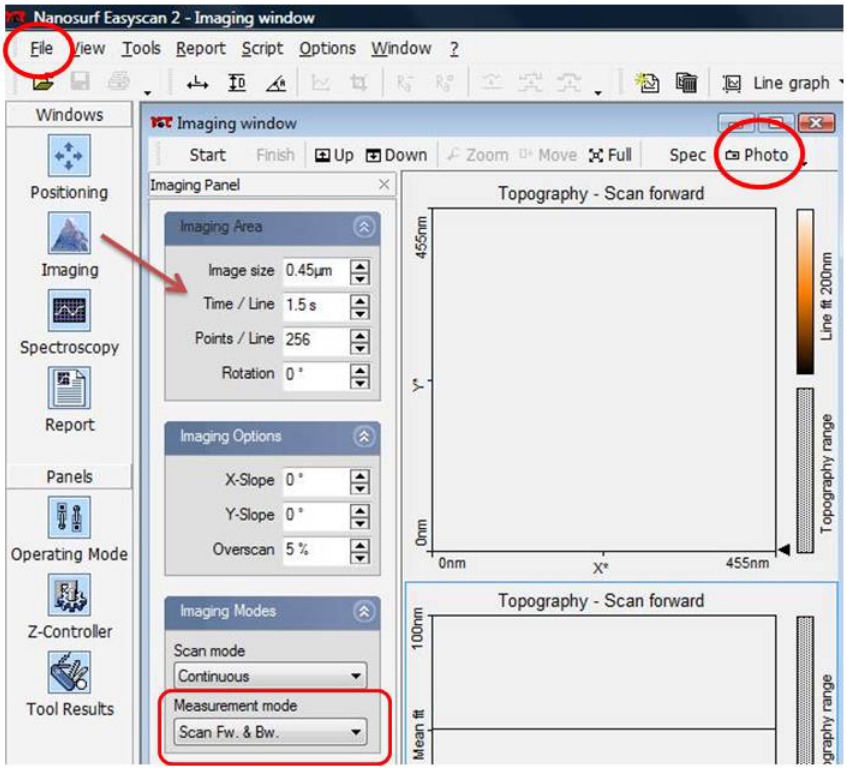

Fig. 10.5: Imaging window. Here the image size (typically $1 - 8.6\ \mu m$), the time per line (typically $1 - 2.5\ s$) and the resolution of the images (*points / line*, standard: 256) can be set up. The *rotation* determines the scan direction. Please make sure to scan forward and backward (framed in red) to allow for the dual line scans which are needed to get information on the quality of the used parameters. *Overscan* determines the amount by which the scan range of each line is made larger than the measurement range, relative to the image width (standard: 5%). Thus edge effects, caused by the reversal of the scanning motion, are not displayed in the measurement. The saving and export options can be found under *File* (upper left corner). The *photo* button is located in the right upper corner.

There are several parameters which can be adjusted to improve the images. **The most important parameters for the image improvement are the loop gains (P-gain, I-gain) and the free vibration amplitude, which can be found in the Z-controller panel and in the operating mode panel, respectively**. The parameters which are now displayed as the default parameters had been saved before because they worked very well for most p6P and HATCN films.

Starting with the *Z-controller panel* (**Fig. 10.6**, **right**), the set point denotes the relative cantilever vibration amplitude (after the fine approach) with respect to its free vibration amplitude. For example, when a set point of 70% is used, the controller will move the tip closer to the sample until the vibration amplitude has decreased to 70% of the vibration amplitude far away from the sample. Thus the set point determines the distance between the tip and the sample. In order to preserve the tip it is recommended to use a set point between 60% and 70%.

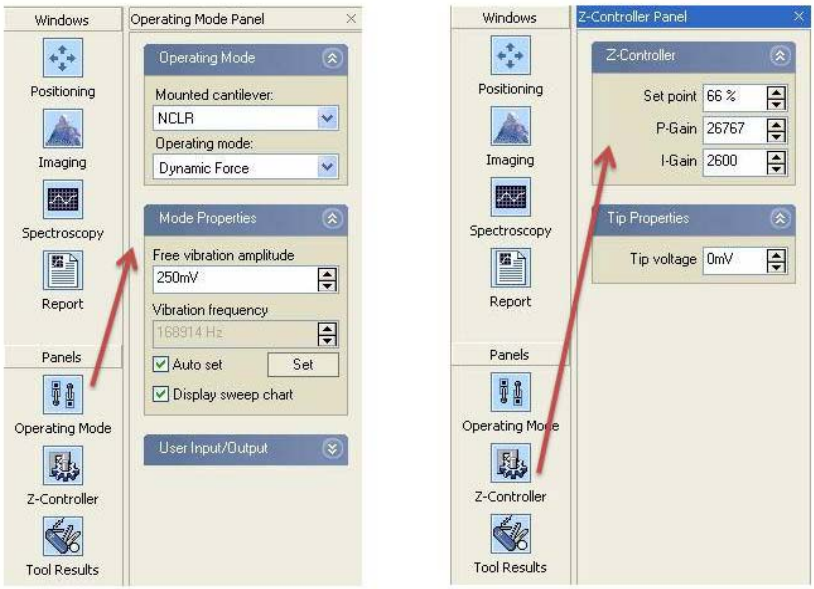

Fig. 10.6: Left: *Operating mode panel*; The mounted cantilever is a non-contact cantilever (*NCLR*) and the AFM is run in the *dynamic force* mode. Here the *free vibration amplitude* can be optimized. **Right:** *Z-controller panel*. Here the *set point* and the loop gains can be optimized. The *tip voltage* is not used in this mode.

The *P-gain* (proportional) and the *I-gain* (integral) determine the speed of the controller. If the gain is too low, the controller will not follow the surface fast enough. If the gain is too high, the controller will overshoot and may start to oscillate. Thus, the image will contain many measurement artifacts. Usually the P-gain should be higher than the I-gain by a factor of 10. Typical values for the P-gain range from 20000 up to 30000. Unfortunately, there is a limit of 32767 for the P-gain.

The *free vibration amplitude* can be found in the *operating mode panel* (**Fig. 10.6**, **left**) and denotes the desired reference amplitude of the cantilever vibration. The cantilever vibrates at this amplitude when it is far away from the sample. The excitation strength is adjusted so that this vibration amplitude is reached. Typical values for the free vibration amplitude range from $100\ mV$ up to $200\ mV$, sometimes on very rough surfaces it is necessary to raise the amplitude to $600\ mV$ or $700\ mV$. In general, the quality of the obtained images can be significantly improved by altering the free vibration amplitude and this parameter is apart from the loop gains the most important one. A good way to check the used parameters is to have a look at the dual line scan during the measurement: The two lines (forward & backward scan) should not differ too much from each other. *NCLR* and *dynamic force* indicate that a non-contact cantilever is mounted and that the AFM is run in the non-contact (tapping) mode.

A.3 Image processing

Once the image data has been recorded and saved, it is always possible to create new images displaying this data (**Fig. 10.7**, **8**). The data contained in the .nid files (standard AFM files) can be displayed as (see **Fig. 10.7**, **10**)

- single line scan (forward)
- dual line scan (forward & backward, only possible if activated in the imaging window)
- topography map
- shaded map
- 3D view

Fig. 10.7: Image processing bar; **1**: Measure length; **2**: Measure distance; **3**: Measure Angle; **4**: Create cross-section; **5**: Cut out area; **6**: Glitch filter; **7**: Noise filter; **8**: Create new chart; **9**: Delete chart; **10**: Select chart type; **11**: Select data filter; **12**: Select signal; **13**: Show chart properties dialog;

The topography image is the standard image type, which displays the surface corrugation according to a color scale. On the right-hand side of the topography map there is a small black arrow which points to the line which is depicted in the current line scan. Of uttermost importance during the measurement is to monitor the dual line scan, which gives information on the reliability of the obtained images and helps to optimize the imaging parameters. The shaded image mode is a hybrid between the standard topography map and its derivative. This mode is often used because small surface structures can be seen more clearly that way than in the standard topography mode. Eventually it is also possible to let the software draw a 3D image. If desired, the scales of all the images can be set manually in the *chart properties dialog* (**Fig. 10.7**, **13**), which is advisable if there is an artifact in the image which distorts the scale. The *data filter* panel (**Fig. 10.7**, **11**) describes the way the data is processed before it is displayed.

- Raw Data: The data is not processed.
- Mean Fit: The mean value of each line of data points is calculated and then subtracted.

- Line Fit: The best fit line for each line of data points is calculated and then subtracted.
- Derived Data: The difference between two successive data points (derivative) is calculated.
- Parabola Fit: The best fit parabola for each line of data points is calculated and then subtracted
- Polynomial Fit: The best fit fourth order polynomial for each line of data points is calculated and then subtracted.

Typically, the mean fit and the line fit yield the best images.

Further, the images can be evaluated and analyzed with the help of the *tools bar* (**Fig. 10.7**, **1-7**). Tools can be used in all charts, both during measurement and off-line. Before using a tool on a chart, the chart must be activated by clicking onto it (blue frame appears). Among the tools there are also filters which can be used to reduce periodical artifacts (*glitch filter, noise filter*).

The most important tool is the *cross section tool* (**Fig. 10.7**, **4**), which creates a line scan along a user-defined line in an activated chart. In this way structures in the sample can be analyzed in their height and length by the corresponding tools. Please note that the line along which the cross section has been created is indicated in the corresponding image and needs to be saved by exporting the chart as an image (e.g. as .jpg or .bmp) immediately. If the file is saved as an .nid file, this information will be lost.

B Tutorial on the use of the UHV Kelvin Probe

This section aims to demonstrate shortly how a work function measurement using the built-in UHV Kelvin probe of *KP Technology LTD* is carried out. Traditionally, the work function difference between two surfaces was determined by vibrating the reference surface above the sample and adjusting the variable 'backing potential' V_b until a zero or null output resulted. However, this mode of detection is extremely sensitive to noise since the Kelvin probe signal is diminishing with respect to the noise background. Therefore the Kelvin probe system manufactured by *KP Technology LTD* utilizes an off-null detection where the signal is measured at high signal levels far from balance. For further details please refer to the manual of the manufacturer [134].

B.1 Quick start of the software

In the initial position the tip should be located a few mm away from the sample in order to avoid sample damage when the tip starts vibrating later on. After having positioned the sample and the tip properly, the first step is to start the Kelvin probe software by clicking the desktop symbol shown in **Fig. 10.8**.

Fig. 10.8: Desktop symbol of the Kelvin probe software.

After the software has started one has to open a parameter file, see **Fig. 10.9** and **Fig. 10.10**. For a start, I would recommend to choose the file *standard.par*. Experienced users can create their own parameter file by clicking *New Parameter File* in **Fig. 10.9**.

Fig. 10.9: Click *File – Open Parameter File* to open an existing parameter file and *File – New Parameter File* to create a new parameter file.

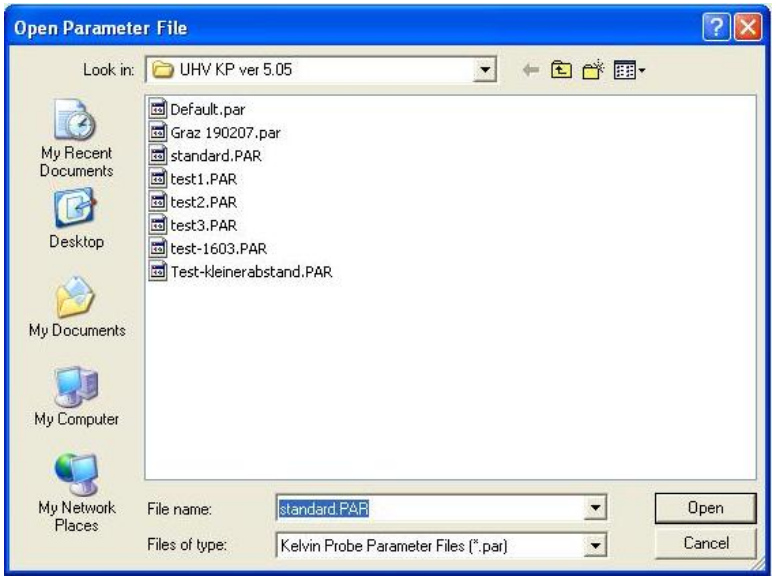

Fig. 10.10: The *Open Parameter File* dialog.

Once a parameter file has been opened a window similar to the one shown in **Fig. 10.11** will be displayed. There are three tabs: one for the *Setup Probe and Data Acquisition*, a second tab for the *Work Function Measurement* and a third for *Advanced/Diagnostics*.

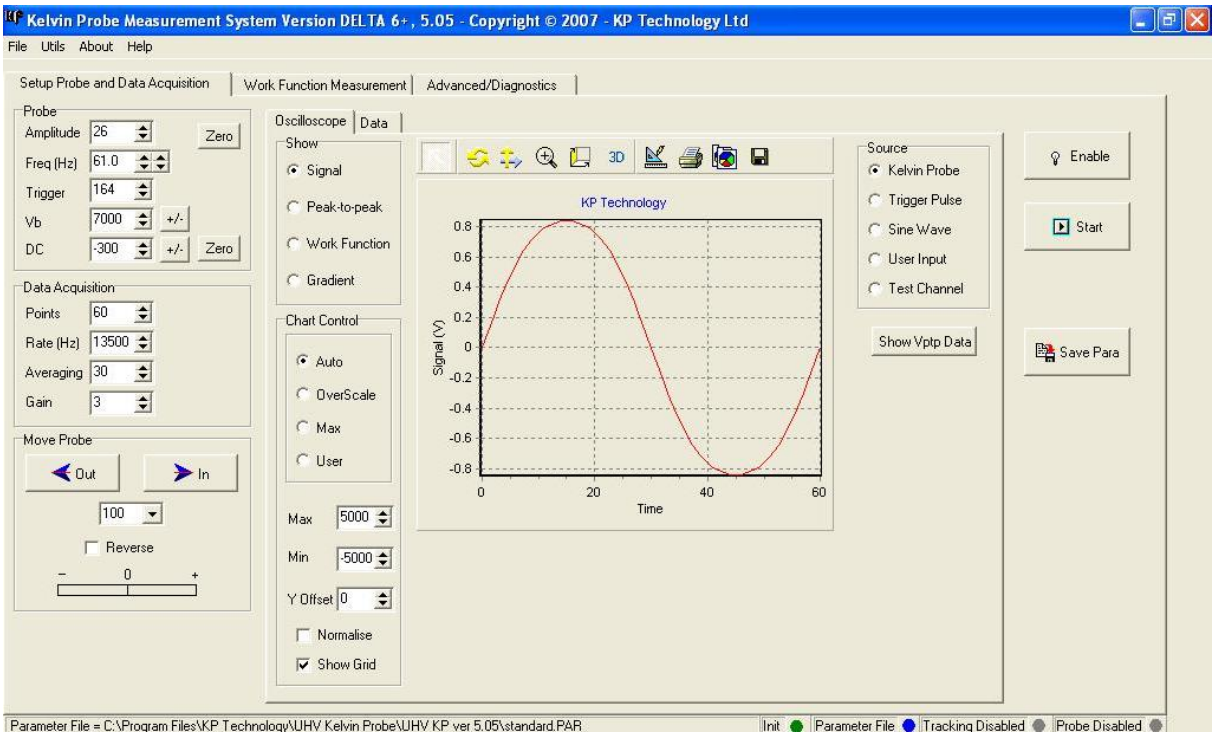

Fig. 10.11: After opening the parameter file *standard.par*.

The *Setup Probe and Data Acquisition* page contains groups for setting-up the probe, data acquisition, tip translation and measurement options. The values of the probe and data acquisition parameters have turned out to work fine, but of course **experienced users may try to further optimize them with the help of the KP manual** [134]. Before a measurement can be started, the probe has to be activated by clicking *Enable* (**top right** in **Fig. 10.11**). Now the tip is vibrating and one can start the data acquisition by clicking *Start* in the *Work Function Measurement* tab (**Fig. 10.12**):

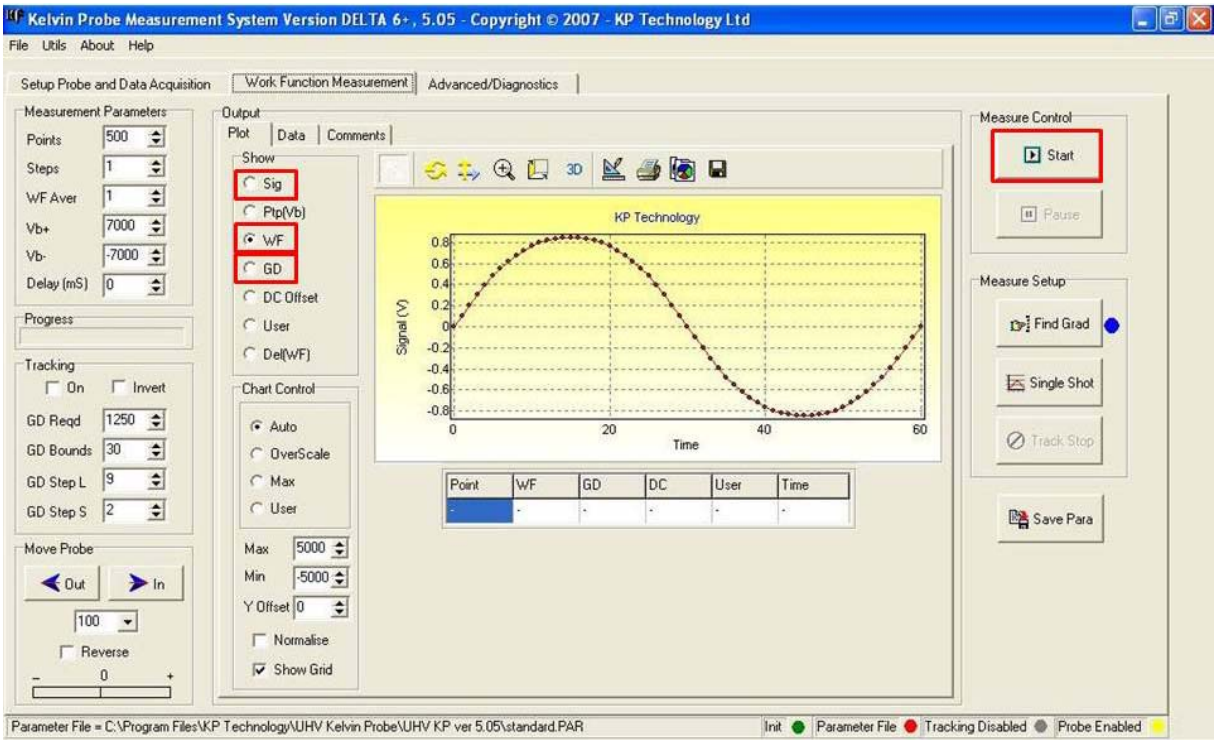

Fig. 10.12: The measurement page. The *Start*-button in the top right corner starts the measurement. The *Show* group determines what is displayed in the chart: *Sig* is the signal from the tip, *WF* (automatically activated after pressing the *Start*-button) is the measured work function and *GD* is the gradient, which gives information on the sample-tip distance.

After starting the measurement, automatically the work function is displayed in the chart. Please note that the value of the work function strongly depends on the sample-tip distance and has no meaning unless the tip has been moved as closely as possible towards the sample without touching it. It has to be pointed out here that in order to prevent damage of the sample the direct contact with the tip must be avoided.

B.2 Positioning the tip

In order to approach the tip to the sample, the signal of the tip has to be observed by clicking *Sig* (see again **Fig. 10.12**). The tip is moved towards the sample by turning the wheel attached to the UHV Kelvin probe (see **Fig. 10.16**). In **Fig. 10.13** the evolution of the signal is shown as a function of the sample-tip distance. In the initial position, i.e. when the sample-tip distance is large, the signal will probably be similar to the one shown in **Fig. 10.13a**. As the sample-tip distance decreases (**Fig. 10.13a-f**), the amplitude of the signal gets higher (up to $6\,V$ here) and the curve should exhibit exactly one minimum and one maximum. During the

approach the signal must remain symmetric with respect to the $0\ V$ line. If this is not the case, like in **Fig. 10.13f**, the tip is already touching the sample and has to be withdrawn quickly. The work function measurement can be started when the signal looks similar to **Fig. 10.13d** or **Fig. 10.13e**, indicating that the sample-tip distance is sufficiently small, but not zero.

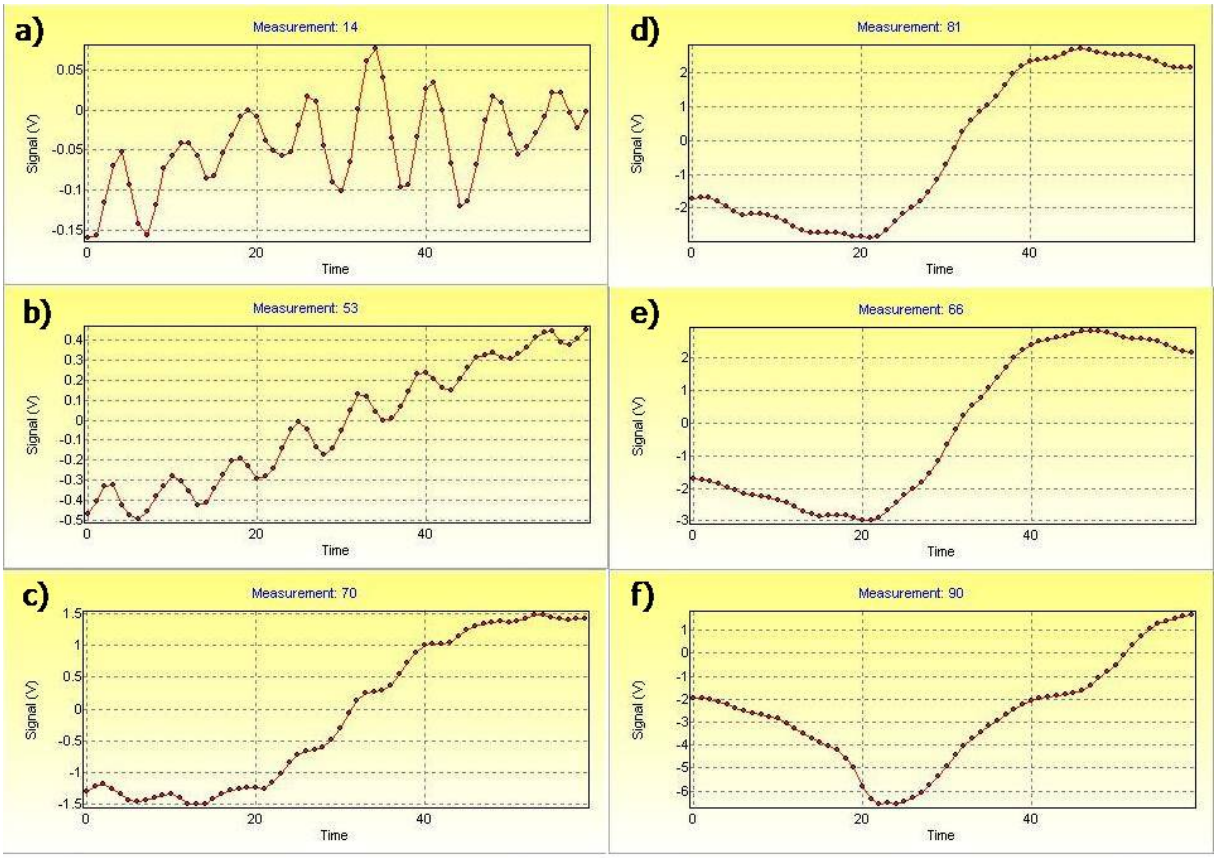

Fig. 10.13: Signal of the tip as a function of the tip-sample distance, starting from **a)** *large distance* to **f)** *no distance* (tip already touches the sample). When the signal looks similar to the charts shown in **d)** and **e)** the work function measurement can be started.

B.3 The work function measurement

The work function, the gradient and the signal can be observed throughout the measurement without affecting it by selecting the desired mode in the *Show* group. By checking the signal from time to time it can be ascertained that the sample-tip distance stays constant during the measurement, i.e. that the tip does not suddenly start touching the sample. Another way to monitor the sample-tip distance is to observe the gradient (*GD*): the higher the gradient, the

smaller is the sample-tip distance. **Fig. 10.14** shows the evolution of the work function during a measurement.

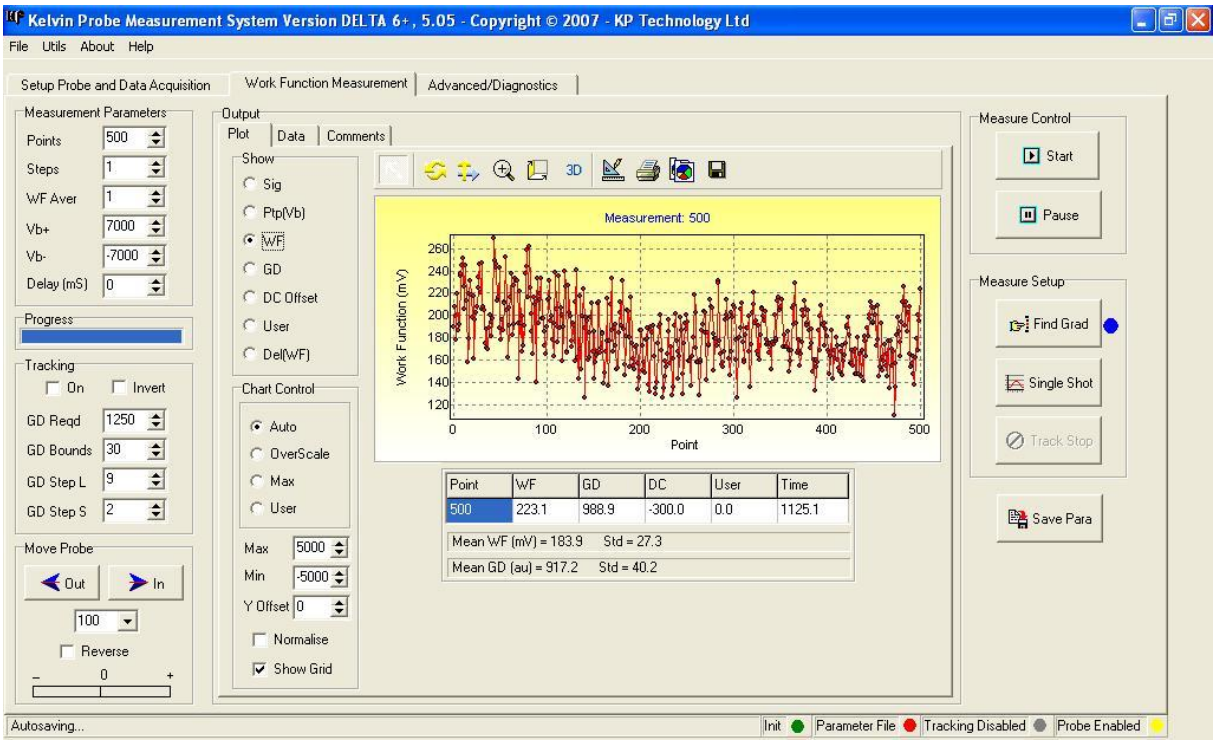

Fig. 10.14: The result of a measurement after 500 points. Beneath the chart the values for the mean work function and the mean gradient are displayed.

There are always slight changes in the work function and the gradient during a measurement. Hence the mean work function is displayed beneath the work function chart together with the mean gradient. The mean gradient becomes particularly important if the sample has to be moved during a series of work function measurements, for instance when the work function is studied as a function of the film thickness. Here the gradient helps to find again the tip-sample distance at which the related work function measurements of the same series were taken. Since the work function depends on the tip-sample distance, it is of utmost importance that all the measurements of a series, which are compared with each other later on, are taken at the same tip-sample distance (same gradient).

The reliability of the gained values depends on the number of points that have been measured. It is recommended to record at least 500 points in order to reduce the influence of the noise on the gained work function values.

After the preset number of points has been reached, the software offers the possibility to save it as a data (.dat) file (**Fig. 10.15**). These data files can be processed in ORIGIN. However,

often it is sufficient to write down the mean WF and the mean GD together with the corresponding standard deviations.

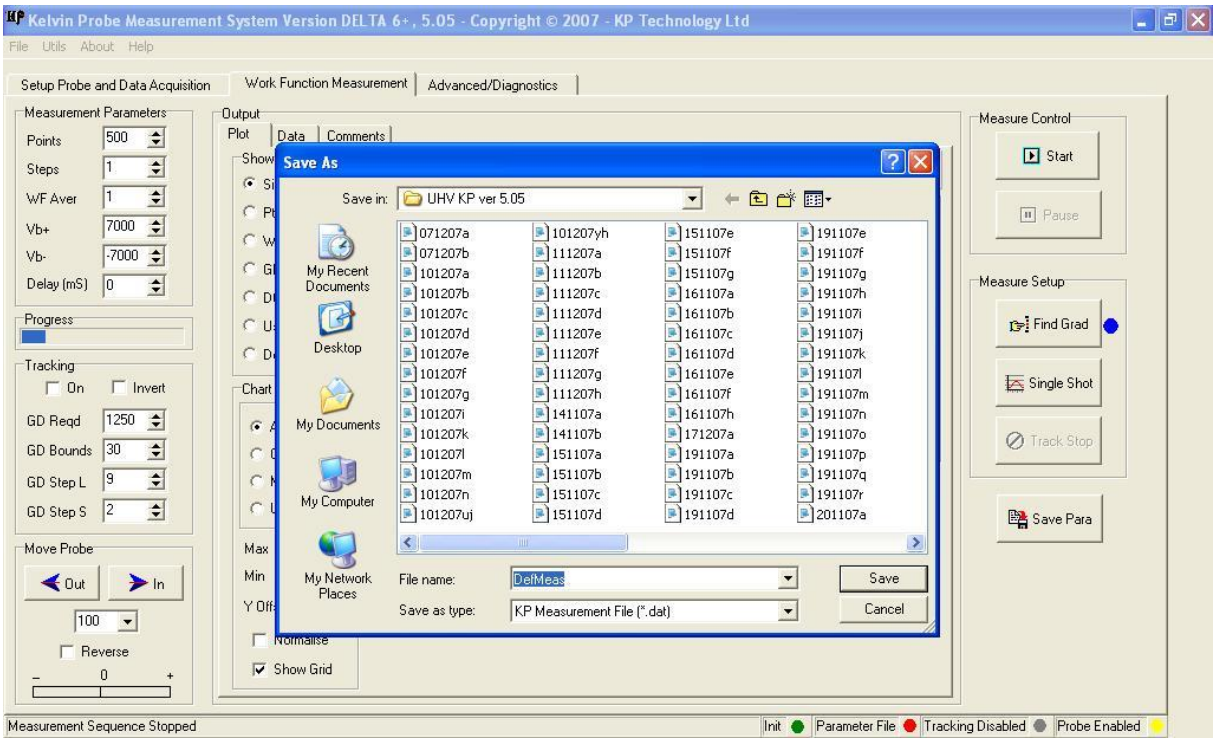

Fig. 10.15: If desired, the measurement can be saved as a data file (.dat) when it is finished.

B.4 Hints & tips

It has already been pointed out that the work function depends on the sample-tip distance, which can be monitored by means of the gradient. In general the work function measurement will be 'better' (low-noise, reliable, stable) the higher the gradient is. Due to the macroscopic size of the tip a high gradient is only possible if the tip and the sample are totally parallel to each other, which has to be taken care of already when attaching the sample to the sample holder in air: avoid any tilting of the sample.

From time to time the signal of the tip stays constant at $13\ V$ and does not change upon any action. In that case an electronic component (**AD 549 JH**, operational amplifier) inside the *UHV tip amplifier* (connects the digital control unit to the Kelvin probe) has broken down and must be replaced (see **Fig. 10.16**).

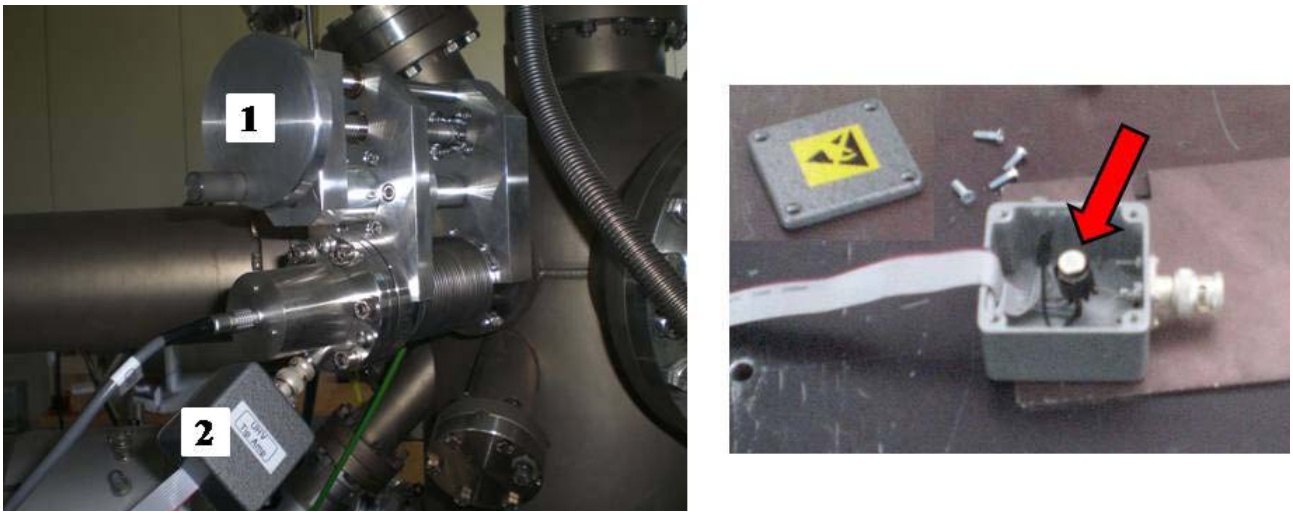

Fig. 10.16: **Left:** Photograph of the UHV Kelvin probe. 1: Positioning wheel to approach or withdraw the tip, 2: UHV tip amplifier. **Right**: Detail and interior view of the UHV tip amplifier. The red arrow points to the electronic component that must be replaced if the signal remains constant at $13\,V$.

Due to the sensibility of this electronic component to voltage swings of some of the other attachments to the UHV chamber (especially XPS and turbo pump cooling system) it is recommended to unplug the UHV tip amplifier if the Kelvin probe is not used for a longer time.

C List of publications and conference contributions

C.1 Publications in international scientific journals

1. *Characterization of step-edge barriers in organic thin-film growth.*
G. Hlawacek, P. Puschnig, **P. Frank**, A. Winkler, C. Ambrosch-Draxl, C. Teichert,
Science 321 (2008) 108.

2. *A study on the formation and thermal stability of 11-MUA SAMs on Au(111)/mica and on polycrystalline gold foils.*
J. Stettner, **P. Frank**, T. Grießer, G. Trimmel, R. Schennach, E. Gilli, A. Winkler,
Langmuir 25 (2009) 1427.

3. *Characterization of 11-MUA SAM formation on gold surfaces.*
J. Stettner, **P. Frank**, T. Grießer, G. Trimmel, R. Schennach, R. Resel, A. Winkler,
Springer proceedings in physics 129 (2009) 101.

4. *Layer growth and desorption kinetics of a discoid molecular acceptor on Au (111).*
P. Frank, N. Koch, M. Koini, R. Rieger, K. Müllen, R. Resel, A. Winkler,
Chemical physics letters 473 (2009) 321.

5. *Origin of the low-energy emission band in epitaxially grown para-sexiphenyl nanocrystallites.*
A. Kadashchuk, S. Schols, P. Heremans, Y. Skryshevski, Y. Piryatinski, I. Beinik, C. Teichert, G. Hernandez-Sosa, H. Sitter, A. Andreev, **P. Frank**, A.Winkler,
The journal of chemical physics 130 (2009) 084901.

6. *SAM of 11-MUA grown on polycrystalline Au foils by physical vapor deposition in UHV.*
P. Frank, F. Nußbacher, J. Stettner, A. Winkler,
Springer proceedings in physics 129 (2009) 107.

7. *Spectroscopy of defects in epitaxially grown para-sexiphenyl nanostructures.*
A. Kadashchuk, Y. Skryshevski, I. Beynik, C. Teichert, G. Hernandez-Sosa, H. Sitter, A. Andreev, **P. Frank**, A. Winkler,
Springer proceedings in physics 129 (2009) 121.

8. *Search for a wetting layer in the film growth of para-hexaphenyl on KCl(001).*
P. Frank, G. Hernandez-Sosa, H. Sitter, A. Winkler,
Thin solid films 516 (2008) 2939.

9. *Tailoring the film morphology of para-hexaphenyl on KCl(001) by surface temperature.*
P. Frank, A. Winkler,
Applied physics / A 90 (2008) 717.

10. *Characterizing Chemically Reactive Thin Layers: Surface Reaction of [2-[4-(Chlorosulfonyl)phenyl]ethyl]trichlorosilane with Ammonia.*
P. Pacher, A. Lex, V. Proschek, O. Werzer, **P. Frank**, S. Temmel, W. Kern, R. Resel, A. Winkler, C. Slugovc, R. Schennach, G. Trimmel, E. Zojer,
The journal of physical chemistry C 111 (2007) 12407.

11. *Influence of surface temperature and surface modifications on the initial layer growth of para-hexaphenyl on mica(001).*
P. Frank, G. Hlawacek, O. Lengyel, A. Satka, C. Teichert, R. Resel, A. Winkler,
Surface science 601 (2007) 2152.

12. *The influence of substrate temperature on the structure and morphology of sexiphenyl thin films on Au(111).*
S. Müllegger, G. Hlawacek, T. Haber, **P. Frank**, C. Teichert, R. Resel, A. Winkler,
Applied physics / A 87 (2007) 103.

13. *Spontaneous rearrangement of oligophenyl crystallites into nanofibers.*
C. Teichert, G. Hlawacek, A. Andreev, H. Sitter, **P. Frank**, A. Winkler, N.S. Sariciftci,
Applied physics / A 82 (2006) 665.

14. *Atom probe, AFM, and STM studies on vacuum-fired stainless steels.*

A. Stupnik, **P. Frank**, M. Leisch,

Ultramicroscopy 109 (2009) 563.

C. 2 Conference Contributions

1. *Tailoring the work function of metals using a cyano-based molecular acceptor: HATCN on Au(111) and Ag(111).*

   P. Frank, M. Koini, T. Djuric, N. Koch, R. Rieger, K. Müllen, R. Resel, A. Winkler,

   59th ÖPG Jahrestagung, Sept. 2009, Innsbruck, Austria.

2. *Temperature and coverage dependent dewetting of ultra-thin films of discoid organic molecules on Au(111) and Ag(111).*

   P. Frank, M. Koini, N. Koch, R. Rieger, K. Müllen, R. Resel, A. Winkler,

   Materials Research Society (MRS) Spring Meeting, April 2009, San Francisco, USA.

3. *Thermal Desorption of SAMs of 11-mercaptoundecanoic acid grown on polycrystalline Au-foils by physical vapor deposition in ultra high vacuum.*
   P. Frank, J. Stettner, F. Nußbacher, A. Winkler,
   58th ÖPG Jahrestagung, Sept. 2008, Leoben, Austria.

4. *AT & S Preis: Mound formation and level dependent Ehrlich-Schwoebel barrier in organic semiconductor thin film growth.*
   G. Hlawacek, P. Puschnig, **P. Frank**, A. Winkler, C. Ambrosch-Draxl, C. Teichert,
   58th ÖPG Jahrestagung, Sept. 2008, Leoben, Austria.

5. *Morphology and emission properties of ordered epitaxially grown organic nanocrystallites.*
   A. Kadashchuk, C. Teichert, I. Beinik, A. Andreev, G. Hernandez-Sosa, H. Sitter, **P. Frank**, A. Winkler,
   58th ÖPG Jahrestagung, Sept. 2008, Leoben, Austria.

6. *Atom Probe, AFM and STM study on vacuum fired stainless steel.*
   A. Stupnik, **P. Frank**, M. Leisch,
   58th ÖPG Jahrestagung, Sept. 2008, Leoben, Austria.

7. *The stability of 11-MUA SAMs grown on gold surfaces.*
   J. Stettner, **P. Frank**, T. Grießer, G. Trimmel, R. Schennach, R. Resel, A. Winkler,
   58th ÖPG Jahrestagung, Sept. 2008, Leoben, Austria.

8. *Chemical Control of the Local Charge Carrier Concentration in Organic Thin Film Transistors.*
   P. Pacher, H. Etschmaier, A. Lex, V. Proschek, E. Tchernychova, M. Sezen, O. Werzer, **P. Frank**, W. Grogger, R. Resel, R. Schennach, A. Winkler, G. Trimmel, C. Slugovc, E. Zojer,
   The 8th International Symposium on Functional Pi-Electron Systems, July 2008, Graz, Austria.

9. *A study of 11-MUA SAM formation on gold.*
   J. Stettner, **P. Frank**, T. Grießer, G. Trimmel, R. Schennach, R. Resel, A. Winkler,
   The 8th International Symposium on Functional Pi-Electron Systems. July 2008, Graz, Austria.

10. *Thermal Desorption Spectroscopy Investigations of SAMs of 11-mercaptoundecanoic acid grown on polycrystalline Au-foils by physical vapor deposition in ultra high vacuum.*
    P. Frank, J. Stettner, F. Nußbacher, A. Winkler,
    The 8th International Symposium on Functional Pi-Electron Systems. July 2008, Graz, Austria.

11. *Atom Probe and STM Study on Vacuum fired stainless steel.*
   A. Stupnik, **P. Frank**, M. Leisch,
   51st International Field Emission Symposium, June/July 2008, Rouen, France.

12. *Characterisation of 11-MUA SAM formation on gold surfaces.*
    J. Stettner, **P. Frank**, T. Grießer, G. Trimmel, R. Schennach, R. Resel, A. Winkler,

European Materials Research Society (EMRS) Spring Meeting, May 2008, Strasbourg, France.

13. *Ehrlich-Schwöbel barrier and Zeno effect in organic thin film growth.*
G. Hlawacek, C. Teichert, P. Puschnig, **P. Frank**, A. Winkler, C. Ambrosch-Draxl,
European Materials Research Society (EMRS) Spring Meeting, May 2008, Strasbourg, France.

14. *SAMs of 11-MUA grown on polycrystalline Au-foils by physical vapor deposition in UHV.*
P. Frank, F. Nußbacher, J. Stettner, A. Winkler,
European Materials Research Society (EMRS) Spring Meeting, May 2008, Strasbourg, France.

15. *Tuning of surface properties by photoreactive self assembled monolayers.*
G. Trimmel, T. Grießer, A. Lex, T. Höfler, P. Pacher, Q. Shen, G. Hlawacek, O. Werzer, A.M. Track**, P. Frank**, R. Schennach, G. Koller, M. Ramsey, C. Teichert, R. Resel, A. Winkler, E. Zojer, J. Adams, G.J. Leggett, W. Kern,
European Materials Research Society (EMRS) Spring Meeting, May 2008, Strasbourg, France.

16. *Chemical Control of Charge Carrier Concentration in Organic Thin Film Transistors: From Depletion to Enhancement.*
P. Pacher, A. Lex, V. Proschek, H. Etschmaier, E. Tchernychova, M. Sezen, O. Werzer, **P. Frank**, W. Grogger, R. Resel, R. Schennach, A. Winkler, G. Trimmel, C. Slugovc, E. Zojer,
European Materials Research Society (EMRS) Spring Meeting, May 2008, Strasbourg, France.

17. *Surface study on vacuum fired stainless steel by AFM and STM.*
A. Stupnik, **P. Frank**, M. Leisch,
Symposium on Surface Science, March 2008, St. Christoph, Austria.

18. *Step edge barrier in organic thin film growth.*
P. Puschnig, C. Ambrosch-Draxl, G. Hlawacek, **P. Frank**, A. Winkler, C. Teichert,

Symposium on Surface Science, March 2008, St. Christoph, Austria.

19. *Ehrlich-Schwöbel barrier and Zeno effect in organic thin film growth.*
G. Hlawacek, C. Teichert, P. Puschnig, **P. Frank**, A. Winkler, C. Ambrosch-Draxl,
DPG Spring Meeting, Feb. 2008, Berlin, Germany.

20. *Polymer Thin Film Characterization: A Combined Approach by X-ray Reflectivity and Spectroscopic Ellipsometry.*
H.-G. Flesch, O. Werzer, **P. Frank**, A. Blümel, J. Jakabovic, J. Kovac, G. Jakopic, R. Resel,
NFN Winterschool on Organic Electronics, Jan. 2008, Planneralm, Austria.

21. *Self assembled monolayers: A study of 11-MUA on Au surfaces.*
P. Frank, J. Stettner, T. Grießer, G. Trimmel, R. Schennach, R. Resel, A. Winkler,
NFN Winterschool on Organic Electronics, Jan. 2008, Planneralm, Austria.

22. *Investigation of chemically and photochemically reactive siloxane thin layers for surface modification.*
A. Lex, P. Pacher, S. Temmel, Q. Shen, G. Hlawacek, O. Werzer, A.M. Track, **P. Frank**, V. Proschek, R. Schennach, G. Koller, M. Ramsey, C. Teichert, R. Resel, A. Winkler, E. Zojer, W. Kern, G. Trimmel,
NFN Winterschool on Organic Electronics, Jan. 2008, Planneralm, Austria.

23. *Chemically and Photochemically Reactive Siloxane Layers for Modification of Inorganic Surfaces.*
A. Lex, P. Pacher, S. Temmel, Q. Shen, G. Hlawacek, O. Werzer, A.M. Track, **P. Frank**, V. Proschek, R. Schennach, G. Koller, M. Ramsey, C. Teichert, R. Resel, A. Winkler, E. Zojer, W. Kern, G. Trimmel,
Materials Research Society (MRS) Fall Meeting, Nov. 2007, Boston, USA.

24. *Zeno effect and step-edge barrier in organic thin films.*
C. Teichert, G. Hlawacek, **P. Frank**, A. Winkler,
American Vacuum Society (AVS) International Symposium & Exhibition, Oct. 2007, Seattle, USA.

25. *Ultra Thin Hexaphenyl Films on KCl (001) - Is there a Wetting Layer?.*
P. Frank, G. Hernandez-Sosa, H. Sitter, A. Winkler,
57th ÖPG Jahrestagung, Sept. 2007, Krems, Austria.
26. *Self assembled monolayers on gold: A study of 11-mercaptoundecanoic acid (11-MUA) on gold.*
J. Stettner, **P. Frank**, A. Winkler, T. Grießer, A.M. Track, G. Trimmel, W. Kern,
57th ÖPG Jahrestagung, Sept. 2007, Krems, Austria.

27. *Zeno effect and step-edge barrier in organic thin films.*
G. Hlawacek, C. Teichert, **P. Frank**, A. Winkler,
57th ÖPG Jahrestagung, Sept. 2007, Krems, Austria.

28. *Hexaphenyl on KCl (001): TDS, XPS and AFM measurements.*
P. Frank, G. Hernandez-Sosa, H. Sitter, A. Winkler,
NFN Meeting, Sept. 2007, Eisenerz, Austria.

29. *SAM formation of 11-mercapto-undecanoic acid (MUA) on gold: The influence of substrate structure and composition.*
J. Stettner, T. Grießer, **P. Frank**, A.M. Track, G. Trimmel, W. Kern, A. Winkler,
NFN Meeting, Sept. 2007, Eisenerz, Austria.

30. *Ammonia Sensing Organic Field Effect Transistor.*
P. Pacher, A. Lex, V. Proschek, E. Tchernychova, M. Sezen, O. Werzer, **P. Frank**, S. Temmel, W. Grogger, R. Resel, R. Schennach, A. Winkler, C. Slugovc, G. Trimmel, E. Zojer,
EUROMAT, Sept. 2007, Nürnberg, Germany.

31. *Photoreactive thin layers for organic electronics.*
A.M. Track, A. Lex, T. Grießer, G. Koller, P. Pacher, L. Romaner, **P. Frank**, J. Stettner, A. Winkler, R. Schennach, G. Trimmel, W. Kern, E. Zojer, M. Ramsey,
EUROMAT, Sept. 2007, Nürnberg, Germany.

32. *Tailoring the thin flm layer growth of 6P on mica(001).*

P. Frank, G. Hlawacek, T. Haber, R. Resel, C. Teichert, A. Winkler,
EUROMAT, Sept. 2007, Nürnberg, Germany.

33. *The importance of a wetting layer for the initial film growth of p-Hexaphenyl on various substrates.*
P. Frank, S. Müllegger, G. Hlawacek, C. Teichert, G. Hernandez-Sosa, H. Sitter, A. Winkler,
9th European Conference on Molecular Electronics (ECME), Sept. 2007, Metz, France.

34. *Tuning the Local Doping Level in Organic Thin Film Transistors by a Chemcial Reaction: from Depletion to Accumulation.*
P. Pacher, A. Lex, V. Proschek, E. Tchernychova, M. Sezen, O. Werzer, **P. Frank**, S. Temmel, W. Grogger, W. Kern, R. Resel, R. Schennach, A. Winkler, C. Slugovc, G. Trimmel, E. Zojer,
9th European Conference on Molecular Electronics (ECME), Sept. 2007, Metz, France.

35. *Para-sexiphenyl growth on modified mica(001).*
G. Hlawacek, C. Teichert, **P. Frank**, A. Winkler,
International Vacuum Congress, July 2007, Stockholm, Sweden.

36. *Zeno effect and step edge barrier in organic thin films.*
G. Hlawacek, **P. Frank**, C. Teichert, A. Winkler,
Gordon Conference, June 2007, South Hadley, USA.

37. *Organic Thin Film Transistor with a Reactive Intermediate Layer for Vapour Sensing Applications.*
P. Pacher, A. Lex, V. Proschek, O. Werzer, **P. Frank**, S. Temmel, E. Tchernychova, M. Sezen, G. Hlawacek, Q. Shen, C. Teichert, W. Grogger, R. Resel, R. Schennach, A. Winkler, C. Slugovc, G. Trimmel, E. Zojer,
106th Bunsentagung: Heterogene Neuartige Kohlenstoffstrukturen, May 2007, Graz, Austria

38. *Ammonia Sensing Organic Thin Film Transistors*.

P. Pacher, A. Lex, V. Proschek, O. Werzer, **P. Frank**, S. Temmel, E. Tchernychova, M. Sezen, G. Hlawacek, Q. Shen, C. Teichert, W. Grogger, R. Resel, R. Schennach, A. Winkler, C. Slugovc, G. Trimmel, E. Zojer,
DPG Spring Meeting, March 2007, Regensburg, Germany.

39. *Characterisation and modification of the hexaphenyl wetting layer on mica(001).*
P. Frank, G. Hlawacek, C. Teichert, A. Winkler,
DPG Spring Meeting, March 2007, Regensburg, Germany.

40. *Using organic thin film transistors with thin reactive layers for ammonia detection.*
P. Pacher, A. Lex, V. Proschek, O. Werzer, **P. Frank**, S. Temmel, E. Tchernychova, M. Sezen, G. Hlawacek, Q. Shen, C. Teichert, W. Grogger, R. Resel, R. Schennach, A. Winkler, C. Slugovc, G. Trimmel, E. Zojer,
Nano and Photonics Mauterndorf 2007, March 2007, Mauterndorf, Austria.

41. *Chemical Surface Reaction of 2-(4-Chlorosulfonylphenyl)ethyltrichlorosilane with Ammonia: A Combined Experimental and Theoretical Study.*
V. Proschek, P. Pacher, A. Lex, O. Werzer, **P. Frank**, S. Temmel, R. Resel, R. Schennach, A. Winkler, C. Slugovc, G. Trimmel, E. Zojer,
NFN Winter School on Organic Electronics, Jan. 2007, Planneralm, Austria.

42. *Fundamental aspects of oligo-phenylen adsorption and thin film layer growth on gold surfaces.*
S. Müllegger, **P. Frank**, I. Salzmann, T. Haber, R. Resel, G. Hlawacek, C. Teichert, K. Hänel, T. Strunskus, C. Wöll, S. Mitsche, P. Pölt, A. Winkler,
NFN Winter School on Organic Electronics, Jan. 2007, Planneralm, Austria.

43. *Thin Reactive Layers for Ammonia Detection with Organic Thin Film Transistors.*
P. Pacher, A. Lex, V. Proschek, O. Werzer, **P. Frank**, S. Temmel, E. Tchernychova, M. Sezen, G. Hlawacek, Q. Shen, C. Teichert, W. Grogger, R. Resel, R. Schennach, A. Winkler, C. Slugovc, G. Trimmel, E. Zojer,
NFN Winter School on Organic Electronics, Jan. 2007, Planneralm, Austria.

44. *Tailoring of Ultra Thin Hexaphenyl (6P) Films on Mica (001) through Surface Modifications.*
P. Frank, G. Hlawacek, C. Teichert, A. Winkler,
NFN Winter School on Organic Electronics, Jan. 2007, Planneralm, Austria.

45. *Oligo-phenylene adsorption and thin film layer growth on gold surfaces.*
S. Müllegger, **P. Frank**, I. Salzmann, T. Haber, R. Resel, G. Hlawacek, C. Teichert, K. Hänel, T. Strunskus, C. Wöll, S. Mitsche, P. Pölt, A. Winkler,
Wilhelm and Else Heraeus Seminar: Physik hochgeordneter organischer Grenzschichten, Jan. 2007, Bad Honnef, Germany.

46. *Adsorption, growth kinetics and desorption of hexaphenyl on/from mica(001).*
P. Frank, A. Winkler,
11th Joint Vacuum Conference (JVC), Sept. 2006, Prague, Czech Republic.

47. *Tailoring growth and morphology of 6P on mica(0001)*
P. Frank, A. Winkler,
56th ÖPG Jahrestagung, Sept. 2006, Graz, Austria.

48. *Reactive Gate Oxide Modification for Organic Thin Film Transistors.*
P. Pacher, A. Lex, V. Proschek, G. Hlawacek, Q. Shen, C. Teichert, A. Satka, J. Kovac, O. Werzer, S. Temmel, **P. Frank**, R. Resel, R. Schennach, A. Winkler, C. Slugovc, G. Trimmel, E. Zojer,
56th ÖPG Jahrestagung, Sept. 2006, Graz, Austria.

49. *Gate Oxide Modification by Reactive Thin Layers in Polymer Thin Film Transistors.*
P. Pacher, A. Lex, V. Proschek, S. Temmel, O. Werzer, **P. Frank**, G. Hlawacek, Q. Shen, K. Stubenrauch, E. Zojer, R. Resel, A.Winkler, C. Teichert, C. Slugovc, G. Trimmel,
8th Austrian Polymer Meeting, Sept. 2006, Linz, Austria.

50. *Experimental and Theoretical Study of Chemically Sensitive Layers in Organic Thin Film Transistors.*
P. Pacher, A. Lex, V. Proschek, S. Temmel, O. Werzer, **P. Frank**, K. Stubenrauch, R. Schennach, R. Resel, A.Winkler, C. Slugovc, G. Trimmel, E. Zojer,

3rd Semianual ISOTEC Meeting, July 2006, Graz, Austria.

51. *Hexaphenyl on Mica: Basic Research into Film Growth and Film Morphology.*
P. Frank, O. Lengyel, G. Hlawacek, C. Teichert, R. Resel, A. Winkler,
EUROFET Meeting, June 2006, Wildau, Germany.
52. *Reactive Dipole Layers for Chemical Sensing Applications.*
P. Pacher, A. Lex, V. Proschek, C. Auner, S. Rentenberger, O. Werzer, **P. Frank**, S. Temmel, R. Resel, A. Winkler, R. Schennach, C. Slugovc, G. Trimmel, E. Zojer,
European Materials Research Society (EMRS) Spring Meeting, June 2006, Nice, France.

53. *Morphology of sexiphenyl thin films.*
G. Hlawacek, A. Andreev, C. Teichert, **P. Frank**, A. Winkler, R. Resel, M. Ramsey,
DPG Spring Meeting, Mar. 2006, Dresden, Germany.

D Bibliography

[1] P. Puschnig, C. Ambrosch-Draxl, Phys. Rev. B 60 (1999) 7891.

[2] G. Leising, S. Tasch, F. Meghdadi, L. Athouel, G. Froyer, U. Scherf, Synth. Met. 81 (1996) 185.

[3] W. Graupner, G. Grem, F. Meghdadi, C. Paar, G. Leising, U. Scherf, K. Müllen, W. Fischer, F. Stelzer, Mol. Cryst. Liq. Cryst. 256 (1994) 549.

[4] F. Meghdadi, S. Tasch, B. Winkler, W. Fischer, F. Stelzer, G. Leising, Synth. Met. 85 (1997) 1441.

[5] H. Yanagi, S. Okamoto, T. Mikami, Synth. Met. 91 (1997) 91.

[6] G. Leising, S. Tasch, W. Graupner, Handbook of Conducting Polymers: Fundamentals of Electroluminescence in Paraphenylenetype Conjugated Polymers and Oligomers, second ed., Marcel Dekker, 1997.

[7] D.J. Gundlach, Y.-Y. Lin, T.N. Jackson, D.G. Schlom, Appl. Phys. Lett. 7 (1997) 3853.

[8] S. Tasch, C. Brandstätter, F. Meghdadi, G. Leising, G. Froyer, L. Athouel, Adv. Mater. 9 (1997) 33.

[9] G. Meinhardt, W. Graupner, G. Feistritzer, R. Schröder, E.J.W. List, A. Pogantsch, G. Dicker, B. Schlicke, N. Schulte, A.D. Schluter, G. Winter, M. Hanack, U. Scherf, K. Müllen, G. Leising, Proc. SPIE 3623 (1999) 46.

[10] T. Mikami, H. Yanagi, Appl. Phys. Lett. 73 (1998) 563.

[11] H. Yanagi, S. Okamoto, Appl. Phys. Lett. 71 (1997) 2565.

[12] R. Resel, I. Salzmann, G. Hlawacek, C. Teichert, B. Koppelhuber, B. Winter, J.K. Krenn, J. Ivanco, M.G. Ramsey, Org. Electron. 5 (2004) 45.

[13] B. Winter, J. Ivanco, F.P. Netzer, M.G. Ramsey, Thin Solid Films 433 (2003) 269.

[14] B. Winter, J. Ivanco, F.P. Netzer, M.G. Ramsey, I. Salzmann, R. Resel, Langmuir 20 (2004) 7512.

[15] G. Hlawacek, C. Teichert, A. Andreev, H. Sitter, S. Berkebile, G. Koller, M. Ramsey, R. Resel, Phys. Status Solidi (a) 202 (2005) 2376.

[16] G. Koller, S. Berkebile, J.R. Krenn, G. Tzvetkov, G. Hlawacek, O. Lengyel, F.P. Netzer, C. Teichert, R. Resel, M. Ramsey, Adv. Mater 16 (2004) 2159.

[17] S. Berkebile, G. Koller, G. Hlawacek, C. Teichert, F.P. Netzer, M.G. Ramsey,

Surf. Sci. 600 (2006) L313.

[18] M. Oehzelt, L. Grill, S. Berkebile, G. Koller, F.P. Netzer, M. Ramsey, Chem. Phys. Chem. 8 (2007) 1707.

[19] Y. Hu, K. Maschek, L.D. Sun, M. Hohage, P. Zeppenfeld, Surf. Sci. 600 (2006) 762.

[20] T. Haber, S. Müllegger, A. Winkler, R. Resel, Phys. Rev. B 74 (2006) 045419.

[21] S. Müllegger, A. Winkler, Surf. Sci. 600 (2006) 1290.

[22] C.B. France, B.A. Parkinson, Appl. Phys. Lett. 82 (2003) 1194.

[23] A. Andreev, T. Haber, D.-M. Smilgies, R. Resel, H. Sitter, N.S. Sariciftci, L. Valek, J. Cryst. Growth 275 (2005) 2037.

[24] A. Andreev, G. Matt, C.J. Brabec, H. Sitter, D. Badt, H. Seyringer, N.S. Sariciftci, Adv. Mater. 12 (2000) 629.

[25] F. Balzer, H.G. Rubahn, Appl. Phys. Lett. 79 (2001) 3860.

[26] F. Balzer, H.G. Rubahn, Surf. Sci. 507–511 (2002) 588.

[27] H. Plank, R. Resel, S. Purger, J. Keckes, A. Thierry, B. Lotz, A. Andreev, N.S. Sariciftci, H. Sitter, Phys. Rev. B 64 (2001) 235423.

[28] H. Plank, R. Resel, H. Sitter, A. Andreev, N.S. Sariciftci, G. Hlawacek, C. Teichert, A. Thierry, B. Lotz, Thin Solid Films 443 (2003) 108.

[29] F. Balzer, J. Beermann, S.I. Bozhevolnyi, A.C. Simonsen, H.-G. Rubahn, Nano Lett. 3 (2003) 1311.

[30] S. Müllegger, O. Stranik, E. Zojer, A. Winkler, Appl. Surf. Sci. 221 (2004) 184.

[31] H. Sitter, A. Andreev, C. Teichert, G. Hlawacek, T. Haber, D.-M. Smilgies, R. Resel, A. M. Ramil, N.S. Sariciftci, Phys. Status Solidi (b) 242 (9) (2005) 1877.

[32] H. Plank, R. Resel, A. Andreev, N.S. Sariciftci, H. Sitter, J. Cryst. Growth 237 (2002) 2076.

[33] A. Andreev, H. Sitter, C.J. Brabec, P. Hinterdorfer, G. Springholz, N.S. Sariciftci, R. Resel, H. Plank, Mater. Res. Soc. Symp. Proc. 665 (2001).

[34] A. Andreev, H. Sitter, R. Resel, D.-M. Smilgies, H. Hoppe, G. Matt, N.S. Sariciftci, D. Meissner, D. Lysacek, L. Valek, Mol. Cryst. Liq. Cryst. Sci. Technol. 385 (2002) 61.

[35] A. Andreev, F. Quochi, F. Cordella, A. Mura, G. Bongiovanni, H. Sitter, G. Hlawacek, C. Teichert, N.S. Sariciftci, J. Appl. Phys. 99 (2006) 034305.

[36] A. Andreev, H. Sitter, C.J. Brabec, P. Hinterdorfer, G. Springholz, N.S. Sariciftci, Synth. Met. 121 (2001) 1379.

[37] A. Andreev, R. Resel, D.-M. Smilgies, H. Hoppe, G. Matt, H. Sitter, N.S. Sariciftci, D. Meissner, H. Plank, O. Zrzavecka, Synth. Met. 138 (2003) 59.

[38] A. Andreev, H. Sitter, N.S. Sariciftci, C.J. Brabec, G. Springholz, P. Hinterdorfer, H. Plank, R. Resel, A. Thierry, B. Lotz, Thin Solid Films 403–404 (2002) 444.

[39] G. Hlawacek, Q. Shen, C. Teichert, R. Resel, D.-M. Smilgies, Surf. Sci. 601 (2006) 2584.

[40] T. Mikami, H. Yanagi, Appl. Phys. Lett. 73 (1998) 563.

[41] H. Yanagi, S. Okamoto, Appl. Phys. Lett. 71 (1997) 2565.

[42] H. Yanagi, T. Morikawa, Appl. Phys. Lett. 75 (1999) 187.

[43] Y. Yoshida, H. Takiguchi, T. Hanada, A. Tanigaki, E.M. Han, K. Yase, J. Cryst. Growth 198 (1999) 923.

[44] D.M. Smilgies, N. Boudet, H. Yanagi, Appl. Surf. Sci. 189 (2002) 24.

[45] E.J. Kinztel Jr., D.M. Smilgies, J.G. Sofronik, S.A. Safron, D.H. Van Winkle, J. Vac. Sci. Technol. A 22 (2004) 107.

[46] F. Balzer, H.G. Rubahn, Surf. Sci. 548 (2004) 170.

[47] T. Haber, A. Andreev, A. Thierry, H. Sitter, M. Oehzelt, R. Resel, J. Cryst. Growth 284 (2005) 209.

[48] T. Haber, M. Oehzelt, R. Resel, A. Andreev, A. Thierry, H. Sitter, D.M. Smilgies, B. Schaffer, W. Grogger, J. Nanosci. Nanotechnol. 6 (2006) 1.

[49] A. Andreev, A. Montaigne, G. Hlawacek, H. Sitter, C. Teichert, J. Vac. Sci. Technol. A 24 (2006) 1660.

[50] W. Chen, C. Huang, X.Y. Gao, L. Wang, C.G. Zhen, D. Qi, S. Chen, H.L. Zhang,K.P. Loh, Z.K. Chen, A.T.S. Wee, J. Phys. Chem B 110 (2006) 26075.

[51] G. Heimel, L. Romaner, J.-L. Brédas, E. Zojer, Surf. Sci. 600 (2006) 4548.

[52] W. Osikowicz, X. Crispin, C. Tengstedt, L. Lindell, T. Kugler, W.R. Salaneck, Appl. Phys. Lett. 85 (2004) 1616.

[53] L. Romaner, G. Heimel, J.-L.Brédas, A. Gerlach, F. Schreiber, R.L. Johnson, J. Zegenhagen, S. Duhm, N. Koch, E. Zojer, Phys. Rev. Lett. 99 (2007) 256801.

[54] S. Duhm, A. Gerlach, I. Salzmann, B. Bröker, R.L. Johnson, F. Schreiber, N. Koch, Org. Electron. 9 (2008) 111.

[55] J. Meyer, S. Hamwi, T. Bulow, H. Johannes, T. Riedl, W. Kowalsky, Appl. Phys. Lett. 91(2007) 113506.

[56] N. Koch, S. Duhm, J.P. Rabe, A. Vollmer, R.L. Johnson, Phys. Rev. Lett. 95 (2005) 237601.

[57] Z.Q. Gao, B.X. Mi, G.Z. Xu, Y.Q. Wan, M.L. Gong, K.W. Cheah, C.H. Chen, Chem. Commun. 1 (2008) 117.

[58] P.S. Szalay, J.R. Galan-Mascaros, R. Clerac, K.R. Dunbar, Synth. Met. 122 (2001) 535.

[59] P.S. Szalay, J. R.Galan-Mascaros, B.L. Schottel, J. Bacsa, L.M. Perez, A.S. Ichimura, A. Chouai, K.R. Dunbar, Journal of Cluster Science 15 (2004) 503.

[60] S. Müllegger, G. Hlawacek, T. Haber, P. Frank, C. Teichert, R. Resel, A. Winkler, Appl. Phys. A 87 (2007) 103.

[61] C. Teichert, G. Hlawacek, A. Andreev, H. Sitter, P. Frank, A. Winkler, N.S. Sariciftci, Appl. Phys. A 82 (2006) 665.

[62] P. Frank, G. Hlawacek, O. Lengyel, A. Satka, C. Teichert, R. Resel, A. Winkler, Surf. Sci. 601 (2007) 2152.

[63] P. Frank, A. Winkler, Appl. Phys. A 90 (2008) 717.

[64] P. Frank, G. Hernandez-Sosa, H. Sitter, A. Winkler, Thin solid films 516 (2008) 2939.

[65] G. Hlawacek, P. Puschnig, P. Frank, A. Winkler, C. Ambrosch-Draxl, C. Teichert, Science 321 (2008) 108.

[66] P. Frank, N. Koch, M. Koini, R. Rieger, K. Müllen, R. Resel, A. Winkler, Chem. Phys. Lett. 473 (2009) 321.

[67] Bröker et al., in preparation.

[68] P. Frank et al., in preparation.

[69] H. Ehrenreich, F. Spaepen, *Solid State Physics*, Vol. 49, Academic Press Inc., San Diego, California, 1995.

[70] P.W. Atkins, *Physical Chemistry*, Oxford University Press, Oxford, 1998.

[71] S. Müllegger, *Adsorption and Thin Film Growth of Oligo-phenylenes on gold surfaces*. PhD thesis, Institute for solid state physics, Graz University of Technology, Graz, Austria (2005).

[72] K. Seki, U.O. Karlsson, R. Engelhardt, E.-E. Koch, W. Schmidt, Chem. Phys. 91 (1984) 459.

[73] P. Puschnig, C. Ambrosch-Draxl, Phys. Rev. B 56 (1999) 7891.

[74] Standard reference database. NIST; http://webbook.nist.gov/cgi/cbook.cgi?ID=C4499836&Units=SI , 2008.

[75] K.N. Baker, A.V. Fratini, T. Resch, H.C. Knachel, W.W. Adams, E.P. Socci, B.L. Farmer, Polymer 34 (1993) 1571.

[76] Y. Delugeard, J. Desuche, J.L. Badour, Acta Cryst. B 32 (1976) 702.

[77] G. Hlawacek, *Molecular growth mechanisms in para-sexiphenyl thin film deposition*. PhD thesis, Institute of physics, University of Leoben, Leoben, Austria.

[78] T.L. Cairns, R.A. Carboni, D.D. Coffman, V.A. Engelhardt, R.E. Heckert, E.L. Little,

E.G. McGeer, B. C. McKusick, W. J. Middleton, J. Am. Chem. Soc. 79 (1957) 2341.

[79] D.S. Acker, W.R. Hertler, J. Am. Chem. Soc. 84 (1962) 3370.

[80] P. Frank, *Adsorption, Schichtwachstum und Desorption von p-Hexaphenyl auf Glimmer-Oberflächen*. Master's thesis, Institute for solid state physics, Graz University of Technology, Graz, Austria (2006).

[81] T. Haber, *Structural Order in Epitaxially Grown Para-Sexiphenyl Thin Films on KCl(100) and Mica Surfaces*. Master's thesis, Institute for solid state physics, Graz University of Technology, Graz, Austria (2004).

[82] Ch. Wöll, S. Chiang, R.J. Wilson, P.H. Lippel, Phys. Rev. B 39 (1989) 7988.

[83] I.V. Markov, *Crystal growth for beginners*. World Scientific, New Jersey, 2nd edition, (2003).

[84] M.A. Herman, H. Sitter. *Molecular Beam Epitaxy*. Vol. 7 of Springer Series in Materials Science, Springer Verlag, Berlin-Heidelberg, (1989).

[85] J. Venables, G. Spiller, M. Hanbücken, Rep. Prog. Phys. 47 (1984) 399.

[86] J. Krug, P. Politi, T. Michely, Phys. Rev. B: Condens. Matter Mater. Phys. 61 (2000) 14037.

[87] M. Kalff, P. Smilauner, G. Comsa, T. Michely, Surf. Sci. 426 (1999) L447.

[88] T. Michely, J. Krug, *Islands, Mounds and Atoms*. Vol. 42 of Springer Series in Surface Science, Springer Verlag, Berlin-Heidelberg, (2004).

[89] G. Ehrlich, F. Hudda, J. Chem. Phys. 44 (1966) 1039.

[90] R.L. Schwöbel, E.J. Shipsey, J. Appl. Phys. 37 (1966) 3682.

[91] J. Krug, J. Stat. Phys. 87 (1997) 505.

[92] P. Politi, J. Phys. I 17 (1997) 797.

[93] M.P. Seah, Surf. Sci. 32 (1972) 703.

[94] E. Umbach, M. Sokolowski, R. Fink, Appl. Phys. A, 63 (1996) 565.

[95] O. Stranik, *Adsorption und Schichtwachstum von p-Quarterphenyl auf Goldoberflächen*. Master's Thesis, Institute for solid state physics, Graz University of Technology, Graz, Austria (2002).

[96] Inficon Inc., *Operating Manual, XTM/2 Deposition Monitor*. Inficon Inc., New York (1995).

[97] P.A. Redhead, Vacuum 12 (1962) 203.

[98] K.J. Laidler, *Chemical Kinetics*. HarperCollins, New York (1987).

[99] K. Christmann, *Introduction to Surface Physical Chemistry*. Springer Verlag, Berlin-Heidelberg, (1991).

[100] S.L. Tait, Z. Dohnalek, C.T. Campbell, B.D. Kay, J. Chem. Phys. 122 (2005) 164708.

[101] K.R. Paserba, A.J. Gellman, Phys. Rev. Lett. 86 (2001) 4338.

[102] K.A. Fichthorn, R.A. Miron, Phys. Rev. Lett. 89 (2002) 196103.

[103] K.A. Fichthorn, K.E. Becker, R.A. Miron, Cat. Today 123 (2007) 71.

[104] E. Habenschaden, J. Küppers, Surf. Sci. Lett. 138 (1984) L147.

[105] D. Briggs, M.P. Seah, *Practical Surface Analysis by Auger and X-ray Photoelectron Spectroscopy*. John Wiley & Sons, Chichester/New York/Brisbane/Toronto/ Singapore (1983).

[106] K. Oura, V.G. Lifshits, A.A. Saranin, A.V. Zotov, M. Katayama, *Surface Science*. Springer Verlag, Berlin (2003).

[107] H. Bubert, H. Jenett, *Surface and Thin Film Analysis: Principles, Instrumentation, Applications*. Wiley-VCH, Weinheim (2002).

[108] http://www.wsu.edu/~scudiero/, 2009.

[109] G. Ertl, J. Küppers, *Low Energy Electrons and Surface Chemistry*. Vol. 4 of Monographs in Modern Chemistry, Verlag Chemie, Weinheim (1974).

[110] D.P. Woodruff, T.A. Delchar, *Modern Techniques of Surface Science*. Cambridge University Press, Cambridge (1986).

[111] G. Binning, C.F. Quate, C. Gerber, Phys. Rev. Lett. 56 (1986) 930.

[112] Nanosurf AG, *Nanosurf easyScan 2 AFM System*. Nanosurf AG, Switzerland (2005).

[113] Nanosurf AG, *Nanosurf easyScan 2 Software Reference*. Nanosurf AG, Switzerland (2005).

[114] http://www3.physik.uni-greifswald.de/method/afm/eafm.htm, 2009.

[115] I.D. Baikie, M. Porterfield, P. Smith, P.J. Estrup, Rev. Sci. Instrum. 70 (1999) 1842.

[116] I.D. Baikie, P.J. Estrup, Rev. Sci. Instrum. 69 (1998) 3902.

[117] I.D. Baikie, S. Mackenzie, P.J. Estrup, J.A. Meyer, Rev. Sci. Instrum. 62 (1991) 1326.

[118] I.D. Baikie, E. Venderbosch, J.A. Meyer, P.J. Estrup, Rev. Sci. Instrum. 62 (1991) 725.

[119] I.D. Baikie, K.O. van der Werf, J. Broeze, A. van Silfhout, Rev. Sci. Instrum. 60 (1989) 930.

[120] I.D. Baikie, U. Petermann, B. Lagel, J. Vac. Sci. Technol. A 19 (2001) 1460.

[121] I.D. Baikie, U. Petermann, A. Speakman, B. Lagel, K.M. Dirscherl, P.J. Estrup, J. Appl. Phys. 88 (2000) 4371.

[122] K. Müller, C.C. Chang, Surf. Sci. 14 (1969) 39.

[123] K. Müller, C.C. Chang, Surf. Sci. 8 (1968) 455.

[124] H. Poppa, A.G. Elliot, Surf. Sci. 24 (1971) 149.

[125] F. Balzer, L. Kankate, H. Niehus, R. Frese, C. Maibohm, H.G. Rubahn, Nanotechnology 17 (2006) 984.

[126] H. Glowatzki, B. Bröker, R.-P. Blum, O.T. Hofmann, A. Vollmer, R. Rieger, K. Müllen, E. Zojer, J.P. Rabe, N. Koch, Nano Lett. 8 (2008) 3825.

[127] N. Yoshimoto, T. Sato, Y. Saito, S. Ogawa, Mol. Cryst. Liq. Cryst. 425 (2004) 279.

[128] R. Resel, T. Haber, O. Lengyel, H. Sitter, F. Balzer, H.G. Rubahn, in preparation.

[129] I. Elkinani, J. Villain, Solid State Commun. 87 (1993) 105.

[130] G. Koller, S. Surnev, M. Ramsey, F. Netzer, Surf. Sci. 559 (2004) L187.

[131] G. Witte, S. Lukas, P.S. Bagus, C. Wöll, Appl. Phys. Lett. 87 (2005) 263502.

[132] T. Haber, A. Andreev, A. Thierry, H. Sitter, M. Oehzelt, R. Resel, J. Cryst. Growth 284 (2005) 209.

[133] O. Hofmann, private communications.

[134] KP Technology LTD, *UHV Kelvin Probe.* KP Technology LTD, UK (2006).